ROYAUME DU MAROC
Université Mohammed V - RABAT -
جامعة محمد الخامس - الرباط -
Faculté des sciences
كلية العلوم
CENTRE D'ETUDES DOCTORALES - SCIENCES ET TECHNOLOGIES

N° d'ordre : 3377

THESE

En vue de l'obtention du : ***DOCTORAT***

Structure de Recherche : ***Laboratoire de la Matière condensée et des Sciences interdisciplinaires (LaMCScI)***

Discipline : ***Physics***

Spécialité : ***Materials Science***

Présentée et soutenue le : 21/11/2020 par :

Naima ENNASSIRI

Investigation of magnetic properties in $CoFe_2O_4$ nanostructures and magnetocaloric effect in antiperovskite materials type Mn_3AC (A=Ga, Al): experimental and simulations

JURY

Abdelilah BENYOUSSEF	PES	Académie Hassan II des sciences et technique, Rabat	Président
Hamid EZ-ZAHRAOUY	PES	Faculté des sciences, Université Mohammed V, Rabat	Directeur de thèse
Mohammed BENAISSA	PES	Faculté des sciences, Université Mohammed V, Rabat	Rapporteur/Examinateur
Mohammed LOULIDI	PES	Faculté des sciences, Université Mohammed V, Rabat	Rapporteur/Examinateur
Abdelmajid AINANE	PES	Faculté des sciences, Université Moulay Ismail, Meknés	Rapporteur/Examinateur
Noureddine MASAIF	PES	Faculté des sciences, Université Ibn Tofail, Kénitra	Rapporteur/Examinateur
Naoufal BAHLAWANE	Directeur de recherche	Institut de Science et Technologie du Luxembourg, Luxembourg	Invité

Année Universitaire : 2020-2021

Acknowledgments

This work thesis has been carried out in the Laboratory of Condensed Matter and Interdisciplinary Sciences (LaMCScI) in Faculty of Sciences – University Mohammed V of Rabat, under the supervision of professor **Hamid EZ-ZAHRAOUY**.

So, to begin, I'm deeply grateful to my thesis reporter professor **Abdelilah BENYOUSSEF** from Hassan II Academy of Science and Technology in Rabat, who did me the honor to head the chair of jury for this thesis. I would like to express my deepest gratitude for him as he is one of the big scientists who made me love the physics during my university studies and for providing me with all the tools a good scientist requires both for his research and personal behavior.

I would like to acknowledge my thesis supervisor professor **Hamid EZ-ZAHRAOUY** from the faculty of sciences in Rabat, for his support and help during these years. I would like to thank him for entrusting me with the thesis subject and for leading me to achieve it. I express to him my gratitude for his availability, for the fruitful and interesting discussions we were able to have and also for providing me with the knowledge and material used during my research. We've been through hard times, but I was really lucky to have professor EZ-ZAHRAOUY as my leader, and for that I'll be forever in his debt. I thank him from my heart for guiding and encouraging me.

My sincere thanks go also to professor **Mohammed BENAISSA** from the Faculty of Sciences in Rabat, for his teaching during my master degree and for reporting and examining my thesis.

I would like to especially thank my Professor **Mohammed LOULIDI** from the Faculty of Sciences in Rabat who was also my supervisor during my bachelor thesis, for his scientific background he transferred to us, his patience and his kindness, also for reporting and reviewing my PhD thesis.

I would like also to express my appreciation to my thesis reporter and jury member the professor **Abdelmajid AINANE** from the faculty of sciences in Meknes, for accepting to evaluate my thesis and research works.

I would like to express my thanks to Professor **Nourredine MASAIF**, from the Faculty of Science in Kenitra, for reporting and reviewing my thesis.

I would also like to thank Doctor **Naoufal BAHLAWANE**, from Luxembourg Institute of Science and Technology for his collaborations and scientific spirit, also for accepting to report and review my thesis.

My sincere thanks to all the collaborators from the ERASMUS+ scholarship. Special thanks to the kindest Christine Boudin for helping me with all the requirements for a safe and comfortable stay in Germany. My deepest thanks go to Mohammed Es-Souni, Professor at the University of Applied Sciences, Institute for Materials and Surface Technology (IMST), Kiel in Germany, for his warm welcome and permanent advices and scientific exchanges during my year stay in Germany. I would also like to thank my dear friend Artjom Roth for his patience, advices, great help as well as a shoulder to lean on during the hours of need. Thank you also for Matthias Dietze and Claus-Henning Solterbeck for their availability and scientific help.

I would like also to offer my special thanks to all the professors, collaborators and thesards of our laboratory for their valuable suggestions and discussions. I would particularly like to thank the entire LaMCScI team, in particular: Ismail Benabdallah, Khadija Daoudi, Bazine Widad Hind El Massaoudi, Salma Saidi, Houda Hajji, Noura Baaala, EL Fdil Rachid…., Thanks to them for the good moments that we shared and the personal and professional help they provided. May they find here all my respects and encouragement for a good continuation.

Finally, A big thanks to my family and especially to my parents. I thank my beloved mom from the bottom of my heart, no words can express how I feel towards her, she taught me to be patient and to never give up. My father who gave me his strength and who always trusted my choices and supported me with his smile, nothing would have been possible without my dear mom and dad. A big thank to all my sisters who were always there for me.

It is thanks to everyone (family, professors and friends) who have given yourselves that I have been able to go this far.

To all, thank you

Abstract

This thesis focuses on the study of structural, electronic, magnetic and magnetocaloric properties of antiperovskite materials type Mn_3AC (A=Al, Ga) by using theoretical methods (DFT and Monte Carlo simulation).

For Mn_3GaC we investigate the second order transition. A significant MCE with no hysteresis loss is observed. On the other hand, Mn_3AlC antiperovskite also undergoes a second order transition with absence of hysteresis loss and low cost and environment friendly raw materials. For that reason, these criterions suggest that Mn_3GaC and Mn_3AlC may be a good candidate for magnetic refrigeration applications.

The second part of this thesis will be devoted to the synthesis of $CoFe_2O_4$ nanostructures including nanorods and nanoporous oxide layers. Both nanostructures were characterized by Scanning Electron Microscopy (SEM), X-ray spectroscopy (EDS) and X-ray Diffraction (XRD). The five steps of the synthesis of $CoFe_2O_4$ nanorods were reported as a function of the electrolyte's compositions. The $CoFe_2O_4$ nanoporous oxide layer was fabricated by electrochemical anodization from the parent alloy FeCoV sheet, leading to an ordered nanoporous structure of $CoFe_2O_4$. Our characterization methods confirmed the transformation of the as-anodized oxide layer into nanoporous oxide layers $CoFe_2O_4$. The magnetic properties of the obtained $CoFe_2O_4$ nanoporous oxide layer have been investigated as a function of the applied magnetic field directions and thickness.

Keywords: DFT, Monte Carlo simulation, Antiperovskites, $CoFe_2O_4$ nanorods, $CoFe_2O_4$ nanoporous oxide layers.

Résumé

Cette thèse porte sur l'étude des propriétés structurales, électroniques, magnétiques et magnétocaloriques des matériaux antiperovskite de type Mn_3AC (A = Al, Ga) en utilisant des méthodes théoriques.

Pour Mn_3GaC, nous avons étudié la transition du second ordre. Un MCE significatif sans perte d'hystérésis est observé. D'autre part, l'antiperovskite Mn_3AlC subit également une transition de second ordre avec l'absence de perte d'hystérésis et des matières premières à faible coût et respectueuses de l'environnement. Pour cette raison, ces critères suggèrent que ces matériaux peuvent être de bons candidats pour des applications de réfrigération magnétique.

La seconde partie de cette thèse sera consacrée à la synthèse de nanostructures $CoFe_2O_4$ comprenant des nanorods et des couches d'oxide nanoporeux. Les deux nanostructures ont été caractérisées par microscopie électronique à balayage (SEM), spectroscopie rayons X (EDS) et diffraction des rayons X (XRD). Les cinq étapes de la synthèse de nanorods $CoFe_2O_4$ ont été reportées en fonction des nombreuses compositions d'électrolytes testées. La couche d'oxyde nanoporeux $CoFe_2O_4$ a été fabriquée par anodisation électrochimique de la feuille d'alliage parent FeCoV. Nos méthodes de caractérisation ont confirmé la transformation de la couche d'oxyde anodisé en couches d'oxyde nanoporeux $CoFe_2O_4$. Les propriétés magnétiques de la couche d'oxyde nanoporeux $CoFe_2O_4$ obtenue ont été étudiées en fonction des directions et de l'épaisseur du champ magnétique appliqué.

Mots-clés : DFT, Simulation Monte Carlo, Anti-pérovskites, $CoFe_2O_4$ nanorods, Couche d'oxide $CoFe_2O_4$ nanoporeux.

Résumé détaillé

Durant ces dernières décennies, notre planète connait des enjeux environnementaux majeurs liés au réchauffement climatique. Pour faire face à ces problèmes, les enjeux écologiques et énergétiques sont actuellement et dans les années à venir des sujets de recherche majeurs. De plus, la rareté des sources d'énergie constitue une source supplémentaire de motivation pour une source alternative. D'où le besoin de chercher de nouvelles familles de matériaux tels que les matériaux antiperovskite et les nanostructures de $CoFe_2O_4$. Le présent travail de cette thèse sera divisé en quatre chapitres. Ainsi, nous proposons ci-dessous les résumés des chapitres constituant cette thèse.

Dans le premier chapitre, nous avons fait une étude bibliographique sur les concepts de base du magnétisme incluant une classification sur les types de magnétisme connus. En même temps, dans cette étude on a vérifié l'effet du magnétisme pour les nanomatériaux, vu le besoin dans notre thèse. Sans oublier, une recherche approfondie sur les matériaux utilisées dans notre travail (i.e. les matériaux antiperovskite et les spinelles ferrites $CoFe_2O_4$).

Dans le deuxième chapitre, nous avons présenté les outils et les méthodes utilisées dans la préparation de cette thèse. Nous avons tout d'abord donner les bases et l'historique de la théorie fonctionnelle de la densité et de la simulation Monte Carlo. Ces deux méthodes ont été utilisés pour effectuer l'étude des propriétes structurales, électroniques, magnétiques et magnétocaloriques des matériaux antiperovskite. Par la suite on a discuté les méthodes expérimentales de synthèse et de caractérisation utilisés lors de la synthèse des nanostructures de $CoFe_2O_4$.

Le troisième chapitre de cette thèse porte sur l'étude des propriétés structurales, électroniques, magnétiques et magnétocaloriques des matériaux antiperovskite de type Mn_3AC (A = Al, Ga) en utilisant des méthodes théoriques consistant en un mélange entre la théorie fonctionnelle de la densité et la simulation de Monte Carlo. Pour le composé Mn_3GaC, constitué de deux transitions magnétiques (une première d'un état antiferromagnétique en un état ferromagnétique et une seconde transition de l'état ferromagnétique en paramagnétique), on s'est focalisé sur l'étude la transition du second ordre. Un MCE significatif sans perte d'hystérésis est observé autour de Tc. Les valeurs maximales du changement d'entropie magnétique (ΔS_{mag}), du changement de température adiabatique (ΔTad) et de la puissance de refroidissement relative (RCP) sont respectivement de 5,65 J / Kg. K, 13,81 K, 351,90 J / kg, sous un champ magnétique externe appliqué de H = 4.5 T. D'autre part, l'antiperovskite

Mn_3AlC subit également une transition du second ordre avec une température de Curie autour de Tc = 287K, une grande largeur à mi-hauteur de sa courbe -ΔSm (T), une absence de perte d'hystérésis et des matières premières respectueuses des coûts et de l'environnement. Les valeurs maximales de ΔS_{mag}, ΔT_{ad} et RCP sont respectivement de 6,40 J / Kg. K, 13,60 K et 416,96 J / Kg. Pour cette raison, ce critère et le faible coût de ces matériaux peuvent suggérer que Mn_3GaC et Mn_3AlC peuvent être de bons candidats pour des applications de réfrigération magnétique autour de la température de Curie.

Pour le quatrième chapitre, il sera consacré à la synthèse de nanostructures $CoFe_2O_4$ comprenant des nanorods et des couches d'oxyde nanoporeux. Les deux nanostructures ont été caractérisées par microscopie électronique à balayage (MEB), spectroscopie aux rayons X (EDS) et diffraction des rayons X (XRD).

Les nanorods de ferrite de cobalt alignés verticalement $CoFe_2O_4$ (CFO) ont été synthétisés en suivant 5 processus, comme cela sera décrit en détail dans la thèse : Dans la première étape, des plaquettes de Si commerciales ont été utilisées comme substrats. Tandis qu'une couche d'or conductrice a été déposée par-dessus le substrat de silicium pour agir comme une électrode avec une conductivité élevée pour l'électrodéposition de $CoFe_2$ nanorods. En plus de cela, une pulvérisation (sputtering) d'une couche épaisse a été réalisée au-dessus de l'électrode en or à l'aide d'une inter-couche adhésive Ti. Pour la 2ème étape, une technique d'anodisation électrochimique a été utilisée pour oxyder la couche d'Al en un gabarit (template) d'oxyde d'aluminium anodisé (AAO), ce processus a conduit à l'auto-organisation des pores. Dans la 3ème étape, une technique d'électrodéposition potentiostatique a été utilisée pour remplir le template poreux AAO avec les nanorods métalliques de $CoFe_2$. Suite à cela, la 4ème étape consiste à supprimer le template AAO en utilisant une dissolution chimique. Ce dernier processus nous a conduit à obtenir une matrice de nanorods $CoFe_2$ autonome. Enfin, dans la cinquième étape un recuit chimique a été utilisé pour transformer les de nanorods $CoFe_2$ en nanorods $CoFe_2O_4$ isolants.

En un premier lieu, une méthode d'anodisation électrochimique a été utilisée pour synthétiser une couche d'oxyde nanoporeux $CoFe_2O_4$ auto-ordonné. Grâce à l'anodisation de la feuille d'alliage source FeCoV, sous des conditions d'électrolytes et d'anodisations bien déterminées, une structure nanoporeuse ordonnée $CoFe_2O_4$ a été obtenu, et qui pourrait bien avoir un potentiel important sur de nombreuses applications magnétiques. La méthode de microscopie à balayage électronique (SEM) a montré que la taille des nanopores restait constante dans une gamme de 15 nm indépendant du potentiel d'anodisation. La spectroscopie à rayons X à

dispersion d'énergie (EDS) et les mesures de diffraction des rayons X (XRD) confirment la transformation de la couche nanoporeuse anodisé en une couche d'oxyde nanoporeux en phase avec $CoFe_2O_4$. De plus, en utilisant la magnétométrie à échantillon vibrant (VSM), les propriétés magnétiques de la couche d'oxyde nanoporeux $CoFe_2O_4$ a été étudiée en fonction de la direction du champ magnétique externe et de l'épaisseur de la couche d'oxyde nanoporeux.

List of Publications.

Articles

Accepted:

1- **Ennassiri, N.**, Tahiri, N., El Bounagui, O., Ez-Zahraouy, H., & Benyoussef, A. (2018). Structural, electronic, magnetic, and magnetocaloric properties in metallic antiperovskite compound Mn_3GaC. Materials Research Bulletin, 98, 335-339.

2- **Ennassiri, N.**, Tahiri, N., El Bounagui, O., Ez-Zahraouy, H., & Benyoussef, A. (2018). Magnetic, magnetocaloric and transport properties in $AlCMn_3$ antiperovskite compound. Journal of Alloys and Compounds, 741, 1196-1202.

Submitted (Under review):

- **Ennassiri, N.,** Roth, A., Ez-Zahraouy, H., Es-Souni, M., "Formation of spinel CoFe2O4 nanoporous oxide layers by electrochemical anodization", Submitted to Solid State Communications

Communications and Internship

- Oral Communication at the "1st International Materials Science and Engineering for Green Energy Conference (IMSEGEC2017)" at Al Akhawayn University, Ifrane. May 2017.

- Oral Communication at "Journées Nationales des doctorants et des jeunes chercheurs"

- Oral Communication at 2nd Interlab-Meeting at Faculty of Sciences Rabat, December 2019.

- 5 months Internship at Morrocan Foundation for Advanced Science and Research (MASCIR). 2017.

- 1 Year Erasmus+ Scholarship at Kiel University of Applied Sciences "Fachochhschule Kiel", Institute for Materials Science and Surface Technology, Germany. 2018

- 4 Months Internship at Centre National pour la Recherche Scientifique et Technique (CNRST) division d'unité d'appui technique et recherche scientifique (UATRS) 2019.

Chapter I. Theoretical backgrounds

Chapter II: Computations theory and experimental methods

Chapter III. Structural, electronic, magnetic, and Magnetocaloric Properties in antiperovskite materials of type Mn_3AC (A=Ga, Al)

Chapter IV. Fabrication of $CoFe_2O_4$ nanostructures

List of tables

Table of Figures

General introduction

The need for refrigeration technologies continues to increase day by day. However, conventional refrigeration systems based on the compression and expansion of gases are at the origin of the emission of 30% of greenhouse gases, namely CFCs and HCFCs, directly responsible for the deterioration of the Ozone layer and global warming. To deal with these problems, ecological and energy issues are currently and in the coming years major research subjects. In addition, the scarcity of energy sources constitutes an additional source of motivation to direct research towards more economical cooling systems.

Research in this area is therefore exploring new avenues. One of the most promising is magnetic refrigeration, an emerging technology that uses compact systems (solid and non-volatile materials as active components), quiet, clean and high efficient energetically (up to 1.5 times that of the expansion compression). This technology, credible to produce an "ecological" and energy efficient cooling, based on the magnetocaloric effect (MCE) presented by certain magnetic materials. The principle of this effect was discovered in 1881 by the physicist E. Warburg and explained in 1917 by P. Weiss and A. Piccard. The temperature of the magnetic material increases when a sufficiently intense magnetic field is applied to it and decreases when this field is removed.

In recent years, a number of material families have been identified as potential candidates. Gadolinium is the only pure element to have a strong magnetocaloric effect in the vicinity of ambient temperature, its high price and low resistance to aqueous corrosion do not allow it to be considered for large-scale applications. As a result, current research has turned mainly towards several families of ferromagnetic materials: compounds based on gadolinium such as than $Gd_5(Si_xGe_{1-x})_4$, lanthanum-based compounds of the $LaFe_{13-x}Si_x$ type and compounds without rare earth element but based on manganese and Fe_2P type such as the ternary $MnFeP_{1-x}As_x$.

recently, the antiperovskite compounds Mn_3AX (A = Ga, Al, Sn, In, Zn, etc.; X = C, N) have attracted great attention because of their unique properties such as superconductivity, a giant magnetoresistance (GMR) and large magnetocaloric effect (MCE). Among them, promising materials have been achieved like the antiperovskite Mn_3GaC and Mn_3AlC which are exhibiting a significant MCE at T = 249 K and T = 287 K, respectively.

In the first part of our study, by using the theoretical methods including Density Functional Theory (DFT) and Monte Carlo Simulations, we focused on researching and calculating the

magnetic properties and magnetocaloric effect of Mn_3GaC and Mn_3AlC antiperovskite compounds.

In the second part of this thesis and as a part of our collaboration with ERASMUS+ scholarships, we conducted this part of our research at the "Institute for Materials and Surface Technology (IMST)"- University of Applied Sciences, Kiel-Germany. The framework of the project is to create a sensor based on an extrinsic multiferroic material composed of functional piezoelectric and magneto strictive materials.

In this context, we aim at fabricating two types of $CoFe_2O_4$ nanostructures: The first one consists at synthesizing Co_2FeO_4 nanorods, grown by using electrochemical deposition inside the pores of anodic aluminum oxide (AAO). The second type of nanostructure is a new form of $CoFe_2O_4$ consisting of self-ordered $CoFe_2O_4$ nanoporous oxide layer via electrochemical anodization of FeCoV alloy metal sheet. The benefits of the electrochemical method are the cheap and most straightforward approach to obtain ordered nanostructures under the right conditions. This method allowed us to get a new nano-structural form of $CoFe_2O_4$. The synthesized $CoFe_2O_4$ nanorods and $CoFe_2O_4$ nanoporous oxide layer may be used for several applications.

The first chapter is divided into three parts. The first part is focused on the study of the magnetic properties of the materials at the bulk and nanoscale level. We uncovered the origin of magnetism and the magnetic classification of materials. A significant effort was made to determine the magnetic equations describing the phenomena. In addition to that, we laid the thermodynamic foundations necessary for the study of the magnetocaloric effect. The second part is dedicated to the study of the large family of magnetocaloric materials based on Manganite antiperovskite compounds Mn_3AX. In the last part of this chapter, we will discuss the $CoFe_2O_4$ spinel ferrites materials, by focusing on their properties as well as applications.

The second chapter is devoted to generalities on the Density functional Theory method which will be intensively used to study the electronic structure and the magnetic properties of our materials. The theory of density functional and the different approximations used in this thesis will be thoroughly described. This chapter is also devoted to the Monte Carlo method. The different algorithms of Monte Carlo simulation have been defined and explained. Following that, we described the different techniques of characterization used (Scanning Electron microscope to analyze the microstructure and identify the chemical elements in the materials, X-Ray diffraction to confirm the crystal structure and the Vibrating Sample Magnetometer (VSM) for measuring the magnetic properties.

The third chapter is dedicated to presenting the results of our various research concerning the study of the structural, electronic, magnetic, magnetocaloric and transport related properties of Mn_3GaC and Mn_3AlC compound. To this end, several theoretical methods were used; namely Density Functional Theory (DFT), and Monte Carlo Simulation (MCS).

The fourth chapter deals with the formation of $CoFe_2O_4$ nanorods by electrochemical deposition. Followed by the process of fabricating $CoFe_2O_4$ nanoporous oxide layer by anodizing a commercial rolled sheet of a FeCoV alloy. We will show how the process parameters affect the porous structure, and the post processing treatment of the $CoFeO_4$ stoichiometry and properties. Finally, the magnetic properties of $CoFe_2O_4$ nanoporous oxide layer have been studied as a function of external applied magnetic field direction and thickness.

Chapter I. Theoretical background

1. Magnetism

1.1. Basic Concepts of Magnetic Materials

Electromagnetic force is generated due to electric current passing through matter. The force between two electric charges at rest is just electric. However, if the charges are in movement then a different force exists between them, as called magnetism.

Ampere postulated that magnetic properties of magnetic materials are due to atomic current loops. He proposed that magnetism in materials must be due to "molecular currents". This suggests that magnetism in atoms arise mainly due to magnetic moments of its rotating electrons. Electrons in atoms are continually revolving around the nucleus, and possess an electrostatic charge.

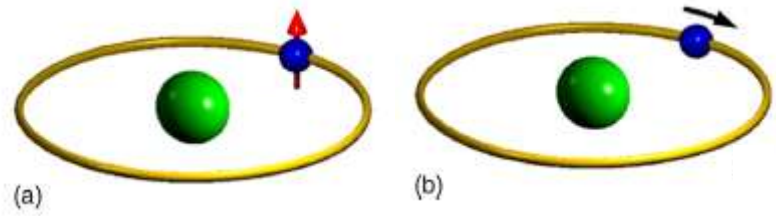

Figure 1. *(a) Magnetic moment produced by the spin of the electron and (b) that produced by an electron orbiting the nucleus.*

Therefore, the movement of electrons around the nucleus constitute small atomic current loops.[1-2] However, Ampere predicted impractically large currents, implying, there must be another origin of magnetism. In 1928 Dirac proposed the solution for fully relativistic quantum mechanical equations of electrons.[3] This explanation formed the basis for second magnetic mechanism. This second source of magnetism was spin, which is coming from electron rotating around its own axis as shown in Figure 1b. Additionally, the spin of an electron is hard to visualize, but it has the properties of a small magnetic moment pointing either "up" or "down" direction as could be seen from Figure 1a. Therefore, there are two main moments contributions, namely spin moment and orbital moment. The orbiting electrons rotation creates a magnetic moment quantized in units of the Bohr magneton $\mu_B = {he^-}/{2m_e} = 9.274 \times 10^{-24}\ \mathrm{J.T^{-1}}$.[4-5] Furthermore, each electron has a spin moment of 1

μ_B. Somewhat, it is incorrect but provides an illustrative picture of the electrons or spins rotating around its own axis.

A circulating electron in an atom has a magnetic moment. In a bulk material, these moments add up vectorially and they can give a net magnetic moment which is non-zero. Magnetization M of a sample could be defined to be equal to its net magnetic moment per unit volume:[6]

$$M = \frac{m_{net}}{V}, \qquad (1)$$

M is a vector with dimensions $L^{-1}I$ and is measured in a unit of $A.m^{-1}$. Let's consider a long solenoid of N turns per unit length and carrying a current I. The magnetic field in the interior of the solenoid is given by

$$B_0 = \mu_o NI, \quad (2)$$

If the interior of the solenoid is filled with a material with non-zero magnetization, the field inside the solenoid will be greater than B_0. The net magnetic field inside of the solenoid is expressed as: $B = B_0 + B_m$

with B_m being the field contributed by the material core. It turns out that this additional field B_m is proportional to the magnetization M of the material and is expressed as

$$B_m = \mu_o M, \quad (3)$$

where μ_0 is the permittivity of vacuum.

It is convenient to introduce another vector field H, called the magnetic intensity, which is defined by

$$H = \frac{B}{\mu_0} - M, \quad (4)$$

where H has the same dimensions as M and is measured in units of $A.m^{-1}$. Thus, the total magnetic field B is written as

$$B = \mu_0(H + M), \qquad (5)$$

The contribution to the total magnetic field inside the sample could be divided into two parts: the first one, due to external factors such as the current in the solenoid, represented by H. The second is due to the specific nature of the magnetic material, namely M. The latter quantity can be influenced by external factors. This influence is mathematically expressed as

$$M = \chi . H, \qquad (6)$$

Where χ, a dimensionless quantity, is called the magnetic susceptibility. It is a measure of how a magnetic material responds to an external field. Table 1 lists the susceptibility for some known elements. It is small and positive for materials, called paramagnetic[7] and small and negative for

materials, which are termed diamagnetic. In the latter case M and H are opposite in direction. From Eqs. 5 and 6 we obtain:

$$B = \mu_0(1+\chi)H, \qquad (7)$$
$$= \mu_0\mu_r H$$
$$= \mu H$$

where $\mu_r=1+\chi$, is a dimensionless quantity called the relative magnetic permeability of the substance. It is the analog of the dielectric constant in electrostatics. The magnetic permeability of the substance is μ and it has the same dimensions and units as

$$\mu = \mu_0\mu_r = \mu_0(1+\chi), \qquad (8)$$

The three quantities χ, μ_r and μ are correlated and only one of them is independent. Given one, the other two may be easily determined.

Diamagnetic substance	χ	**Paramagnetic substance**	χ
Bismuth	-1.66×10^{-5}	Aluminum	2.3×10^{-5}
Copper	-9.8×10^{-6}	Calcium	1.9×10^{-5}
Diamond	-2.2×10^{-5}	Chromium	2.7×10^{-4}
Gold	-3.6×10^{-5}	Lithium	2.1×10^{-5}
Lead	-1.7×10^{-5}	Magnesium	1.2×10^{-5}
Mercury	-2.9×10^{-5}	Niobium	2.6×10^{-5}
Nitrogen	-5.0×10^{-9}	Oxygen	2.1×10^{-6}
Silver	-2.6×10^{-5}	Platinum	2.9×10^{-4}
Silicon	-4.2×10^{-6}	Tungsten	6.8×10^{-5}

***Table 1**. Magnetic susceptibility of some elements at 300K*

1.2. Classification of magnetic materials

1.2.1 Diamagnetism

For diamagnetism; electrons in an atom orbiting around nucleus possess orbital angular momentum. These orbiting electrons are equivalent to a current-carrying loop and thus possess orbital magnetic moment. Diamagnetic materials have a resultant magnetic moment in an atom being zero. When a magnetic field is applied, those electrons having orbital magnetic moment

in the same direction slow down and those in the opposite direction speed up. This happens due to induced current in accordance with Lenz's law. Thus, the material develops a net magnetic moment in the direction opposite to that of the applied field and hence repulsion.

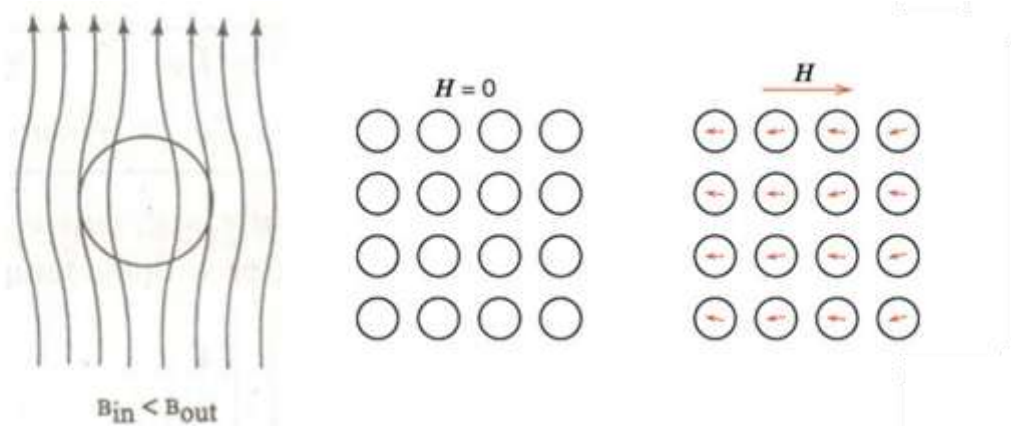

Figure 2. *Behavior of diamagnetic material in presence of magnetic field/ Atomic dipole configuration with and without magnetic field*

The magnetic susceptibility is negative and is also independent of the temperature as shown in Fig 3. That is, the magnitude of the magnetic field within a diamagnetic solid is less than that in a vacuum. The volume susceptibility for diamagnetic solid materials is on the order of -10^{-5} when placed between the poles of a strong electromagnet. Diamagnetic materials have applications in microsystems[8-9-10] and magnetic levitation.[11-12]

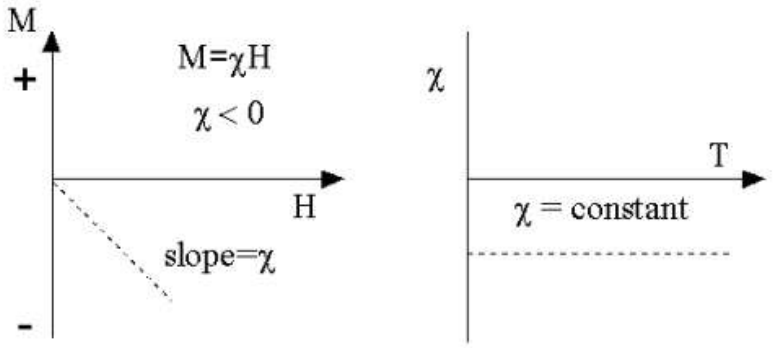

Figure 3*. Curves showing M vs H and χ Vs T for diamagnetic materials*

1.2.2 Paramagnetic Materials

A paramagnetic material contains permanent dipoles which are present due to the incomplete cancellation of electron spin and orbital magnetic moments, resulting in a magnetic moment even in the absence of an applied field. In the absence of external magnetic field, the dipoles are randomly oriented resulting in zero magnetic moment. When external magnetic field is applied, some of the permanent dipoles try to align in the direction of the magnetic field (Fig.

4). Since few dipoles try to align in the direction of the magnetic field, the net magnetic moment produced in the material is small and so the material is weakly magnetized. The susceptibilities of paramagnetic values range from 10^{-5} to 10^{2}.

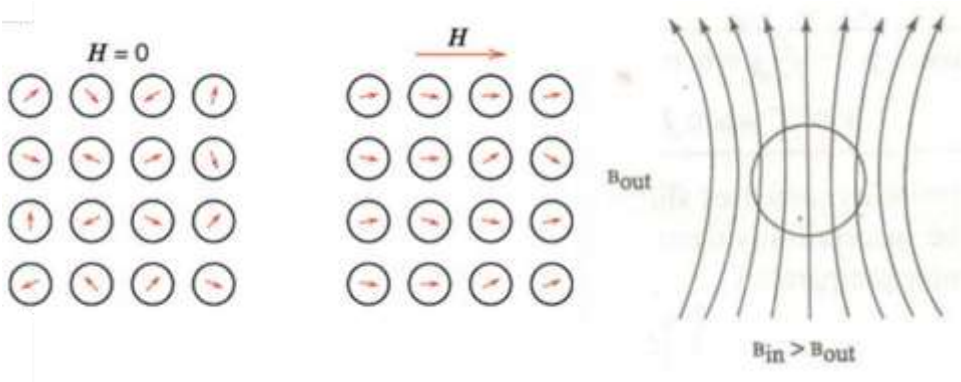

Figure 4. *Atomic dipole configuration with and without magnetic field for a paramagnetic material / Behavior of paramagnetic material in external magnetic field.*

Experimentally, one finds that the magnetization of a paramagnetic material is inversely proportional to the absolute temperature T,

$$M = C\frac{B_0}{T}, \qquad (9)$$

$$\chi = C\frac{\mu_0}{T}, \qquad (10)$$

This is known as Curie's law, after its discoverer Pierre Curie (1859-1906). The constant C is called Curie's constant. Thus, for a paramagnetic material both χ and μ_r depend not only on the material, but also on the sample temperature. As the field is increased or the temperature is lowered, the magnetization increases until it reaches the saturation value Ms, at which point all the dipoles are perfectly aligned with the field. Beyond this, Curie's law (Eq.10) is no longer valid.

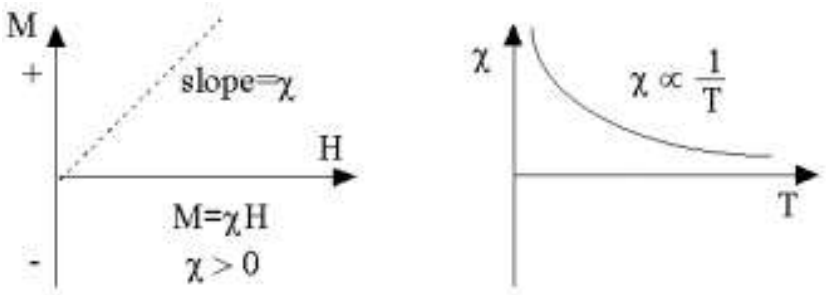

Figure 5. *Curves showing M vs H and χ Vs T for paramagnetic materials*

1.2.3. Ferromagnetic Materials

Some materials possess a permanent magnetic moment even in the absence of external magnetic field resulting in a permanent magnetization. Permanent magnetic moment in ferromagnetic materials is due to uncancelled spins of the electron. In a ferromagnetic material the dipoles of the adjacent atoms interact with each other which results in parallel alignment of all the dipoles (Fig. 6b). This interaction between the adjacent atoms is called exchange interaction or exchange coupling. By applying small value of magnetic field to the ferromagnetic material a large value of magnetization is produced.[13] Due to the parallel alignment of the atomic dipoles the material possesses a characteristic feature called spontaneous magnetization which results in the material allowing a greater number of lines to pass through it by appliance of an external magnetic field as shown in fig.6a.

The ferromagnetic property is also dependent of temperature. At high temperature, a ferromagnet becomes a paramagnet, as the domain structure disintegrates with temperature. This disappearance of magnetization with temperature is gradual. It is a phase transition reminding us of the melting of a solid crystal. The temperature of transition from ferromagnetic to paramagnetism is called the Curie temperature Tc.[14] The susceptibility above the Curie temperature as shown on fig.7, i.e., in the paramagnetic phase is described by:

$$\chi = \frac{C}{T - T_C} \quad (T > T_C) \qquad (11)$$

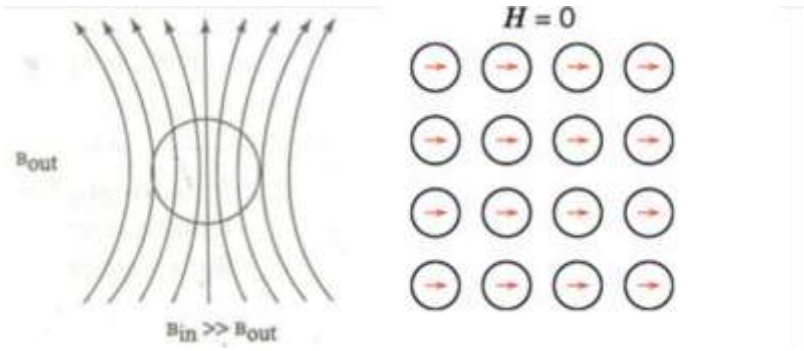

Figure 6. *(a) Behavior of ferromagnetic material in external magnetic field (b) Shows the alignment of atomic dipoles in ferromagnetic materials*

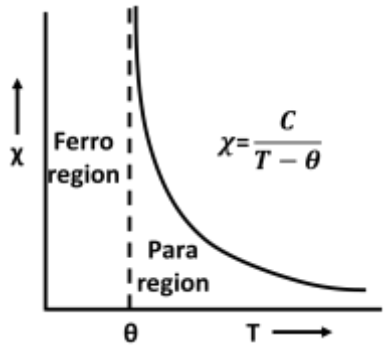

***Figure 7**. Variation of magnetic susceptibility with temperature for ferromagnetic material.*

1.2.4. Anti-ferromagnetic Materials

Anti-ferromagnetic material is a special class of ferromagnetic material. The material contains permanent dipoles. Similar to ferromagnetism, antiferromagnetism is associated with domain structure and exchange coupling between adjacent spins but the alignment of spins within a domain is anti-parallel. The spins are of equal magnitude. Indeed, the net magnetization in a domain is zero and over all domains is very small. In antiferromagnetic materials the distance between the interacting atoms is small such that the exchange forces result in antiparallel alignment of the dipoles. The susceptibility of antiferromagnetic material is temperature dependent. The characteristic feature of antiferromagnetic material is the occurrence of a sharp maximum peak in the susceptibility versus temperature curve (Fig. 8). As temperature increases the spin alignment is disturbed and magnetization decreases. However, beyond a temperature called Neel temperature (T_N), susceptibility drops. The value of magnetic susceptibility is positive and is very small when T is greater than the Neel temperature, T_N.[15]

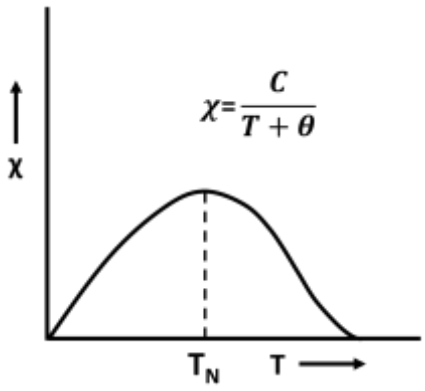

***Figure 8.** Variation of susceptibility with temperature for antiferromagnetic materials*

1.2.5. Ferrimagnetic Materials or Ferrites

Ferrimagnetic materials exhibit permanent magnetization, in addition to a spontaneous magnetization, saturation magnetization and hysteresis curve. Magnetic susceptibility of ferrimagnetic materials is very large and positive. The magnetic susceptibility for ferrimagnets is also temperature dependent. Fig. 9 shows the variation of susceptibility with temperature for ferrimagnetic materials. Saturation magnetization of ferrimagnetic materials is not as high as ferromagnetic materials. Since they are ceramic in nature, they are suitable for high frequency applications and in special magnetic devices.[16-17]

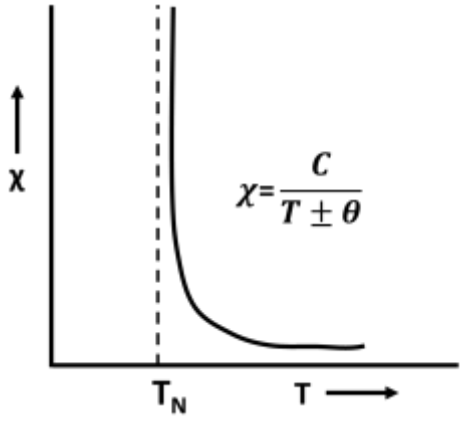

Figure 9. *Variation of susceptibility with temperature for ferrimagnetic materials*

1.3. Domain theory of ferromagnetic materials

In 1907, Weiss proposed domain theory to explain ferromagnetic behavior of a ferromagnetic material.[18] He stated that a single crystal of ferromagnetic solid compresses a large number of small regions, each region is spontaneously magnetized to saturation extent called a domain as shown in Fig. 10 below.

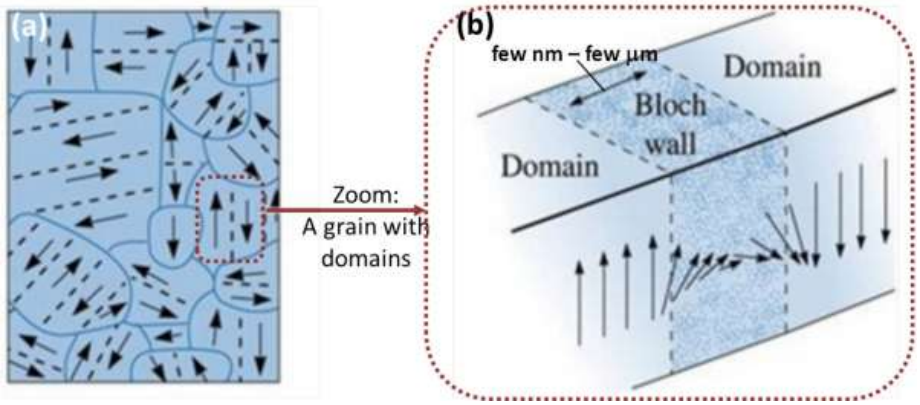

Figure 10. *(a) A qualitative sketch of magnetic domains in a polycrystalline material. (b) The magnetic moment in adjoining atoms changes its direction continuously across the boundary between domains.*[19]

The separation between the adjacent domains is called “a domain wall”. Each domain is spontaneously magnetized and all the domains are randomly oriented such that the net magnetic moment of the crystal is zero. When such a material is placed in a magnetic field the material gets magnetized by two processes.

1. Domain wall movement: The domains which are favorably oriented in the direction of the magnetizing field increase in volume at the cost of those that are unfavorably oriented.

2. Rotation of the domains: Application of higher magnetic fields rotates partially the domains in the direction of the magnetizing field. This results in further increase in the magnetizing field.

1.3.1. Hysteresis

Hysteresis means lagging or retardation of effect behind the cause. In our case, it is referring to the lag of magnetization behind the magnetizing field. When the temperature is less than the ferromagnetic Curie temperature hysteresis is exhibited. A part of the hysteresis curve is shown in Fig.11.

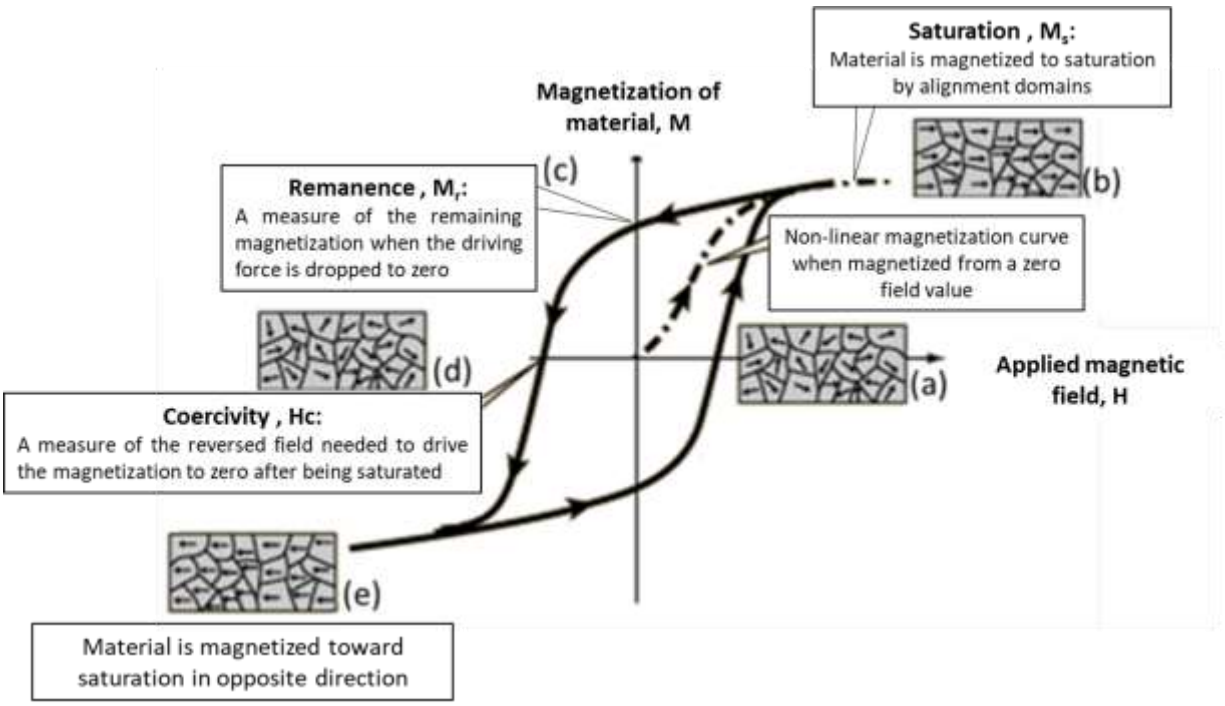

Figure 11. *M(H) hysteresis loop of ferromagnetic material*

The main parameters to describe ferromagnetic material can be extracted from a hysteresis loop. For a thorough understanding of magnetic properties of a material, Weiss domains behavior under applied magnetic field should be discussed. Initially, a ferromagnetic material consists of magnetic domains with random orientation. Applied magnetic field leads to reorientation of

magnetic moments towards its direction. Displacement of Bloch walls causes the growth of domains with magnetic moments parallel to applied field while reduction of other domains is observed. When all the moments are aligned with magnetic field the saturation state M_s is reached (Figure 11). Removal of the field leads to a decrease of magnetization: some magnetic moments are reoriented; some keep the magnetization parallel to the previously applied. Afterwards, the magnetization remaining after magnetic field drops to zero, the latter is called remanent magnetization or remanence M_r. If on previously saturated material an opposite magnetic field is applied, at a certain moment the global magnetization will drop to zero due to the alignment of domains with preferential directions. The field inducing zero global magnetization of saturated magnetic material is called coercivity field or coercivity H_c. Followed by an increase of the opposite magnetic field leading to magnetization toward saturation in opposite direction (Figure 11).

1.4. Magnetic interactions:

Magnetism of a given material is governed by the spin concept which is the coupling of magnetic moments in the material. This concept was developed by quantum theory in a short time from 1925 to 1928 by Pauli and Dirac.[20] They stated that, magnetism is created by different exchange interaction mechanisms such as ferromagnetic, ferrimagnetic, antiferromagnetic and spin glasses systems. The different types of exchange interactions can be classified as direct exchange interaction, indirect exchange interaction, super and double exchange interactions. A brief detail of these interactions is given in the following section.

1.4.1. Direct exchange interaction:

In a direct exchange interaction, the atoms are close enough, leading to an overlap of the wave function of electrons. As a result, a strong and short-range coupling of the magnetic spins occur which decreases quickly with the separation of the ions. An easy way to understand the direct exchange interaction, is to have two atoms and one electron from each atom. The Coulomb interaction can be minimal if the atoms become very close to each other and then the electrons stay in between the nuclei for most of their time. As the electrons should be located at the same area in space at the same time, Pauli's exclusion principle says that the electron’s spins should be opposite. As reported by Bethe and Slater most of the electrons time are spent in between nearby atoms when the distance between the atoms is small. As a consequence, for that the spins are antiparallel alignment and then we have negative exchange which is antiferromagnetism (see Fig. 12).

Figure 12. Antiparallel alignment for small interatomic separations

When the electrons are far from the atoms, they spend most of their time far apart from each other to decrease the repulsion between the electrons. The result of that is: parallel alignment or positive exchange which is ferromagnetism (see figure 13).

Figure 13. Parallel alignment for small interatomic separations

1.4.2. Double Exchange Interaction

Exchange interaction is a process in which two neighboring atoms (Manganese for example) and their connecting oxygen atom play a role. The process is depicted in Fig. 14. One of the manganese atoms has one of its e_g states occupied, while the other has an empty e_g shell. One electron tunnel from the oxygen atom to the manganese atom without e_g electrons. The e_g electron from the other manganese atom then tunnels to the freed 2p position on the oxygen atom. The obtained result in one electron moving from one manganese atom to the next. This process is how the double exchange interaction induces electrical conductivity. Since electrons retain their spin while tunneling, tunneling is only possible between states with parallel spins. Which is why double exchange interaction only occurring between manganese atoms whose t2g electrons have their spins aligned. Because double exchange interaction increases the freedom of electrons, it lowers their energy. This makes it energetically favorable for electrons of neighboring manganese atoms to align their spins, inducing by the occasion ferromagnetism. Since double exchange interaction requires filled Eg states as well as empty ones (holes) it is highly doping dependent.

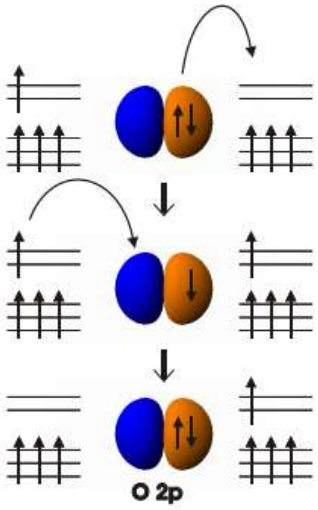

Figure 14. *Double exchange interaction*

1.4.3. Super exchange interaction

Super exchange interaction describes interaction between moments on ions too far apart from each other to be connected by direct exchange, but coupled through a non-magnetic material. Super exchange was proposed by Hendrik Kramers[21] in 1934 when he noticed in crystals like MnO, that there are Mn atoms that manage to interact with one another despite having nonmagnetic oxygen atoms between them. Phillip Anderson later refined Kramers' model in 1950.[22] To understand the super exchange interaction, we first consider a case where two magnetic ions are connected via a nonmagnetic ion by an angle of 180°. This is the arrangement which yields the strongest super exchange interaction. An example of material which shows such kind of exchange interaction is MnO once again. Two Mn dx^2-y^2 orbital are connected via O p_x orbital. The schematic in Fig. 15 (a) and (b) clearly explain how the 180° super exchange interaction become antiferromagnetic. Schematic in Fig 15 (a) shows that when the arrangement is antiferromagnetic both the hopping processes from the ligand are allowed while for ferromagnetic arrangement, the second hopping process is not allowed (Fig. 15 (b)) due to the Pauli exclusion principle. This makes antiferromagnetic state energetically favorable. The situation is quite different when two cations with d orbitals (dx^2-y^2 and $d3z^2$-1) form an angle of 90° with the connecting anion (p_x or p_z). Fig. 15 (c) clearly demonstrate that in this case ferromagnetic ordering will have lower energy, taking the advantage of the Hund coupling in the anion site.

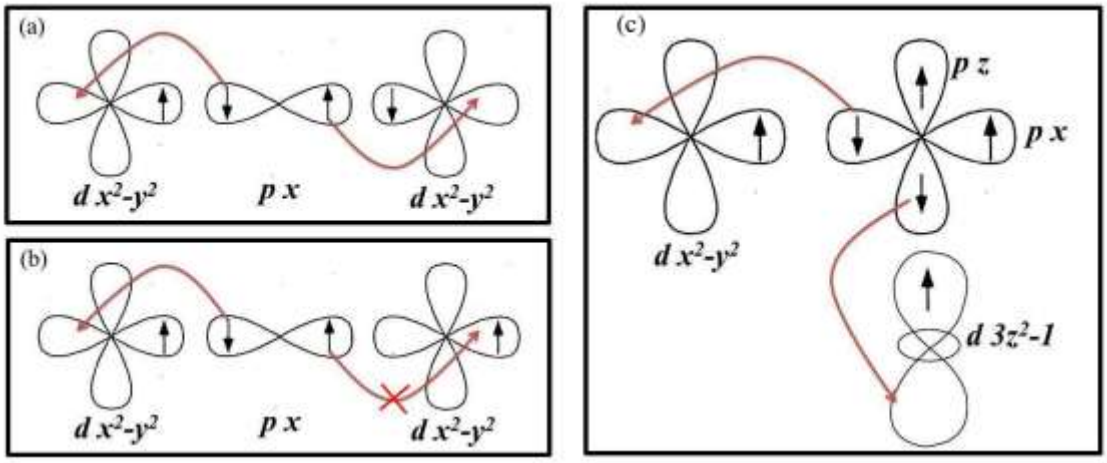

Figure 15. *Diagram of 180° super exchange interaction between cations separated by an anion (a) antiferromagnetic and (b) why it cannot be ferromagnetic. (c) diagram of the 90° super exchange interaction between two cations separated by an anion is ferromagnetic*

1.5. Magnetic anisotropy

In most magnetic materials, the magnetization tries to align itself along one of the main crystal directions which is called easy direction of magnetization. All ferromagnetic and ferrimagnetic materials possess, a crystal direction or a set of preferential magnetization directions.[23]

This magnetic anisotropy can have various causes. The most important in magnetic materials are the shape and magneto crystalline anisotropies. Shape anisotropy is associated with the geometrical shape of a magnetized body, and is related to the preference that the polarization in a long body is for the direction of the major axis. While, the magneto-crystalline anisotropy is associated with the crystal symmetry of the material.

Three situations that give rise to this anisotropy as an intrinsic crystal property exist. The first and most important one is when the atoms possess an electron-orbital moment in addition to an electron-spin moment. In such a situation the spin direction may be coupled to the crystal axis. This arises through the coupling between spin and orbital moments and the interaction between the charge distribution over the orbit and the electrostatic field of the surrounding atoms. There will then be one or more axes or surfaces along which magnetization requires relatively little work. The crystal will then be preferentially magnetized along such an easy axis or plane. The second situation is encountered in non-cubic crystal lattices. In these crystals the magneto-static interaction between the atomic moments is also anisotropic, which may give rise to easy directions or planes of magnetization. The third possibility of crystal anisotropy is found in the directional ordering of atoms as described by Néel.[24] This typically involves solid solutions of atoms of two kinds, A and B, linked by the atomic bonds *A*-*A*, *A*-*B* and *B*-*B*. In the presence of a strong external magnetic field the internal energy of these bonds may be to some extent direction-dependent. Given a sufficient degree of atomic diffusion-as a result of raising the temperature, for example-a certain ordering can be brought about in the distribution of the bonds; in this way it is possible to "bake" the direction of this field into the material as the easy axis of magnetization. In addition to these sources of magneto-crystalline anisotropy mechanical stresses may contribute through the magneto-elastic (magneto-strictive) properties of the crystal. This contribution, however, is considered to be negligible in hard magnetic materials.[21]

1.6. Crystal field Theory

1.6.1. Principle

This model was proposed by Bethe in 1929, it is purely based on the electrostatic interaction (Coulomb's law) between a central metal denoted (M) and the ligands (L), that is to say an ionic interaction (central atom = positive charge; ligand with free doublet = negative charge).

This model assumes that ligands are represented by negative point charges or by dipoles oriented with the free pair (partial negative charge) towards the central atom. These negative charges interact with the electrons of the d orbitals and the repulsion between entities of identical charge leads to repulsion and destabilization of orbitals.

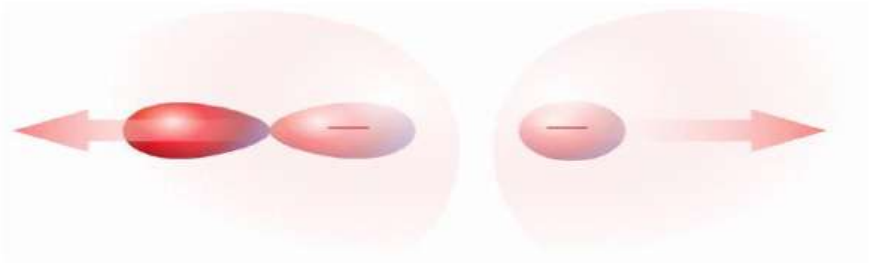

The consequence on the destabilization of the central ion is the lifting of degeneration and the splitting of the 5 atomic orbitals into two series of atomic orbitals.

1.6.2. Shape of atomic orbitals d and removal of degeneracy

As with p orbitals, the shape of d orbitals is far from being of spherical symmetry. It is determined by the geometry of the electronic procession.

There are five *d* orbitals, namely d_{xy}, d_{xz}, d_{yz}, d_{x2-y2}, and d_{z2}. These are directional orbitals made up of four lobes except for the d_{z2} orbital:

- The d_{xy}, d_{xz}, d_{yz} orbitals have the same symmetry (lobes centered on the bisectors of the axes,
- The d_{x2-y2}, and d_{z2} orbitals have their lobes centered on the Ox, Oy and Oz axes; as shown below.

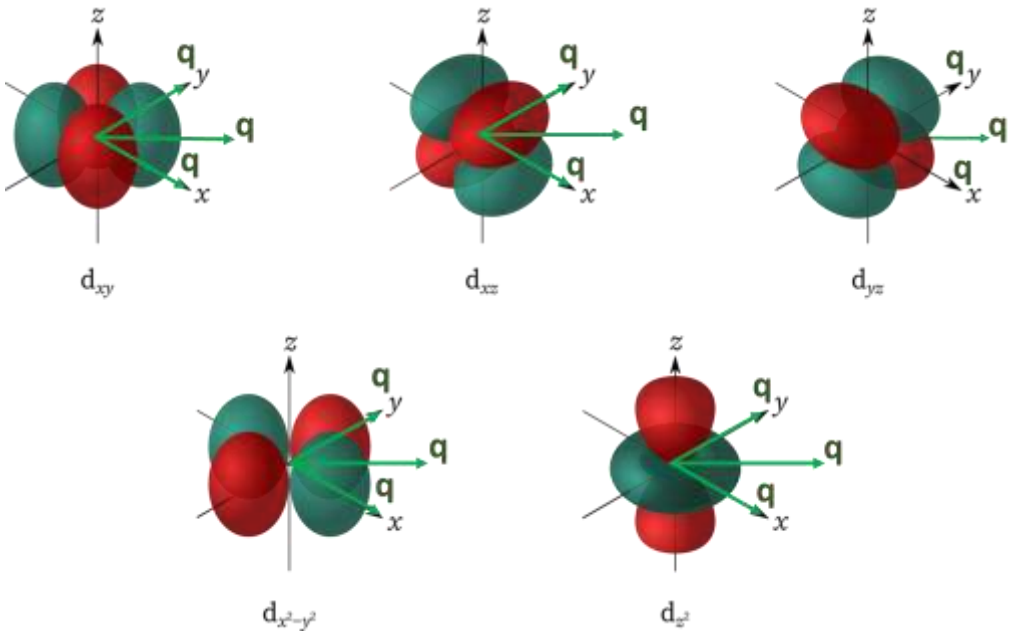

The extent of the destabilization of the five d orbitals and the lifting of degeneracy depends on the shape and symmetry of the complex. It is evaluated by the energy difference between the two groups of orbitals (d_{x2-y2} and d_{z2}) and (d_{xy}, d_{xz}, d_{yz},), and it is called crystal field energy.

Two different symmetries could be considered: octahedral symmetry and tetrahedral symmetry.

1.6.3. Influence of the symmetry of the environment

1.6.3.1 Octahedral symmetry case of the environment of coordinates

When *d* orbitals are in a field of octahedral symmetry. We observe a partial lifting of degeneracy, three d orbitals will be stabilized and the other two will be destabilized. The stabilization or destabilization of atomic d orbitals depends on their shapes and orientation (which depend on the magnetic quantum number m_l). Orbitals d_{x2-y2} and d_{z2} have their lobes oriented towards the ligands (negative charges). While the orbitals present a high electronic density (negative charges), their energy level will rise (repulsion). The situation is reversed in the case of the three orbitals d_{xy}, d_{xz}, d_{yz}, because their lobes are oriented towards diagonal directions (between ligands).

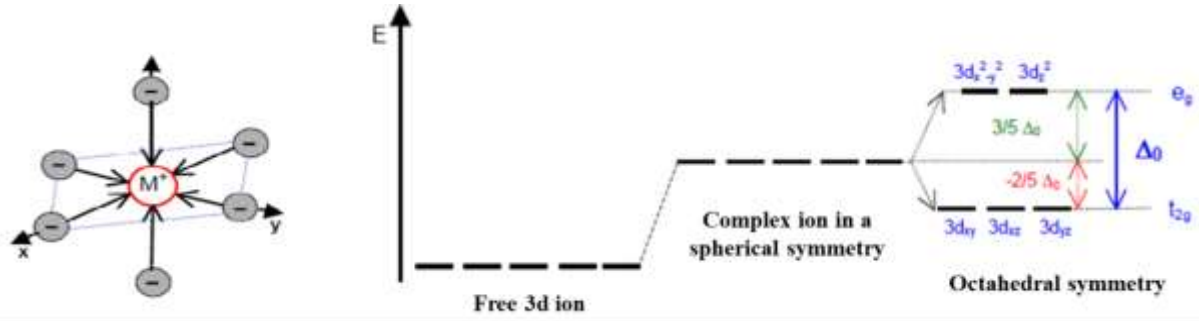

In this case: t_{2g} orbitals lower their energy, so they will become more stable and this stabilization corresponds to $-2\Delta_0/5$ per electron. On the other hand, the energy of the orbitals e_g will rise and the destabilization will correspond to $+3\Delta_0/5$ per electron.

1.6.3.2. Tetrahedral symmetry case of the ligand environment

A tetrahedron can always be inscribed in a cube. In the case of tetrahedral complexes (tetrahedral field), the ligands are placed in the positions between the x, y, z axes (in reality they occupy 4 vertices of the cube, see figure below).

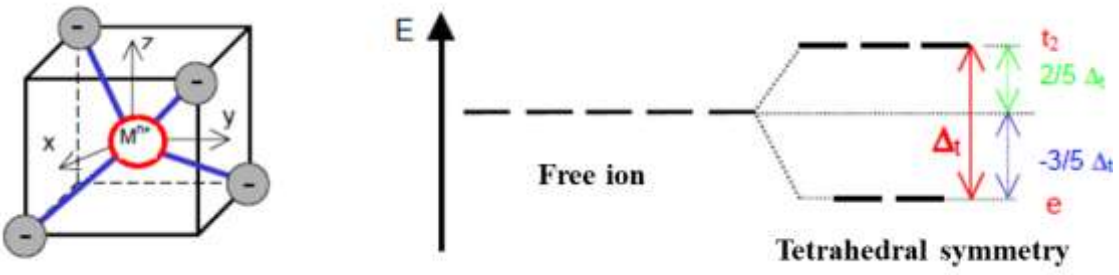

The removal of degeneracy corresponds to the difference Δ_t (splitting energy of orbitals d for tetrahedral symmetry), which separates the e and t_2 orbitals. In this case the d_{x2-y2} and d_{z2} are stabilized (degeneracy 2, symbol e) and the stabilization will correspond to $-3\Delta t/5$ by electron. On the other hand, the d_{xy}, d_{xz}, d_{yz} orbitals are destabilized (degeneracy 3, symbol t2), the destabilization will correspond to $+2\Delta t/5$ per electron.

In the case of the tetrahedral field, the splitting energy is smaller than in the case of the octahedral field. For the same ligand and the same distances M-L, the ratio of the two values is $\Delta t = 4/9\Delta_0$.

2. Magnetic nanoparticles

2.1. Magnetic properties of nanoparticles

Magnetic properties of nanoparticles (denotes as NP) can differ drastically from their bulk counterparts. A bulk magnetic material consists of a large number of formed magnetic domains attempting to minimize the magnetostatics energy of the material, which is why the structure of a magnetic material plays an important role in determining its magnetic properties. If the material size is reduced to a nanoscale level, a single NP can represent a single magnetic domain. Below a critical particle size the formation of domain walls would not occur (as the energy required to form them is more than the energy saved should they be formed) and hence

stable single domain particles can form.[25] The critical diameter (R_{sd}) for a magnetic nanoparticle (MNP) to reach the single domain limit is given by:

$$R_{sd} = \frac{36\sqrt{AK}}{\mu_0 M_s^2} \quad (12)$$

where A is the exchange constant, K is the effective anisotropy constant and Ms is the saturation magnetization.[26] For the majority of magnetic nanomaterials R_{sd} will be in the range of 10-100 nm, though for materials with a high magnetic anisotropy, this value can be higher.

In small magnetic NPs reaching the single domain limit (given by the equation (12)), the paramagnetic-like behavior can be observed even below the Curie temperature *T*c. The phenomenon is therefore called the superparamagnetism (SPM) as the whole particle behave like one "giant" superspin consisting of the atomic magnetic moments, thus the magnetic moment of the whole NP is 10^4-10^5 times larger than the atomic magnetic moment. The theory of SPM and relaxation of the NPs were treated by L. Neel and C. P. Bean.[27]

The SPM theory contains several assumptions. First, all moments within the NP rotate coherently, in other words the magnetic moment of the whole NP behaves as a one giant superspin with magnitude equal to summation of the individual atomic moments. Second, the magnetic energy required to magnetization reversal is given by the uniaxial magneto crystalline anisotropy (MCA) that can be expressed in the form:

$$E = K_{eff} V sin^2\theta_M \quad (13)$$

Where θ_M is the angle between the magnetic easy axis and the direction of the magnetic moment, K_{eff} effective anisotropy constant and *V* is the volume of the NPs. Third, the interparticle interactions are neglected.

In the case of the zero external magnetic field, $\mu_0 H$ the NP superspin will be stuck by the MCA in one of the two equilibrium state as is depicted in Figure 17. The relaxation time, τ of the NP into the equilibrium state is given by:

$$\tau = \tau_0 \exp\left(\frac{K_{eff} V}{k_B T}\right) \quad (14)$$

where k_B is the Boltzmann constant and *T* the temperature, the relaxation time τ_0 is of the order of 10^{-9}-10^{-12} s. Because of the small size, the energy barrier $K_{eff}V$ can be surpassed by the thermal fluctuations at a certain temperature, so-called blocking temperature, T_B.[28-29] Below the T_B, the NPs are in a blocked state analogous to the quasi-ordered state (such as ferromagnetism and ferrimagnetism). Upon reaching the T_B, the NP come in the SPM state. However, the T_B depends not only on the particle size, *d* and the K_{eff}, but also on the time window of the measurements, τ_m. If $\tau_m > \tau$ the NPs have enough time to fluctuate and the SPM state can be

observed, on the other hand if $\tau_m < \tau$ the blocked state of NPs will be observed. Indeed, determination of T_B is dependent on the used experimental technique (10^{-8} s for Mössbauer Spectroscopy, 1s for dc magnetic measurement, 10 - 10^{-3} s for ac magnetic measurement).

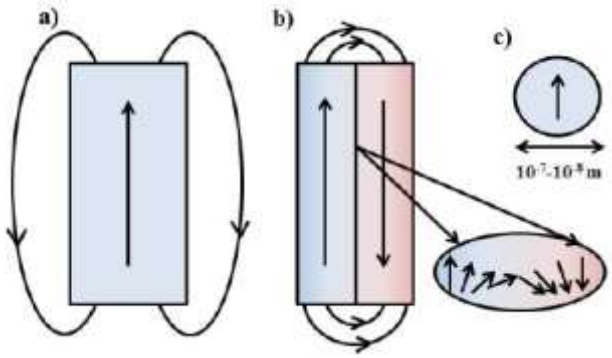

Figure 16. *Schematic illustration of the domain structure in bulk and submicron ferromagnetic material. a) The sample is uniformly magnetized with the high demagnetizing field associated with presence of the free poles at the surface. b) The sample is divided into two domains with opposite direction of magnetization, the demagnetizing field is twice lower; the inset shows the reorientation of the magnetic moments within the domain wall. c) The monodomain magnetic NP.*

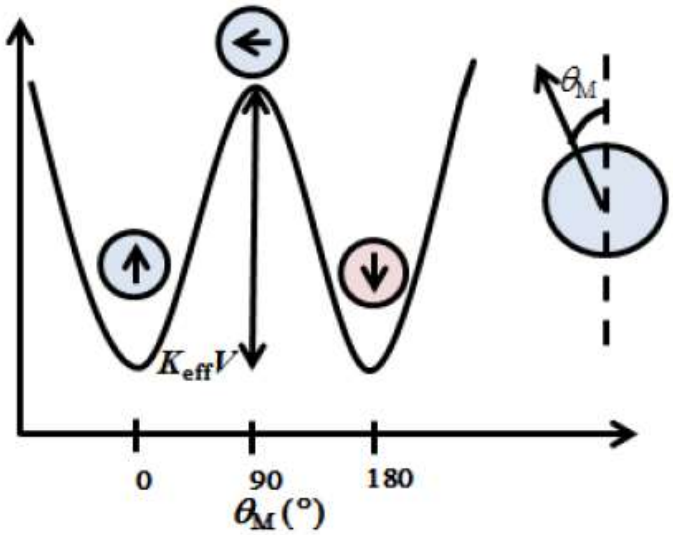

Figure 17. *The angular dependence of the energy barrier, $K_{eff}V$ in zero external field with definition of the axis system on the right, the dashed line corresponds to the magnetic easy axis of the NP*

2.2. Surface effects in nanoparticles

By decreasing the NP size, the numbers of atoms located at the surface of a NP (surface atoms) increases with respect to the all atoms and at some defined size, surface atoms dominate the volume atoms. The ratio of the surface atoms to the atoms located in the whole NP is given by the relation:

$$ratio = \frac{4\pi(\frac{d}{2})^2 \frac{1}{S_{unit}} N_S}{4\pi(\frac{d}{2})^3 \frac{1}{V_{unit}} N_V} \qquad (15)$$

where d is the particle diameter, S_{unit} and V_{unit} are the surface and volume of the unit cell, respectively and Ns, Nv are the number of atoms located at surface and in the whole volume of a NP. The dependence of the *ratio* on the d is depicted in Figure 18 for the spinel structure (details of the spinel structure will be discussed in the next section below). Only the atoms located at the surface were considered (as shown in the left panel). In the right panel the thickness of the surface layer was given by the thickness of the unit cell of the spinel structure (around 0.83 nm).

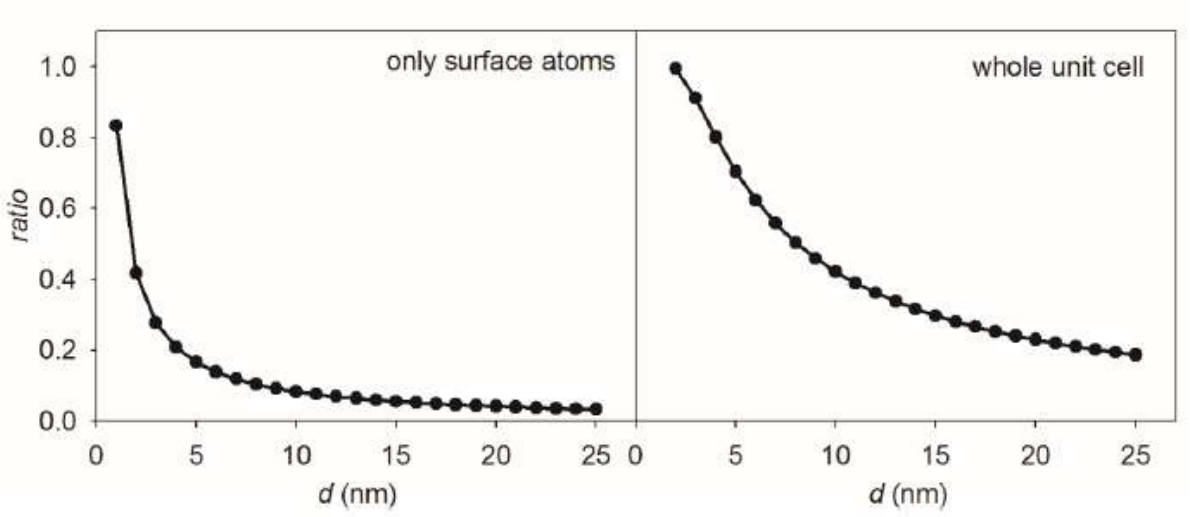

Figure 18. *The ratio of the surface atoms vs. all atoms in the whole volume. Left panel: Only the surface atoms lying exactly on the surface were considered. Right panel: The thickness of the surface layer was equaled to the one-unit cell of the spinel structure.*

It is well seen, that for NPs with smaller d (the exact value depends on the thickness of the surface layer) the surface spins become dominant, thus affecting the magnetic response of the whole NP.

Surface atoms exhibits lower coordination numbers originating from breaking of the symmetry of the lattice at the surface. Moreover, the exchange bonds are broken resulting in the spin disorder and frustration at the surface leading to the undesirable effects such as low saturation magnetization of the NP and/or the unsaturation of the magnetization in the high magnetic applied field.[30-31] The determination of the thickness of the shell is disputable, as not only the surface spins have to be considered, but a gradient of the orientation of individual spins should be expected.

During the last century, the lower *M*s of the NPs was to the bulk values.[32] Several works tried to explain this feature including the presence of nonmagnetic layer[28] or presence of hydrogen in the lattice. In 1971, J. M. D. Coey[26-27] suggested that the non-collinearity of the spin arrangement in NPs is responsible for the lower *M*s and proposed the so-called magnetic core-shell model of the NP. In the model, the NP consists of a core with the bulk spin arrangement and the disordered shell, where the spins are inclined at random angles to the surface, which was called spin canting angle. The latter spin canting angle depends on the number of the magnetic nearest neighbors connecting with the reduced symmetry and dangling bonds.

3. Magnetic refrigeration

3.1. History of magnetic refrigeration

Nowadays, a growing interest in using the magnetocaloric effect (MCE) has emerged as the cornerstone physical property behind an alternative technology for refrigeration both at room and at cryogenic temperatures. Indeed, due to its environmentally friendly technology since it eliminates ozone depleting gases, reducing the need for global warming greenhouse effect gases, and other hazardous gaseous refrigerants. Furthermore, magnetic refrigeration (MR) offers up to 60% of Carnot efficiency, much larger than any conventional refrigeration technologies. Medicine (hyperthermia) is an additional field in which MCE is being researched. The MCE was first observed in 1881, when Warburg first discovered a thermal effect on metal iron when applying it a varying magnetic field.[33] However, it was only later that its origin, cooling via adiabatic demagnetization, was independently explained by Debye in 1926[34] and Giauque in 1927.[35] Half a decade later, Giauque and MacDougall achieved the lowest temperature up to that time, 250mK, and using paramagnetic salts.[36] The entropy thermal dependence of a magnetic system as a function of the applied field can be illustrated by a schematic diagram of Temperature-Entropy (see Fig. 19 and Fig. 20).

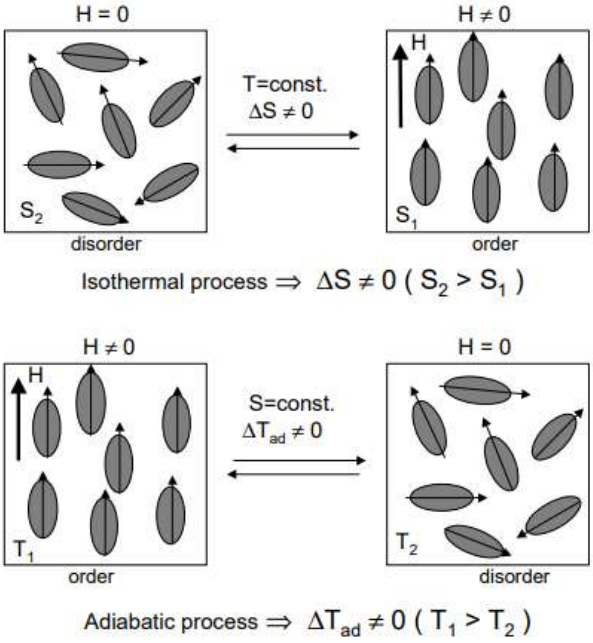

Figure 19. *Picture that shows the two basic processes of the magnetocaloric effect when a magnetic field is applied or removed in a magnetic system: the isothermal process, which leads to an entropy change, and the adiabatic process, which yields a variation in temperature*

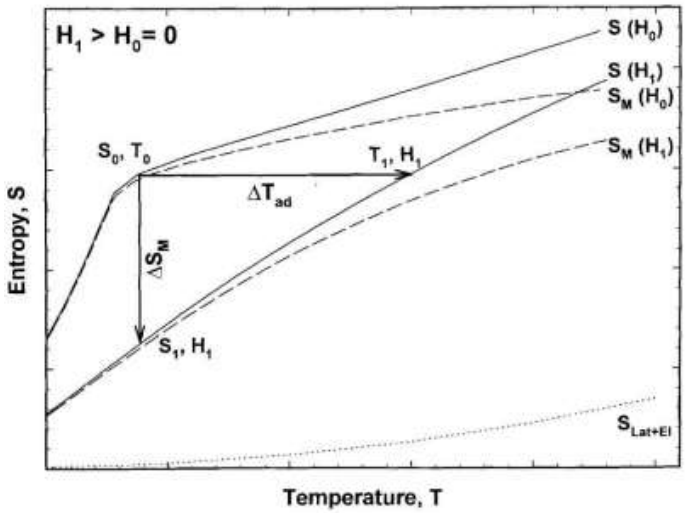

Figure 20. *S–T diagram showing the MCE. Solid lines represent the total entropy in two different magnetic fields ($H_0 = 0$ and $H_1 > 0$), dotted line shows the electronic and lattice contributions to the entropy (non-magnetic), and dashed lines show the magnetic entropy in the two fields. The horizontal arrow shows ΔTad and the vertical arrow shows ΔSm, when the magnetic field is changed from H_0 to H_1.*

3.2. Basics of the Magnetocaloric Effect

The entropy of a magnetocaloric material is the sum of three independent constituents, namely the magnetic entropy S_m, the entropy of the lattice S_l and the entropy of the conduction electrons S_e:

$$S = S_m (B, T) + S_l (T) + S_e (T) \qquad (16)$$

All constituent's magnitude is temperature dependent, while the magnitude of S_m has an additional strong dependence on the external magnetic field density B. S_l and S_e can be neglected at low temperatures, as S_m is much larger than S_l and S_e combined in that temperature regime. On a microscopic level, the magnetocaloric effect is caused by the interaction of the external magnetic field with magnetic moments in the material. In most cases, the magnetic moments originate from the presence of unfilled electron shells in transition metal or rare earth ions in the refrigerant, which imparts a total electronic angular momentum J on each ion. The magnetic moments thus have 2J+1 possible orientation, and by assuming that the thermal energy k_bT is greater than the splitting between the energy levels of these states - all will be equally occupied and will contribute to the magnetic entropy.

$$S_m = R.\ln (2J + 1) \qquad (17)$$

With R being the gas constant (8.314 J mol^{-1} K^{-1}).

By applying a magnetic field, the magnetic moments will tend to align with the field, increasing the energy difference between the states, reducing the occupation of higher energy states (those align counter to the field), thus reducing magnetic entropy.

When a sufficiently high external magnetic field is applied adiabatically to a material, the spin moments align, and the magnetic part of the entropy decreases due to the coupling of the magnetic field and the magnetic moments. To keep the total entropy (spin and lattice contributions) in an adiabatic process constant, the crystalline lattice part of the entropy increases and the material heats up. This heat is then transferred to the ambient atmosphere and the material returns to its initial temperature. Subsequently, when the magnetic field is removed adiabatically, the crystalline lattice entropy decreases and the material cools down. This adiabatic cycle of magnetic cooling is depicted in Fig. 20. The cycle is reversible, assuming the thermal hysteresis loss is negligible.

3.3. Thermodynamic aspects.

To understand the magnetocaloric effect behavior, it is necessary to recall the thermodynamic properties of a magnetic material plunged in a magnetic field H at a temperature T and under a pressure P.[37-38-39] The critical thermodynamic behavior of a magnetic system can be investigated in the framework of Gibbs free energy G. This latter can be expressed as follows:

$$G = U - TS + PV - MB \ (with\ B = \mu_0 H) \quad (18)$$

U is the internal energy, S is the full entropy, V is the volume, and M is the magnetization. Its total differential is given by

$$dG = dU - TdS - BdM + PdV - SdT - MdB + VdP \quad (19)$$

Since the free energy G is a state function, its total differential has the following form:

$$dG = (\frac{\partial G}{\partial T})_{P,B}dT + (\frac{\partial G}{\partial B})_{P,T}dB + (\frac{\partial G}{\partial P})_{B,T}dP \quad (20)$$

The generalized thermodynamic forces V, S, and M can be then identified by the following equations:

$$V = \left(\frac{\partial G}{\partial P}\right)_{B,T} \quad , \quad S = -\left(\frac{\partial G}{\partial T}\right)_{P,B} \quad , \quad M = -\left(\frac{\partial G}{\partial B}\right)_{P,T} \qquad (21)$$

Where T, B, and P are taken as the external variables. Based on Equation (20), we obtain the following relation:

$$\left(\frac{\partial M}{\partial T}\right)_{P,B} = -\frac{\partial}{\partial T}\left(\left(\frac{\partial G}{\partial B}\right)_{P,T}\right)_{P,B}$$

$$= -\frac{\partial}{\partial B}\left(\left(\frac{\partial G}{\partial T}\right)_{P,B}\right)_{P,T} = \left(\frac{\partial S}{\partial B}\right)_{P,T} \quad (22)$$

Then, the thermodynamic Maxwell relation that links the entropy change to the bulk magnetization, the magnetic field, and the temperature is obtained. Under a magnetic field changing from 0 to H ($B=\mu_0 H$), the isothermal entropy change can be written as the integral form of the Maxwell relation

$$\Delta S(T, 0 \rightarrow B) = \int_0^B \left(\frac{\partial M}{\partial T}\right)_{P,B'} dB' \quad (23)$$

This equation shows that the isothermal entropy change is not only proportional to the magnitude of the magnetic field but also depends strongly on the nature of the magnetic phase transition. In the case of materials exhibiting a first order character of the magnetic phase transition, i.e., a rapid variation of the order parameter as a function of the temperature (discontinuous change), the derivative of magnetization with respect to the temperature becomes larger, leading to large values of ΔS. Usually, the obtained ΔS is peaked in a narrow working temperature range. In contrast, for second order transition materials, ΔS reveals less marked feature values but in a wide magnetocaloric working temperature range. However, the isothermal entropy change can be also determined from specific heat measurement by using the second law of thermodynamics

$$\left(\frac{\partial S}{\partial T}\right)_{B,P} = \frac{C_P(T,B)}{T} \qquad (24)$$

Where C_P is the total specific heat. The integration yields

$$S(T,B) = S_0 + \int_0^T \frac{C_p(T',B)}{T'} dT' \qquad (25)$$

At absolute zero, the full entropy S_0 is usually considered to be 0. In this case, the isothermal entropy changes corresponding to the field variation from 0 to B can be expressed as follows:

$$\Delta S(T, 0 \rightarrow B) = \int_0^T \frac{C_P(T',B) - C_P(T',0)}{T'} dT' \qquad (26)$$

In addition to that, the infinitesimal entropy change *dS* for an isobaric process is given by

$$dS = \left(\frac{\partial S}{\partial T}\right)_B dT + \left(\frac{\partial S}{\partial B}\right)_T dB \qquad (27)$$

By using the thermodynamic Maxwell relation [Eq. 21] and the second law of thermodynamics [Eq. 23], Eq. 26 becomes:

$$dS = \frac{C_B}{T} dT + \left(\frac{\partial M}{\partial T}\right)_B dB. \qquad (28)$$

In a reversible adiabatic process, the integration of the above equation yields the second parameter that measures the magnetocaloric effect, namely, the adiabatic temperature change ΔT_{ad}.

$$\Delta T_{ad}(T, 0 \rightarrow B) = -\int_0^B \frac{T}{C_p(T,B)} \left(\frac{\partial M}{\partial T}\right)_{B'} dB'. \qquad (29)$$

According to this equation, the adiabatic temperature change is inversely proportional to the specific heat. Hence, the lower the specific heat is the higher ΔT_{ad} may be. However, the sign and the nature of the magnetocaloric effect, i.e., negative (inverse) or conventional, are governed by the sign of the derivative of magnetization with respect to temperature (dM/dT). For ferromagnets and paramagnets, the magnetization decreases with increasing temperature ($dM/dT<0$), which results in a conventional MCE ($\Delta T_{ad} >0$). For magnetocaloric materials presenting AF-F or AF-Para phase transitions, the magnetization increases with temperature ($dM/dT >0$), and hence, the MCE is negative ($\Delta T_{ad} <0$).

According to the second law of thermodynamics and Maxwell relation, the equation below can be obtained

$$\frac{\partial}{\partial B}\left(\frac{C_P}{T}\right) = \frac{\partial}{\partial B}\left(\frac{\partial S}{\partial T}\right) = \frac{\partial}{\partial T}\left(\frac{\partial S}{\partial B}\right) = \frac{\partial}{\partial T}\left(\frac{\partial M}{\partial T}\right). \qquad (30)$$

In the case of materials showing a second order magnetic transition, dM/dT shows usually a non-peaked maximum (or minimum) in the magnetic phase transformation zone. This means that the term (T/C_P) is magnetic field independent. Consequently, the adiabatic temperature change can be approached by:

$$\Delta T_{ad} = -\frac{T}{C_P} \Delta S. \qquad (31)$$

From Equation (30), larger MCE (ΔT_{ad}) can be expected for materials with high entropy change and low total specific heat.

3.4. Materials Research

Several promising classes of materials are known to exhibit a considerable MCE and have tunable transition temperatures. Currently, researches on this area aims to discover magnetic materials that display a large MCE at or near room temperature and that are economically viable and operate in fields generated by permanent magnets. Subsequently, continual efforts are being made to search for magnetocaloric materials with a first order phase transition in a narrow temperature range, since it is expected to maximize the MCE.[40-41-42] However, there are large thermal and magnetic hysteresis associated with first order behavior. Such hysteresis has a detrimental effect on the refrigerant capacity q, which is expressed as:

$$q = \int_{T_{cold}}^{T_{hot}} \Delta S(T,H) dT \qquad (32)$$

The refrigerant capacity q is a measure of how heat can be transferred between a hot and cold sink in an ideal refrigeration cycle. Therefore, it is unclear whether materials exhibiting a first, or second order phase transition should be used for magnetocaloric applications. Hence, the properties defining the ideal magnetic refrigerant, may vary with the refrigeration system and the desired temperature interval. In terms of an explicit criteria for selecting magnetic refrigerants, there are some prerequisites such as a high saturation magnetization (i.e. magnetic ions with large spin moments), which is proportional to the MCE. In addition to that, a small specific heat and a large thermal conductivity are also desirable, since the temperature change and heat exchange rate are optimized.[36] The main classes of materials for MCE applications are briefly discussed in this section. The rare-earth metal, Gd has a large magnetic moment and exhibits a considerable MCE near room temperature; it has therefore been the focus of research for magnetocaloric applications in recent years.

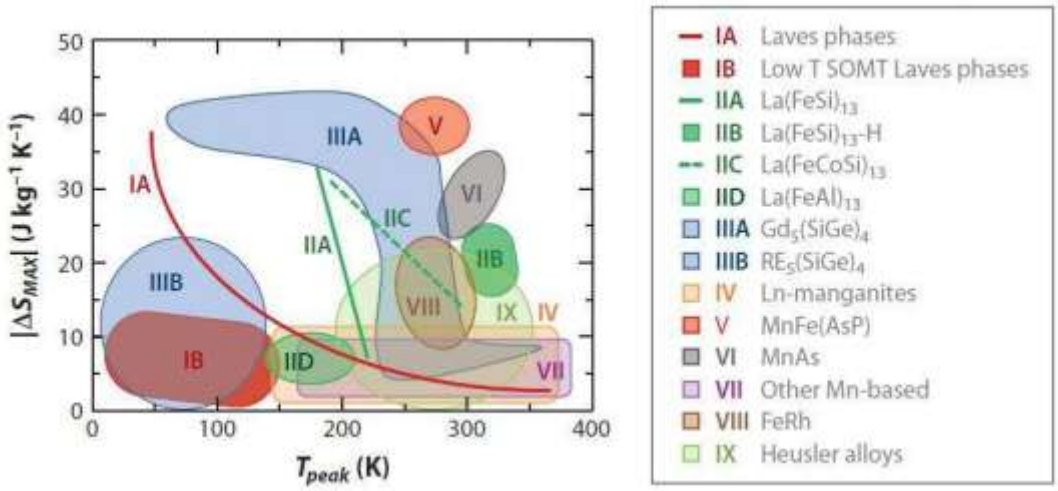

Figure 21. *The maximum entropy changes for ΔH=5T versus the peak temperature for different classes of magnetocaloric material.*[42]

Gd has been used in prototype room temperature regenerator designs,[43-44] and has been considered to be the most active magnetic refrigerant thus far. The ΔS_M, determined from magnetization measurements, is -9.8J. $K^{-1}Kg^{-1}$ for a magnetic field varying from 0T to 5T. Also ΔT_{ad} value is 11.6K near a cutie temperature of Tc = 294K.[45] Since rare-earth metals are acutely expensive, the usage of Gd as a solid refrigerant is commercially limited. Hence, transition metal-based alloys have an advantage since they are much cheaper than rare-earth metals. Materials undergoing a magneto structural phase transition with large values of ΔS_M are often referred to as giant magnetocaloric materials. Pecharsky and Gschneidner coined the term, Giant Magnetocaloric Effect from the alloy, $Gd_5Si_2Ge_2$ as its MCE was around 50% larger than that determined for Gd.[46] Despite the fact that the transition temperature (of 276K) is much lower than that of Gd, $Gd_5Si_2Ge_2$ is considered to be a potential candidate to improve the efficiency of large scale magnetocaloric refrigeration since the following MCE parameters have been determined: ΔS_M = -18$Jkg^{-1}K^{-1}$ and ΔT_{ad} = 15K for a ΔH = 5T.[42] Further studies on the substitution of Gd with other rare-earth metals have provided evidence for a consequent reduction in the MCE.[42] The giant MCE has also been observed in itinerant-electron compounds such as $LaFe_{13-x}Si_x$, and in general, a significant amount of research has been conducted on the magnetocaloric properties of the $La[Fe(Si,Al)]_{13}$ family.[47] The possibility of tuning the transition temperature with composition in such systems has been explored by Gutfleisch et al., through the variation of *x* and/or by hydrogenation.[48-49] In addition to that, $LaFe_{13-x}Si_x$ is a strong candidate for cooling devices, since it undergoes a first order field-induced itinerant-electron metamagnetic phase transition (FM-PM)[50-51]. Jia et al. have determined that a decrease in *x* results in a decrease of the T_C. While, an increase in *x* causes a decrease in the volume

contraction, which results from the phase transition.[52] Although the magnetic entropy change in $LaFe_{13-x}Si_x$ is dominant, the lattice entropy change is comparably large and counteracts most of the magnetic one. Hence, a more detailed, theoretical understanding of magneto-elastic/structural transitions is required to understand the MCE of such materials. In 2004, Gama et al.[53] reported on the existence of a pressure-induced colossal MCE in MnAs. The reported values for MnAs exceeded those of many active refrigerant materials. MnAs undergoes a first order magneto-structural transition from a FM-hexagonal structure to a PM-orthorhombic structure, at a transition temperature T_t (not exactly a conventional type Curie temperature) of 318K. It is considered to be a good candidate, since the ΔS_M value is $-30 J.K^{-1}Kg^{-1}$ and the ΔT_{ad} for $\Delta H = 5T$ is 13K.[54] Unfortunately, its usage is limited due to a considerably large thermal hysteresis and also due to the poisonous nature of arsenic. This has led to a strong effort to develop arsenic-free alloys with comparable, or even improved, magnetocaloric properties. Hence, the substitution of As by Sb in the compound, $Mn(As_xSb_{1-x})$ has shown a reduction in the thermal hysteresis and also a decrease in the transition temperature to 230K at x=0.3, whilst maintaining first-order magneto-structural properties. The MCE is reduced slightly such that, ΔS_M is in the range of -25 to $-30 J.K^{-1}Kg^{-1}$ and ΔT_{ad} for $\Delta H = 5T$ is 10K.[54-55] Moreover, through the addition of Fe and P, the alloy $MnFeP_xAs_{1-x}$ maintains first order transition properties near room temperature for $0.26 \leq x \leq 0.66$.[56] The Mn-Fe-P-Si compounds with a hexagonal Fe_2P-type structure are also promising candidates, since the GMCE exhibited can be tuned by varying the Mn:Fe, P:Si ratio.

In addition, the thermal hysteresis can be reduced simultaneously.[57] Ferromagnetic Heusler alloys such as Ni-Mn-Z (Z = Ga, In, Sn, Sb), which exhibit either a positive or negative MCE, depending on their stoichiometry, have attracted much attention in recent years. In non-stoichiometric $Ni_{2+x}Mn_{1-x}Ga$ alloys, a coupled magneto-structural transition from FM-martensite to PM-austenite takes place.[58-59-60] A positive MCE is displayed in the composition range of $0.18 \leq x \leq 0.27$. The reasoning behind the large MCE exhibited by such materials is related to the sum of entropy changes associated with the transition. Such field-induced magneto-structural transitions resulting from the coupling of magnetic and structural degrees of freedom are promising features for magnetocaloric applications.

4. Manganites antiperovskite compounds

Mn-based antiperovskite with the general formula Mn_3AX, (A: Al, Zn, Ga, Ge, Sn, In) and (X: C, N, B), show a large variety of magnetic ordering configurations and magneto structural transitions with narrow hysteresis properties.[61-62] These compounds have an antiperovskite or

metallic perovskite structure with *Pm*-3*m* symmetry. Fig.22a shows the unit cell of Mn_3GaC.The carbon atom is located at the (1/2, 1/2, 1/2) position in the center of an octahedron of Mn atoms, and the Ga atoms are located at (0, 0, 0).[63] The cubic cell has a lattice constant of 0.896 nm.[64-65-66-67]

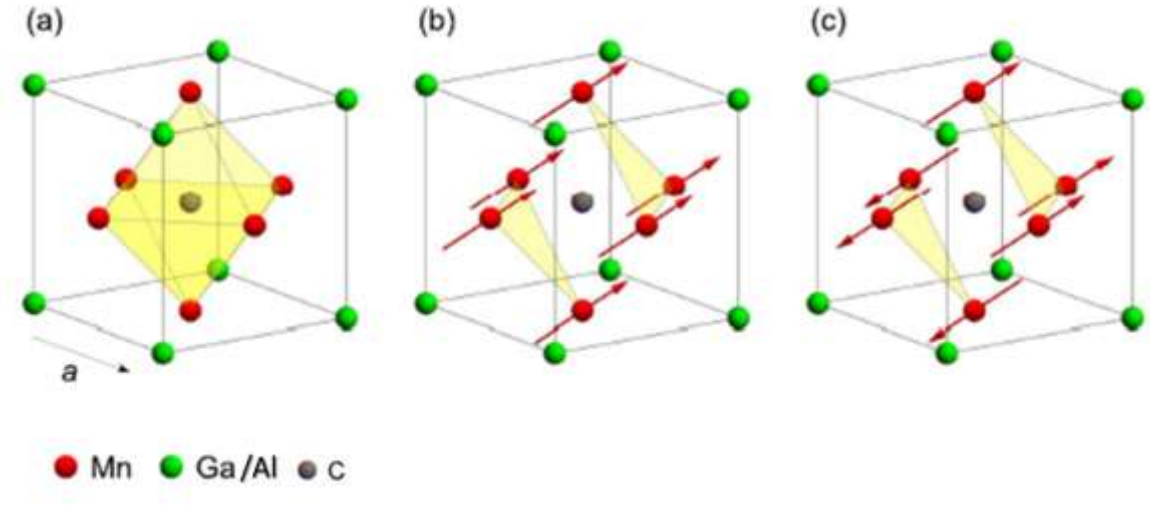

Figure 22. *(a) Antiperovskite Mn_3GaC Pm−3m structure. Ferromagnetic (b) and antiferromagnetic (c) structure of Mn_3GaC.[68-69]*

Mn_3GaC has been investigated due to its narrow hysteresis at the first-order transition. It was found to exhibit a first-order transition at Ti = 160K from a low temperature antiferromagnetic (AF) state to a high-temperature ferromagnetic state (FM), which is accompanied by a decrease in the volume of the unit cell of about 0.56%, while the structure of the alloy remains cubic. The transition can be regarded as a first-order magneto-structural transition, which is verified by the rapid change of the heat capacity of Mn_3GaC at Ti,[69] with an inverse MCE. Otherwise at the Curie temperature T_C=249K Mn_3GaC shows a second phase transition from the FM state to the paramagnetic state (PM) with a conventional MCE.[61] As mentioned above, at the first order transition, Mn_3GaC shows an inverse MCE with a ΔT_{ad} of about 5K in a field change ΔH of 2T.[70]

4.1 Tuning the transition of Mn_3GaC.

Mn_3GaC has several advantages in being doped with various elements. Many studies were conducted to tune the transition of Mn_3GaC, such as doping Mn with several elements such as Fe, Ni, Co and Cr.[71-72]

Toh et al. showed that by doping Mn with Co ($0 <= x <= 0.05$), the first transition temperature Ti is decreased to 100K with the increase of percentage doping.[66] While the magnetic entropy change ΔS_m is not being affected by the doping and the MCE is being in a large temperature range between 50 and 160K which makes these alloys promising candidates for low

temperature magnetic refrigeration.[71] Doping with Ni was also performed, it was observed that an intermediate canted FM state appeared between the AF and the FM state. The transition temperature between the FM and the canted FM decreases with increasing x. As well as between the canted FM state and the AF. Moreover, T_c from the FM to PM state is increasing with the increase of Ni doping. The shift of transition temperature towards lower temperatures can therefore be explained as a combination of a chemical pressure effect and a correlating electronic band filling effect due to the substitution of Mn with Ni.[73] Similar to the doping with Ni, Fe has shown similar behavior consisting in an intermediate state between AF and FM phase. Contrary to these two doping with Cr (0<=x<=0.05) shows no presence of an intermediate FM state. In fact, the state is totally absent at x >0.15%, and the transition becomes direct from the AF phase to the PM phase. In addition to that Tc decreases with increasing the percent of doping. Another possible option, is to substitute with Al or Sn.[74]

Mn_3SnC alloy show no difference between the AF and the FM phase but exhibits a ferrimagnetic state. This alloy undergoes a first-order transitions to the PM phase at Tc~279K with a thermal hysteresis of ~2.5K.[75] The entropy change of this alloy at the PM transitions is similar to the one of Mn_3GaC which makes this alloy also an interesting choice for magnetocaloric application.

A further possibility to shift T_i to higher temperatures, is by substituting carbon to nitrogen. The thermal hysteresis of Mn_3GaC can be reduced by substituting C to N, whereas the hysteresis disappears for $Mn_3GaC_{0.85}N_{0.15}$.[76-77] At 185K, the first and second order transitions for $Mn_3GaC_{0.85}N_{0.15}$ coincides and the alloy transforms from an AF to and enhanced paramagnetic state PM without long range FM ordering.

4.2. Magnetocaloric properties of Mn_3GaC

Yu et al. have discovered a giant negative MCE in the antiperovskite Mn_3GaC alloy.[78] This giant MCE is related to the first order AF–FM transition at T_i =160K. The most fascinating, is that both the value of the magnetic entropy changes ($-\Delta S_m$) and the adiabatic temperature change (ΔT_{ad}) show a plateau like temperature dependencies with maximum values of about 15J/kg·K and 5.4 K at ΔH = 20 kOe, respectively. By increasing the magnetic field, the value of ($-\Delta S_m$) is almost constant but the temperature span induces a significant broadening. However, due to the first-order transition, the thermal hysteresis adversely affects the reversibility of the MCE and the usefulness of the material as a magnetic refrigerant. In comparison to the first-order AF–FM transition, little attention has been paid to the MCE with respect to the second-order FM–PM transition at T_C =249K which is close to room temperature.

Therefore, in order to explore the new room-temperature MCE materials, we investigated the MCE around T_C in Mn_3GaC,[79] which is the goal treated in this thesis. As illustrated in Fig.23a, the maximum magnetic entropy change $-\Delta S_m$ reaches 2.52J/kg·K for a ΔH =20kOe. With increasing the magnetic field to ΔH =20kOe, the maximum magnetic entropy increases to $-\Delta S_m$ =4.30 J/kg·K These results indicate that $MnGa_3C$ compound sample is a good substance for magnetic refrigeration applications

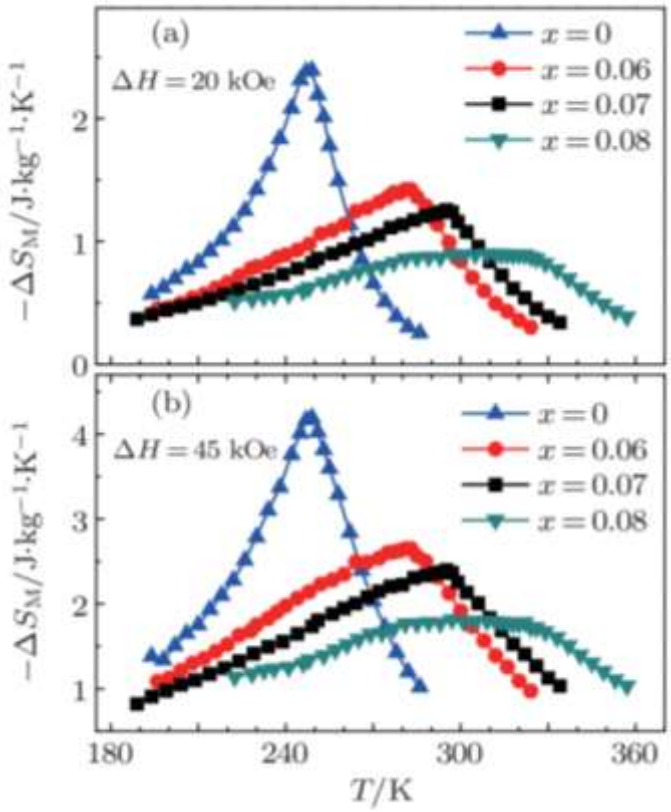

Figure 23. *Magnetic entropy change $-\Delta S_m(T)$ as a function of temperature under magnetic field changes of ΔH=20 kOe (a) and 45 kOe (b) for $Ga_{1-x}CMn_{3+x}$* [73]

4.3. Magnetocaloric properties of Mn_3AlC

Mn_3AlC is a FM material with a curie temperature $T_C \sim 288$ K[80] with a lattice parameter of 0.3873 nm, and it has the same crystalline structure of Mn_3GaC. The magnetic transition at T_C was confirmed to be second-order transition without thermal hysteresis. As shown in Fig. 24a, the maximum magnetic entropy change $-\Delta S_M$ reaches 3.28 J/kg·K for a ΔH = 45 kOe. With increasing ΔH, the values of $-\Delta S_M$ and ΔT_{ad} increase gradually and reach the maximum values (3.28 J/kg·K and 1.62 K for ΔH = 45 kOe). The RCP value of Mn_3AlC is 137 J/kg, and 328 J/kg for ΔH=20, and 45 kOe, respectively (Fig. 24b). The RCP value for ΔH=45 kOe is 1.5 times of that of Mn_3GaC.

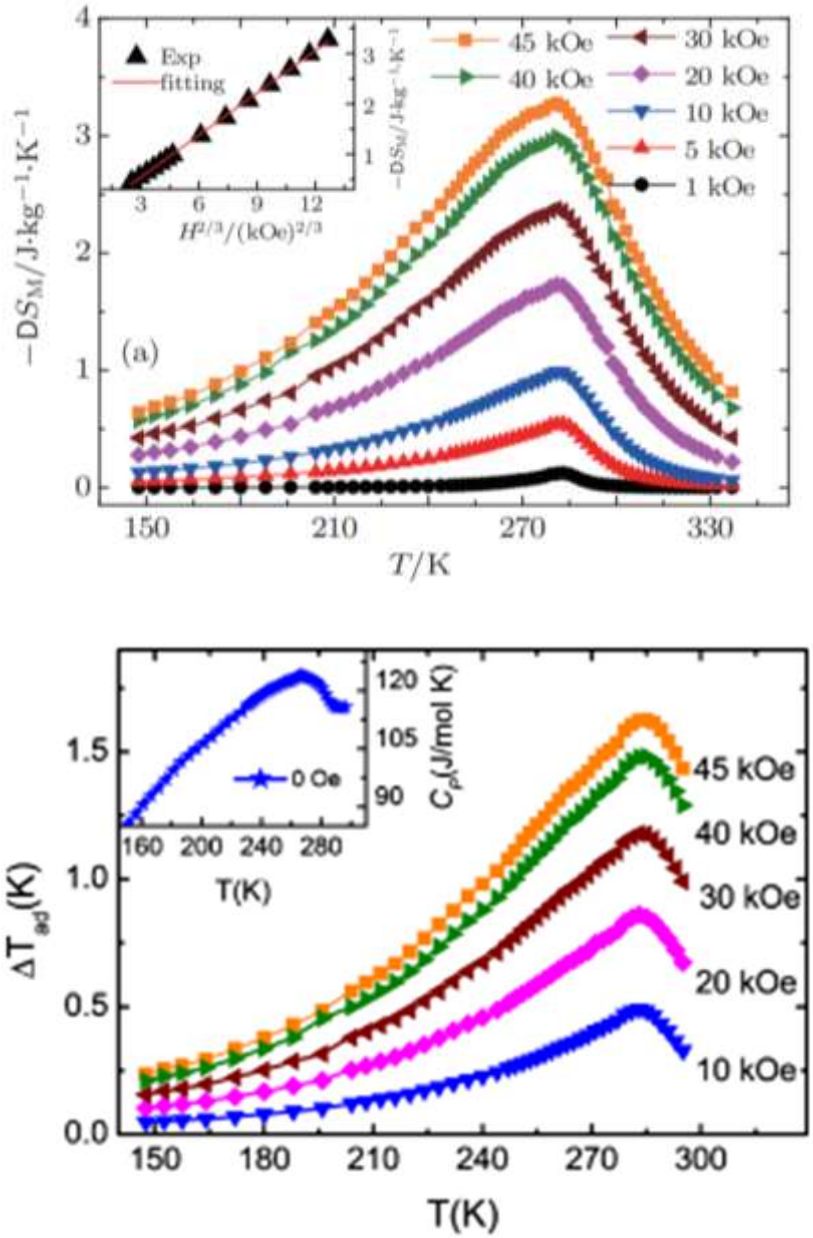

Figure 24. *(a) Magnetic entropy change −ΔSM(T) with various magnetic field changes for AlCMn3.*[81] *Inset shows the maximum magnetic entropy change −ΔS max M at T_C as a function of $H^{2/3}$ for AlCMn3. The solid line shows the linear fit to the experimental data. (b) The $-\Delta S_M(T)$ curve for magnetic field change ΔH = 45 kOe. The shaded area is the RCP. The inset shows the magnetic field dependence of RCP*

5. $CoFe_2O_4$ spinel ferrites.

5.1. Spinel ferrites

The word spinel originates from Italian "spinella", diminutive of spine. Also called as cubic ferrites most of the spinel compounds have space group Fd_3m. At least 30 oxide minerals are included in the spinel super group. The principal member of the group has the formula, AB_2O_4; the '*A*' represents a divalent metal ion such as magnesium, iron, nickel, manganese and zinc.

While, the '*B*' represents trivalent metal ions such as aluminum, iron, chromium and/or manganese. In most oxide structures, the oxygen ions are appreciably larger than the metallic ions and the spinel structure can be approximated by a cubic close packing of O_2^- ions in which the cations (e.g. Co_2^+, Fe_3^+) occupy certain interstices. Several different types of cation grouping may exist in a spinel structure with a net charge eight to equalize the anion's net charge, for example $Co^{2+}Fe_2^{3+}O_4$, $Mg_2^{2+}Ti^{4+}O_4$, $Li^{1+}Al^{3+}Ti^{4+}O_4$, $Li_{0.5}^{1+}Al_{2.5}^{3+}O_4$ and $Na_2^{1+}W^{6+}O_4$, etc. Thus, Spinel ferrites make the most widely useable ferrites group.[82]

5.2. Crystal structure of the spinel ferrites

In 1915 and for the first time Bragg and Nishikawa determined the structure of spinel. The unit cell of the latter has a cubic lattice, composed with two kinds of alternately repeating sub cells in the three-dimensional arrays. The smallest cell of the spinel lattice that has cubic symmetry contains eight "molecules" of $MeFe_2O_4$. The relatively large oxygen ions form an fcc lattice. Spinel ferrites have a cubic close-packed arrangement of oxygen anions with divalent metal cations and trivalent Fe^{3+} at two different kinds of crystallographic sites called tetrahedral sites (A sites) and octahedral sites (B sites) respectively as given in Figure 25.[83] The two sites (A) and (B) are surrounded by 4 and 6 oxygen atoms respectively. The cubic unit cell with spinel crystal structure ferrites is shaped by 56 atoms, 32 of oxygen atoms spread in a cubic close packed configuration (CCP) whereas 24 metal cations are distributed among 8 A sites and 16 B sites. Total available A sites are 64 but only 8 are occupied while available B sites are 32 from which only 16 are occupied for charge neutrality.[84] In a tetrahedral site (A), the interstitial is in the center of a tetrahedron formed by four lattice atoms. Three atoms, touching each other, are in plane; the fourth atom sits in the symmetrical position on top. Again, the tetrahedral site has a defined geometry and offers space for an interstitial atom. An octahedral sites (B) for an (interstitial) atom is the space in the interstices between 6 regular atoms that form an octahedron. Four regular atoms are positioned in a plane; the other two are in a symmetrical position just above or below as shown in Fig. 26.

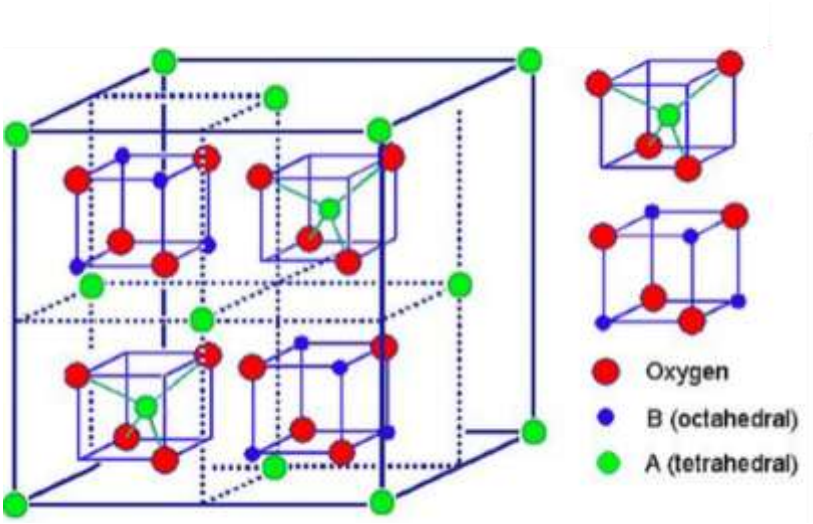

Figure 25. *A spinel unit cell structure showing oxygen atoms, tetrahedral A sites, and octahedral B sites.*[77]

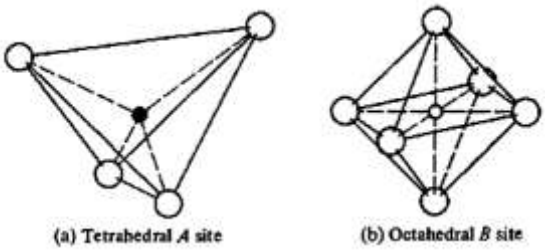

Figure 26. *(a) Tetrahedral A sites (b) Octahedral B site.*

5.3. Classification in spinel ferrites

Based on the coulombic energy of charged ions[85-86] and their influence in the polarization of anions,[87] large divalent ions favor tetrahedral occupancy and large trivalent ions favor octahedral occupancy. Thus, On the basis of cation allocation at interstices the spinel ferrites are placed in three groups.

(1) Normal spinel structure: $\delta = 1$

(2) Inverse spinel structure: $\delta = 0$

(3) Mixed spinel structure: $0 < \delta < 1$

5.3.1. Normal spinel ferrites.

Normal spinel ferrites: In normal spinel ferrites all Me^{2+} ions occupy tetrahedral sites i.e. 8 bivalent cations occupy 8 tetrahedral sites and 16 trivalent cations occupy 16 octahedral sites. Structural formula of such ferrites is $Me^{2+}[Fe_2^{3+}]O_4^{2-}$. Zinc ferrites $Zn^{2+}[Fe^{2+}Fe^{3+}]O_4^{2-}$ belong to this class. The normal spinel ferrites are illustrated in the figure below.

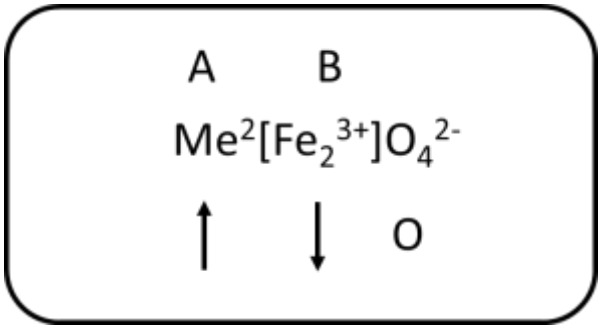

5.3.2. Inverse spinel ferrites

All Me^{2+} are in octahedral sites and Fe^{3+} ions are equally distributed between tetrahedral and octahedral sites in inverse spinel ferrites. The structural formula of these ferrites is $(Fe^{3+})[M^{2+}Fe^{3+}]O_4^{2-}$. Fe_3O_4, $NiFe_2O4$ and $CoFe_2O_4$ have inversed spinel structure. Inverse spinel ferrites are illustrated in the figure below.

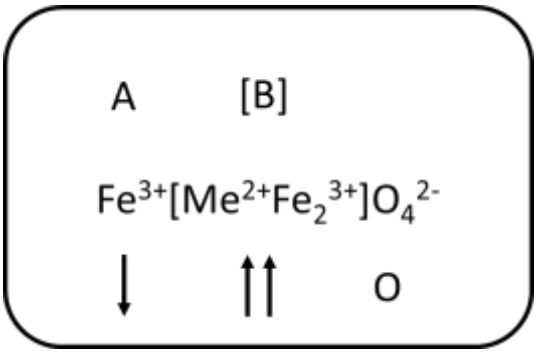

5.3.3. Mixed spinel ferrites:

If the bivalent cations (Me^{2+}) are present on both tetrahedral and octahedral sites, the spinel is mixed spinel structure. Structural formula of such ferrites is $Me_{1-\delta}^{2+}Fe_{\delta}^{3+}[Me_{\delta}^{2+}Fe_{2-\delta}^{3+}]O_4^{2-}$. $MnFe_2O^4$ is an important candidate for this type of structure and has an inversion degree of ∇=0.2 and its structural formula therefore is $Mn_{0.8}^{2+}Fe_{0.2}^{3+}[Me_{0.2}^{2+}Fe_{1.8}^{3+}]O_4^{2-}$. Mixed spinel ferrites are illustrated below.

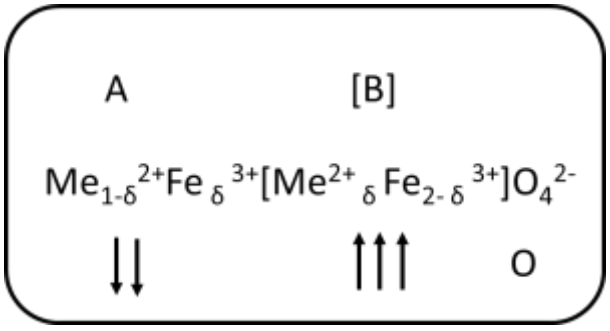

5.4. Spinel ferrites applications.

Ferrites are considered to be better magnetic materials compared to pure metals due to their high resistivity, lower cost, easier manufacture and superior magnetization properties. Ferrites

are also extensively used for many applications such as in radar, audio-video and digital recording, bubble devices, memory cores of computers, satellite communication and microwave devices.[88-89-90] Ferrite has a vast application from microwave to radio frequencies. It is used for antenna cores in radio receivers, fly back transformer in TV picture tube, broad band transformer, mechanical filter, ultrasonic generator, moderators, phase shift, isolators.

Cobalt is well known because of its ability to reduce magnetic losses at high frequencies. Among spinel ferrites, cobalt ferrite $CoFe_2O_4$ is especially interesting because of its applications in biotechnology,[91] magnetic storage appliances[92] and in high frequency devices.[93] $CoFe_2O_4$ has high cubic magneto crystalline anisotropy, high coercivity and moderate saturation magnetization. Cobalt ferrite nanocrystalline particles as a photo-magnetic material show interesting light-induced coercivity change.[94] Many biotechnological applications have been developed depending upon biogenic and synthetic nanoparticle.[95] In magnetic resonance imaging (MRI), super paramagnetic particles are selectively associated with healthy tissues because these particles change the rate of proton decay from the excited to the ground state. Consequently, a disparate and darker contrast is obtained from these healthy regions of tissue. [96-97] Thermal energy obtained from hysteresis loss of ferrites is used in heating of specific tissues for treatment of cancer (hyperthermia).[98] Grain dimensions, chemical composition, crystallinity, and cations allocation play an influential role in defining the properties of nano ferrite particles. Furthermore, the structural, magnetic and electrical properties of ferrites are very much sensitive to synthesis conditions.

5.5. $CoFe_2O_4$ at nanoscale levels

In the last decade, research on nanoscale structures has been mainly driven by their peculiar properties in comparison to bulk structures that generally show constant physical properties. For instance, the improvement of magnetic properties through tailoring size and morphology of nanoscale magnetic materials is the main impetus behind the extensive work on fabricating $CoFe_2O_4$ nanostructures.[99] Among these nanostructures, we can cite different morphologies such as nanoparticles, nanowires and nanorods, which could be processed via several methods, namely co-precipitation,[100] thermal decomposition,[101] hydrothermal method,[102] pulsed laser deposition,[103] electrodeposition[104] and chemical methods.[93] Most recently self-ordering electrochemical method have been successfully used to prepare highly ordered oxide nanostructures.[105,106]

Chapter II: Computations theory and experimental methods

1. Introduction

One of the fundamental problems in condensed-matter physics and quantum chemistry is the theoretical study of electronic properties of systems ranging from atoms and molecules to complex materials. Since electrons are governed by the laws of quantum mechanics, all these systems are fully described by the Schrodinger equation. Analytic solutions of the Schrodinger equation are obtainable for very simple systems only. However, for systems with large number of atoms, the electrostatic repulsion between the electrons makes its numerical resolution very difficult. In that case, it is natural to consider the many-electron wave function Ψ (r_1, r_2, r_i….) with appropriate approximations. The earliest and widely used approximation was that of Hartree[107], which expresses the wave function of system as a product of one-electron wave functions, so that the problem reduces to a one-electron Schrodinger equation. Then, considerable improvement of the energy computation was made by incorporating the exchange effects with the so-called Hartree-Fock approximation[108], which replaces the product of one-electron wave functions by a linear combination of orbitals[109].

2. Density Functional theory

2.1. The Electronic Structure Problem.

A major goal of electronic structure calculations is to solve the non-relativistic time independent Schrodinger equation, for system of many electrons and nuclei:

$$\hat{H}\Psi(r) = E\Psi(r) \qquad (1)$$

Where $\hat{H}$ is the Hamiltonian operator:

$$\hat{H} = \hat{T}_e + \hat{T}_N + \hat{V}_{e-e} + \hat{V}_{N-N} + \hat{V}_{e-N} \qquad (2)$$

In Eq. (2), $\hat{T}_e$ and $\hat{T}_N$ are is the kinetic energy operators of electrons and ions, $\hat{V}_{e-e}$ is the electron-electron interaction operator, $\hat{V}_{N-N}$ is the corresponding nucleus-nucleus repulsion interaction term, and $\hat{V}_{e-N}$ is the electrostatic electron-nucleus attraction operator. In terms of the electron and nucleus coordinates these parts of the Hamiltonian can be written as:

$$H = \sum_{i=1}^{n} \frac{-\hbar^2\nabla_i^2}{2m} + \sum_{\alpha=1}^{N} \frac{-\hbar^2\nabla_\alpha^2}{2M_\alpha}$$

$$-\sum_{i=1}^{n}\sum_{\alpha=1}^{N} \frac{Z_\alpha e^2}{|r_i - R_\alpha|} + \frac{1}{2}\sum_{\mathrm{i,i'\#j}} \frac{\mathrm{K}e^2}{|r_i - r_j|} + \frac{1}{2}\sum_{\alpha\#\beta} \frac{Z_\alpha Z_\beta k e^2}{|R_\alpha - R_\beta|}$$

$$\hat{T}_e = -\frac{1}{2}\sum_i \nabla_i^2 , \hat{V}_{e-N} = \sum_i [\sum_I V(R_I - R_i)], \text{ and } \hat{V}_{e-e} = \sum_i \sum_{j>i} \frac{1}{r_i - r_j^i} \qquad (3)$$

In Eq. (1), Ψ is the wave function and E is the eigen-energy of the system. In the case of a system with N-nuclei, and n-electrons, the wave function Ψ is a function of both electronic and nuclei coordinate:

$$\psi = \psi_1(r_1, r_{2,} \dots\dots\dots r_n;\ R_1, R_2, \dots\dots R_N),$$

i.e. it depends on 3n+3N variables, which makes obtaining the solution very complicated. Thus, in order to describe the system properties, one needs to make some approximations.

2.1.1. The Born-Oppenheimer

Due to smaller mass, electrons move much faster than the nuclei. Thus, electrons rapidly adjust themselves to the change in nucleus coordinates and one can decouple the electronic and nucleus degrees of freedom in solving Eq. (1):

$$\psi = \psi_1(r_1, r_{2,} \dots\dots\dots r_n;\ R_1, R_2, \dots\dots R_N) = \sum_\nu \Lambda_\nu(R)\Phi_\nu, (r_1, r_{2,} \dots\dots\dots r_n) \qquad (4)$$

Where, Φ is the wave function of electrons for a fixed set of nucleus coordinates R. In this case, the Schrodinger equation for the electronic part of the system can be written as:

$$H^e \Phi(r_1, r_{2,} \dots\dots\dots r_n) = E_\nu^e \Phi(r_1, r_{2,} \dots\dots\dots r_n) \qquad (5)$$

Where,

$$H^e = \hat{T}_e + \hat{T}_N + \hat{V}_{e-e} + \hat{V}_{e-N} \qquad (6)$$

And

$$\hat{V}_{N-N} = \frac{1}{2}\sum_{i\neq j} \frac{Z_i Z_j}{R_{ij}} \qquad (7)$$

(Z_i is the nucleus (ion) charge).

After one obtains the solution of Eq. (2.6), one can calculate new positions of the ions by finding the minimum for energy of the system:

$$E^{BO} = \frac{1}{2}\sum_{i\neq j} \frac{Z_i Z_j}{R_{ij}} + E_e(R) \qquad (8)$$

The procedure is repeated until the converged solution for the electronic and ionic system is obtained. This algorithm forms the basis of the Born-Oppenheimer approximation (BOA).

Despite the great simplification of the BOA, one still needs to take care of a huge number of electronic degrees of freedom in the Schrödinger equation, i.e. one need to properly take into account many-electron effects.

2.1.2. Hartree and Hartree-Fock approximation

In the simplest approximation, proposed by Hartree[110], it is assumed that the electrons don't interact with each other, so the many-electron wave function can be approximated by a product of single-electron orbitals:

$$\psi(\vec{r_1}, \vec{r_2} \dots \dots \dots . \vec{r_n}) = \varphi_1(\vec{r_1})\varphi_2(\vec{r_2}) \dots \dots \dots \varphi_n(\vec{r_n}) \qquad (9)$$

In this case, Eq. (2.6) reduces to the following equation:

$$[-\tfrac{1}{2}\nabla_i^2 + \textstyle\sum_I V(R_I - \vec{r_i}) + \sum_{j\neq i} \int \left|\varphi_j(\vec{j})\right|^2 \frac{1}{|\vec{r_j} - \vec{r_i}|} d\vec{r_j}]\, \varphi_i(\vec{r_i}) = \varepsilon\varphi_i(\vec{r_i}) \qquad (10)$$

which can be rather easily solved numerically.

The third term in the square brackets in Equation (10) is an electrostatic potential experienced by the electron in the $i\ th$ state due to the other electrons. Thus, the problem reduces to one-electron equations, which can be solved self-consistently, for example by using an iterative procedure.

In the Hartree approximation, Equation (10), the electrons are interacting with each other only via the effective field; direct interactions between electrons are missing. Also, due to fermionic nature of electrons, their wave function must satisfy certain properties, missing in the Hartree approximation. Namely, the fermion wave function must be antisymmetric with respect to interchanging each-pair of electrons:

$$\psi\left(\vec{r_1}, \vec{r_2} \dots, \vec{r_j}, \dots, \vec{r_k} \dots, \vec{r_n}\right) = -\psi\left(\vec{r_1}, \vec{r_2} \dots, \vec{r_j}, \dots, \vec{r_k} \dots, \vec{r_n}\right) \qquad (11)$$

The property can be satisfied if one writes the electron wave function in the form of Slater determinant:

$$\psi(\vec{r_1}, \vec{r_2} \dots, \vec{r_n}) = \frac{1}{\sqrt{n!}} \begin{vmatrix} \varphi_\alpha(\vec{r_1}) & \varphi_\beta(\vec{r_1}) & \dots & \varphi_\nu(\vec{r_1}) \\ \varphi_\alpha(\vec{r_2}) & \varphi_\beta(\vec{r_2}) & \dots & \varphi_\nu(\vec{r_2}) \\ \dots & \dots & \dots & \dots \\ \varphi_\alpha(\vec{r_N}) & \varphi_\beta(\vec{r_N}) & \dots & \varphi_\nu(\vec{r_N}) \end{vmatrix} \qquad (12)$$

Indeed, changing two electrons is equivalent to change of two columns in the Slater matrix, which correspond to change of the sign of the determinant. Also, such a wave function satisfies

the Pauli Exclusion Principle, according to which one cannot have two electrons in the same state: determinant of the matrix with two or more equal columns is zero.

This approximation is called the Hartree-Fock (HF) approximation. In the HF approximation the one-electron equation is:

$$[-\frac{1}{2}\nabla_i^2 + \sum_I V(R_I - \vec{r_i})]\varphi_\lambda(\vec{r_i}) + [\sum_\mu \varphi_\mu^*(\vec{r_j}) \frac{1}{|\vec{r_j}-\vec{r_i}|} \varphi_\mu(\vec{r_j}) d\vec{r_j}]\varphi_\lambda(\vec{r_i}) -$$

$$[\sum_\mu \varphi_\mu^*(\vec{r_j}) \frac{1}{|\vec{r_j}-\vec{r_i}|} \varphi_\lambda(\vec{r_j}) d\vec{r_j}]\, \varphi_\mu(\vec{r_i}) = \varepsilon\varphi_\lambda(\vec{r_i}) \qquad (13)$$

The last term on the left-hand side of the equation describes the exchange interaction effects. As according to Pauli Exclusion Principle same-spin electrons cannot occupy the same state, it leads to a constraint in the electron motion, or an effective electron interaction. In most cases, the HF approximation is much more accurate than the Hartree approximation. Exchange interaction deals with same-spin electrons, forbidding them to be in the same state (site, momentum and so on). However, different spin electrons can occupy the same state, which in particular is the case of two electrons occupying the same orbital, which in the case of localized orbitals may lead to large increase of their (Coulomb interaction) energy. The part of the electron energy beyond the HF approximation is called correlation energy. While in typical metallic and semiconductor systems the latter is rather small, in strongly correlated materials it can be very large, and one needs to make further approximations to include this part of the interaction in the effective Hamiltonian. In any event, the solution of the HF equation is rather expensive, because of their many-particle character. Therefore, it would be desirable to reduce the many-electron problem to a single-electron one.

2.2. Density-Functional Theory

In the preceding section, we introduced several different ways to approximately solve the electronic Schrödinger equation such as the Hartree-Fock method, Møller-Plesset perturbation theory, and coupled cluster methods. These different methods share one common feature that they all rely on the many body wave function as a central quantity. Once the wave function is known, the energy of the system and all related properties will be determined. But the wave function itself is already a complicated quantity as it depends on 3N spatial variables together with the spin variable, where N is the number of electrons in the system. This severely limits the system sizes that can be treated with wave function-based methods. Certainly, systems with hundreds of atoms and large basis sets are beyond reach for most practical studies with wave function-based methods. DFT differs from the wave function-based methods by using the

electron density (ρ(r)) as the central quantity. The advantage of using the electron density over the wave function is the much-reduced dimensionality. Regardless of how many electrons one has in the system, the density is always 3 dimensional. This enables DFT to be applied to much larger systems, hundreds or even thousands of atoms become possible. Partly for this reason, DFT has become the most widely used electronic structure approach today, particularly in the condensed matter physics community. In this section, a basic introduction to DFT will be given. Authoritative and comprehensive discussions of DFT can be found in a range of excellent review articles[111,112,113,114] and textbooks [115,116].

2.2.1. Thomas-Fermi Theory

The history of using the electron density rather than the wave function begins with the early work of Thomas and Fermi[117,118] First, let us define the electron density.

$$\rho(r) = n \int \dots \int |\psi(x_1, x_2, \dots, x_N)|^2 ds_1 x_2 \dots x_N \qquad (13)$$

ρ(r) determines the probability of finding any of the N electrons within the volume r but with arbitrary spin while the other N−1 electrons have arbitrary positions and spin in the state represented by Ψ. This is a nonnegative simple function of three variables, x, y, and z, integrating to the total number of electrons,

$$\int \rho(r) dr = N \qquad (14)$$

In Thomas-Fermi theory, the kinetic energy of electrons is derived from the quantum statistical theory based on the uniform electron gas, but the interaction between electron-nucleus and electron-electron are treated classically. Within this model, the kinetic energy of the electrons is defined as,

$$T(\rho) = C_F \int \rho^{\frac{5}{3}}(r) dr \qquad (15)$$

With

$$C_F = \frac{3}{10}(3\pi^2)^{\frac{2}{3}} = 2.871 \qquad (16)$$

From the above equation, the approximation is made that the kinetic energy only of the electron depends exclusively on the electron density. By adding the interaction between electron-nucleus and electron-electron into Eq. (6), a total energy in terms of electron density is obtained,

$$E[\rho] = C_F \int \rho^{\frac{5}{3}}(r) dr - Z \int \frac{\rho(r)}{r} dr + \frac{1}{2} \iint \frac{\rho(r_1)\rho(r_2)}{|r_1 - r_2|} dr_1 r_2 \quad (17)$$

The second and third terms are the electron-nucleus and electron-electron interactions, respectively. The importance of this simple Thomas-Fermi model is not how well it performs in computing the ground state energy and density but more as an illustration that the energy can be determined purely using the electron density.

2.2.2. Hohenberg-Kohn Theorem

Modern density-functional theory was born in 1964 with the paper of Hohenberg and Kohn [119]. The two key results of this paper are: (i) a one to one mapping between external potential and electron density was established; (ii) it was shown that the ground state density can be found by using a variational principle. The first part was proved in a simple and extremely elegant manner using the principle of reduction ad absurdum, and this is derived for a non-degenerate system. Suppose there is a collection of electrons enclosed into a box influenced by an external potential v(r). We assume we know the electron density of this system and it also determines v(r) and thus all properties. If there is another external potential $v_0(r)$ which differs from v(r) by more than a constant that can also give the same electron density ρ(r) for the ground state, then we will have two different Hamiltonians $\widehat{H}$ and $\widehat{H}_0$ whose ground state electron density is the same but the normalized wave function Φ and Φ_0 would be different. Then we will have

$$E_0 < \Phi' \left| \widehat{H} \right| \Phi' > = < \Phi' \left| \widehat{H}' \right| \Phi' > + < \Phi' \left| \widehat{H} - \widehat{H}' \right| \Phi' > = E_0' + \int \rho(r)[v(r) - v(r)']dr \quad (18)$$

Where E_0 and E_0' are the ground-state energies for $\widehat{H}$ and $\widehat{H}'$, respectively. Similarly, we can get

$$E_0' < \Phi \left| \widehat{H} \right| \Phi > = < \Phi \left| \widehat{H} \right| \Phi > + < \Phi \left| \widehat{H}' - \widehat{H} \right| \Phi > = E_0 + \int \rho(r)[v(r) - v(r)']dr \quad (19)$$

Adding Eq. (18) and Eq. (19), we will obtain

$$E_0 + E_0' < E_0' + E_0 \quad (20)$$

This is an obvious contradiction. So, there are no two different external potentials that can give the same ρ(r). Thus ρ(r) uniquely determines v(r) and all ground state properties. Now we can write the energy E explicitly as a function of the electron density ρ(r):

$$E[\rho] = T[\rho] + T_{ne}[\rho] + V_{ee}[\rho] = \int \rho(r)v(r)dr + F_{HK}[\rho] \quad (21)$$

Here

$$F_{HK}[\rho] = T[\rho] + V_{ee}[\rho] \quad (22)$$

Herein, we note that $F_{HK}[\rho]$ is only dependent on ρ and independent from any external potential v(r). Thus $F_{HK}[\rho]$ is a universal functional of ρ. The second Hohenberg-Kohn theorem demonstrates that that the ground state energy can be obtained variationally, with the density that minimizes the total energy being the exact ground state density. This is expressed as:

$$E_0[\rho_0] \leq E_v[\rho] \qquad (23)$$

Where $E_v[\rho]$ is the energy functional of Eq. (21). Following from the first part of the theorem, suppose the ground state wave function is Φ and its related electron density is ρ. Thus, the ρ uniquely defined the external potential v(r). If there is another wave function Φ_0 with an arbitrary variation from Φ and its electron density is ρ_0, then we can obtain,

$$< \Phi' \left| \widehat{H} \right| \Phi' >= \int \rho'^{(r)} v(r) + F_{HK}[\rho'] = E[\rho'] \geq E[\rho] \qquad (24)$$

So, the energy will reach the minimum only when the electron density is the ground state electron density.

2.2.3. The Kohn-Sham Equations

From the Hohenberg-Kohn theorem, we can get the ground-state energy by minimizing the energy functional,

$$E[\rho] = \int \rho(r) v(r) dr + F_{HK}(\rho(r)) \quad (25)$$

Although the Hohenberg-Kohn theorem provided a proof in principle that the total energy could be obtained from the ground state density it was not yet known how to obtain the ρ(r) or FHK(ρ(r)). In 1965, Kohn and Sham[120] published a paper which transformed density-functional theory into a practical electronic structure theory. Kohn and Sham recognized that the failure of Thomas-Fermi theory mainly resulted from the bad description of the kinetic energy. To address this problem, they decided to re-introduce the idea of one electron orbitals and approximate the kinetic energy of the system by the kinetic energy of non-interacting electrons. This led to the central equation in Kohn-Sham DFT which is the one-electron Schrödinger-like

$$\left(-\frac{1}{2}\nabla^2 + v(r) + \int \frac{\rho(r')}{|r-r'|} dr' + v_{xc}(r) \right) \phi_i' = \varepsilon \phi_i \qquad (26)$$

Here φ are the Kohn-Sham orbitals and the electron density is expressed by,

$$\rho(r) = \sum_i^N |\phi_i|^2 \qquad (27)$$

The terms on the left side of Eq. (26) are the kinetic energy of the non-interacting reference system, the external potential, the Hartree potential, and exchange-correlation potential, respectively. The ε is the energy of the Kohn-Sham orbital. In addition, the exchange-correlation potential is given by,

$$v_{xc}(r) = \frac{\delta E_{xc}}{\delta \rho(r)} \qquad (28)$$

and $E_{xc}[\rho]$ is the exchange-correlation functional which will be discussed later. Furthermore, we can define an effective potential (v_{eff}) which is,

$$v_{eff} = v(r) + \int \frac{\rho(r')}{|r-r'|} dr' + v_{xc}(r) \qquad (29)$$

This allows Eq. (26) to be rewritten in a more compact form,

$$\left(-\frac{1}{2}\nabla^2 + v_{eff}\right)\phi_i = \varepsilon\phi_i \qquad (30)$$

Clearly this is a Hartree-Fock like single particle equation which needs to be solved iteratively. Finally, the total energy can be determined from the resulting density through

$$E = \sum_i^N \varepsilon_i - \frac{1}{2}\iint \frac{\rho(r)\rho(r')}{|r-r'|} dr dr' + E_{xc}[\rho] - \int v_{xc}(r)\rho(r) dr \qquad (31)$$

Equations (30), (27), and (28) are the celebrated Kohn-Sham equations. Note that the v_{eff} depends on ρ(r) through Eq. (29). So, the Kohn-Sham equation must be solved self-consistently. The general procedure is to begin with an initial guess of the electron density, construct the v_{eff} from Eq. (29), and then get the Kohn-Sham orbitals. Based on these orbitals, a new density is obtained from Eq. (27) and the process repeated until convergence is achieved. Finally, the total energy will be calculated from Eq. (31) with the final electron density. If each term in the Kohn-Sham energy functional was known, we would be able to obtain the exact ground state density and total energy. Unfortunately, there is one unknown term, the exchange-correlation (xc) functional (E_{xc}). E_{xc} includes the non-classical aspects of the electron-electron interaction along with the component of the kinetic energy of the real system different from the fictitious non-interacting system. Since E_{xc} is not known exactly, it is necessary to approximate it, which is the focus of the next section.

2.3. Exchange-Correlation Functionals

"Density functional theory is in principle exact! But, in practice approximations have to be made." W. Kohn Oct. 14, 1997 Laboratoire de Chimie Theorique Universite Pierre et Marie

Curie Paris, France to use the Kohn-Sham equations we must know what the form of the exchange-correlation energy functional is. However, the exact form of E_{xc} is not known and may never be known (in some simple closed form). Thus, since the birth of DFT some sort of approximations for E_{xc} have been used. By now there is an almost endless list of approximations with varying levels of complexity. Rather recently a useful way for categorizing the many and varied Exc functionals that exist has been proposed by Perdew and is known as "Jacob's ladder" [121]. In this scheme functionals are grouped according to their complexity on rungs of a ladder which lead from the Hartree approximation on "earth" to the exact exchange-correlation functional in "heaven". We now very briefly discuss the first few rungs of this ladder

as a means to introduce some of the most common types of exchange-correlation functionals in widespread use:

(a) The local-density approximation (LDA): This is simplest approximation, and can be written as:

$$E^{xc-LDA}[\rho(r)] = \int \rho(r)\varepsilon^{xc-unif}\rho(r))d(r) \qquad (32)$$

where $\varepsilon^{xc-unif}$ is the exchange-correlation energy per particle of the homogeneous electron gas of density ($\rho(r)$), i.e. the exchange-correlation energy density is taken to be that of a uniform electron gas of the same density. The exchange energy is known exactly and the correlation energy is obtained by fitting to the many body studies of Gell-Mann and Brueckner and Ceperly and Alder[122,123]. Modern LDA functional tend to be exceedingly similar, differing only in how their correlation contributions have been fitted to the many-body free electron gas data. The Perdew-Zunger (PZ) [124], Perdew-Wang (PW) [125], and Vosko-Wilk-Nusair (VWN) [126]functionals are all common LDA functionals. Strictly, the LDA is valid only for slowly varying densities. Experience with calculations of atoms, molecules, and solids shows that Eq. (2.32) can in general also be applied to these systems. Indeed, LDA works surprisingly well and much current understanding of metal or semiconductor (Si or GaAs) surfaces comes from LDA simulations. A partial rationalization of the success of LDA is provided by the observation that it satisfies a number of so-called sum rules.[127,128,129,130]

(b) The generalized gradient approximation (GGA): These are the second generation functionals (sitting on the second rung of Jacob's ladder) in which the gradient of the density, $\nabla\rho(r)$, at each coordinate is taken into account as well as the density itself:

$$E^{xc-GGA}[\rho(r)] = \int \rho(r)\varepsilon^{xc-unif}\rho(r))\nabla\rho(r)d(r) \quad (33)$$

Thus, GGAs are "semi-local" functionals, comprising corrections to the LDA while (again) ensuring consistency with known sum rules. For many properties, for example geometries and ground state energies of molecules, GGAs can yield better results than the LDAs. Although for the properties of metals and their surfaces, GGA results are not necessarily superior to LDA results. The most widely used GGAs in surface physics are the PW91[131] functional, and its close relative PBE [132]. PBE actually has several off-spring; revPBE [133], PBE-WC [134], and PBEsol [135].

2.3.1. Linearized Augmented Plane Wave (LAPW) Method

Augmented plane wave method is a nonlinear method. This method is very slow in terms of computational time. Since u_l have to be determined with the guessed values of energy of eigen states. Moreover, energy at the muffin tin boundary is not smooth. This problem has been overcome by using Linearized augmented plane wave method.

In this method Taylor series expansion is employed by expanding u_l around E_l.

$$u_l(r) = u_1(r) + (E_1 - E_l^1)\frac{du_1(r)}{dE_1} + O((E_1 - E_l^1)^2 \qquad (34)$$

Linearized augmented plane waves (LAPW) can be written as [136]

$$\varphi_{Kn}^{APW}(r) = \begin{cases} \sum_{lm}[A_{lm,Kn}u_1(r) + B_{lm,Kn}\dot{u}_1]Y_{lm}(r) & (r\ \varepsilon\ MT) \\ \frac{1}{\sqrt{V}}e^{iKn.r} & (r\ \varepsilon\ I) \end{cases} \qquad (35)$$

It is clear that wave function is determined by ul and its energy derivative in muffin tin region. Therefore, LAPW can be regarded more adaptable as compared to APW. In both plane wave methods namely APW and LAPW the level of accuracy is determined by the product of $R_{min}.K_{max}$. It means highest accuracy can be attained by smallest muffin tin radius (unless core charge does not leak out of muffin tin sphere) and largest wave vector K_{max} (G_{max}). Small value of R requires small wavelength of plane waves to describe an atom near the nucleus. Large value of R is inappropriate because atomic functions are not suitable to describe the region far from the nucleus. On the other hand, if large value of Kmax and hence G_{max} are chosen than it would make calculations expensive in terms of computing cost. Therefore, DFT calculations require interplay between the values of R and K(G).

2.4. The WIEN2k supporting code

The WIEN2k code based on FP-(L) APW method is used to solve the Kohn-Sham equations for present work. Its first public version was released by P. Blaha and K. Schwarz in 1990. It is in progress till now. There are two main parts of the WIEN2k code to perform calculations on the particular crystalline solid as shown in the figure below. These are the Initialization and the

self-consistent field cycle (SCF). Each of these portions has numerous independent programs linked via shell scripts. There are several other analytical tools to determine a large number of physical properties e.g. charge density, band structure, and elastic properties et cetera. First section initializes the calculation by generating structure file and computing nearest neighbor distances. Also, it checks whether muffin tin spheres are overlapping. Afterwards a new structure file is generated supporting given space group. Next the symmetry operations are performed and the k-mesh is obtained in full brillouin zone. Finally, it estimates the input trial density for iterations. Second SCF cycle construct potential from input trial density for the Kohn-Sham equations. It gives eigenvectors and eigenvalues after one complete cycle. Latter valence and core charge densities are computed by integration over all valence and core states respectively. Then they are summed up to new electron charge density. It is then compared with the previous old charge density. If both are same then SCF cycle converges successfully. Otherwise same cycle is repeated with new electron density as input parameter until SCF cycle is converged. After the convergence of SCF cycle one can calculate the desired physical properties.

Results obtained with WIEN2k are considered to be most accurate, though they are most expensive in terms of computation. For bulk systems it behaves quiet well. However, for supercell, constructed for magnetic configuration, it becomes quiet time consuming. Therefore, for such problem's parallelization become important. In this method parallelization is done over k points and every k point is calculated on single CPU.

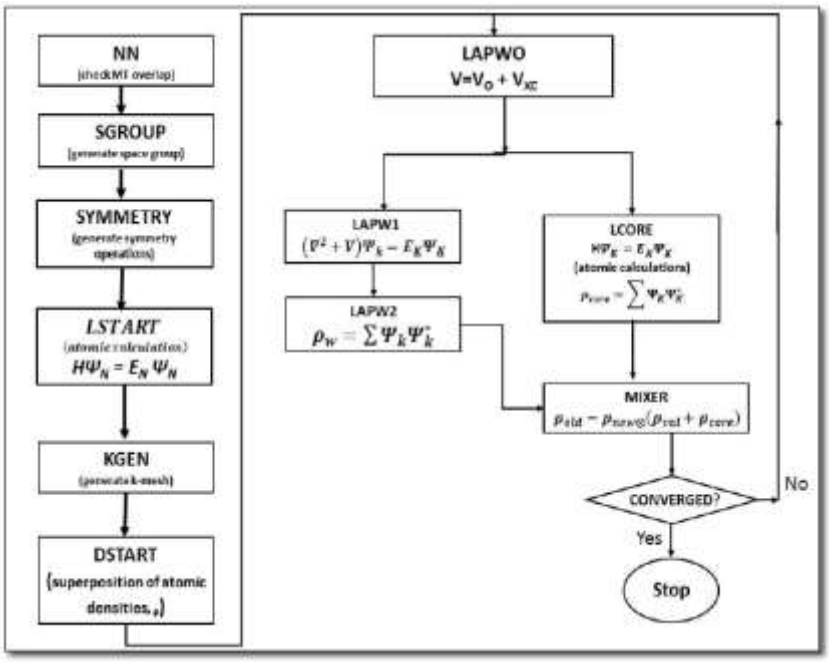

Figure 27. *Schematic flow chart for the WIEN2k code*[137]

In this way supercell can be calculated in a reasonable time span. In this thesis WIEN2k code is used to explore different functional magnetic materials. Supercell is also constructed in order to make antiferromagnetic configuration for $Bi_2Fe_4O_9$. Different xc functionals are used to compare structural, electronic, magnetic and optical properties of studied materials. WIEN2k has been used most successfully to obtain accurate results.

3. Monte Carlo simulation (SMC)

Improving the accuracy of Monte Carlo (MC) results has been a big help in several disciplines in addition to physics. In the broadest sense, the simulation of MC means any simulation (which is not necessary a computer simulation) which uses random numbers in the simulation algorithm.

MC methods, although was used for a very long time, and became increasingly important since their implementation by Von Neumann, Udilam and Metropole at the end of the Second World War, in order to study the diffusion processes (the simulation of nuclear reactions). These methods lend themselves well to the modeling of such a process insofar as it has a purely stochastic character.

The idea of using randomness to get an answer to a scientific problem is actually much older than computers. These methods give a very general numerical resolution framework, without theoretical constraints and a framework for evaluating the uncertainty linked to the results. That is why they are applied to a wide variety of problems.

The two main types of problems effectively dealt with by the MC method are the calculations of multiple integrals, and the problems of diffusion and collision. This is made possible by the essential property of being able to simulate distributions of random quantities.

The term "MC" is actually extremely broad, and there is a lot of overlap. The term "Monte Carlo" comes from famous casinos in Monte Carlo. When the study of MC methods got very serious in the 1940s and 1950s, someone thought of the similarity of using random numbers in casino games, and called the method thereafter.

To give a concrete example, the molecular dynamics (DM) simulations that describe atomic motion, is in principle completely deterministic in nature. But in practice, random numbers are often used in the MD as well. The initial atomic velocities are usually given randomly, so this brings character to MC.

"Anyone who considers arithmetic methods of producing random numbers is, of course, in a state of failure." John Von Neumann (1951). Therefore, the key element of any MC method is the good source of the state of the laws of chance, i.e. any MC simulation involves, by definition, random numbers. Perhaps begins with the experience of "the needle of Buffon" conducted in the 18th century by the famous naturalist and philosopher GL Buffon.

Many scientific and technological sectors have now adopted this type of approach known as the "Monte Carlo method". It is in fact the increased power of computers that has enabled these methods to become operational and to spread in sectors as varied as physics, such as molecular and genetic biology, telecommunications, networks, operational research, finance, and many more.

However, the calculated result depends in a complicated and coupled way on all the electron and photon transport physics.

In this case, the theory cannot provide a precise mathematical description and whole of microscopic and macroscopic physics. Theory can, however, provide intuition for the design of measures. Monte Carlo methods are an addition to this process as well, serving in experience analysis and verification or invalidating of the design.

3.1. MCS operations and basics

The main difficulty related to the study of condensed matter physics is due to the large number of particles that make up the systems. Let's start from the point where a system is at thermodynamic equilibrium. In this case, we can use statistical physics. The idea is then based on the knowledge of the partition function in a given statistical set, and from which the physical observables that we want to study can be averaged. Knowing this partition function requires summing up on all the microscopic states of the system. In theory, these states are solutions of Schrödinger's equation, but the number of states is so large that it is impossible to realize this sum. This problem may seem difficult, there is nevertheless a solution by conceding to certain approximations. Also, a number of theoretical methods have emerged in the study of condensed matter systems. We can cite the mean field method (CM), the renormalization group, Green's functions, transfer matrices, etc.

To tackle the problem from a digital point of view, we must answer two questions in particular:

First, how do we converge the system towards an out of balance but stationary regime? Secondly, once this stationary regime has been reached, how can we average the observables relevant to our study? These two questions will be the subject of the following part.

Statistical physics is based on the study of a system at equilibrium in a statistical whole. There are several sets, as far as we are concerned, we are interested in the study of our systems in the canonical set [N, V, T] in which a system is characterized by a number of particles N, a volume V , as well as a fixed temperature T. As we have already pointed out, the approximation of thermodynamic quantities is conditioned by the knowledge of the partition function Z:

$$Z = \sum_{i=1}^{N} e^{-\beta E_{im}} \qquad (36)$$

With $\beta=1/k_bT$, N is the number of states and k_b is the Boltzmann constant

The statistical weight of a particular state i or the probability that a state i exists or also the Boltzmann weight is:

$$P_i = \frac{e^{-\beta E_i}}{Z} \qquad (37)$$

The partition function can also be given in other forms:

- If we work with energy: $Z = \sum_E g(E)e^{-\beta E}$ (38)

- If we work with the Hamiltonian H: $Z = Tr\, e^{\beta H}$ (39)

It is in a way “the key function” of statistical physics, because from it we calculate the thermodynamic potential or the free energy, then these derivatives allow us to generate the other thermodynamic quantities, as shown in the following diagram:

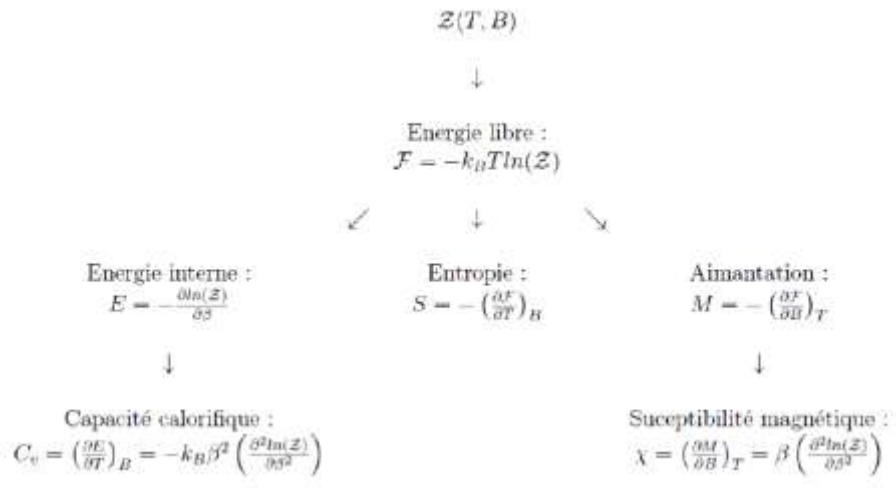

Figure 28. *Utilities of the partition function*

Unlike the theoretical study of statistical physics which uses derivatives, the Monte Carlo simulation exploits and simulates the random thermal fluctuation of the studied system from one state to another (the fluctuations of thermodynamic quantities are extremely important with regard to l 'interpretation of physics) but after having calculated the averages of the quantities we want.

Taking for example a quantity A, its mean value has the expression:

$$< A >= \sum_{i=1}^{N} A_i P_i = \sum_{i=1}^{N} \frac{A_i e^{\beta E_i}}{Z} \qquad (40)$$

Then if A is subjected to an excitation B, the fluctuation of A when it is subjected to B is: $\frac{\partial <A>}{\partial B}$

This is the response or the susceptibility from <A> to B. The fluctuation is none other than the standard deviation, so it is easy to establish the expression of the susceptibility of the quantity A:

$$< (A - < A >)^2 >=< A^2 > - < A >^2 \qquad (41)$$

$$< A >= \frac{1}{\beta} \frac{\partial \ln(Z)}{\partial B} = \frac{1}{\beta} \frac{Z'}{Z}\Big|_B \qquad (42)$$

$$< A >^2 = \frac{1}{\beta^2} \frac{Z''}{Z}\Big|_B \qquad (43)$$

$$< A^2 > - < A >^2 = \frac{1}{\beta^2} \left(\frac{Z''}{Z} - \frac{Z'^2}{Z^2} \right) = \frac{1}{\beta} \frac{\partial <A>}{\partial B} \qquad (44)$$

$$\frac{\partial <A>}{\partial B} = \beta (< A^2 > - < A >^2) \qquad (45)$$

During simulations, it will be essential to calculate quantities such as the internal energy of the system, the magnetization, the magnetic susceptibility and the heat capacity.

The process of Monte Carlo simulation to pass from one state to another (which is none other than the solution of the problems mentioned above and which consists in generating a stochastic dynamic between two successive configurations) is governed by the master equation:

$$\frac{dP_a}{dt} = \sum_b (P_b \pi(b \to a) - P_a \pi(a \to b)) \qquad (46)$$

With P_a, P_b: the probabilities of finding the system in state a or b (probability of realization of the state)

$\pi(b \to a)$ and $(a \to b)$: the probabilities of transition from the system from state a to state b or from state b to state a during time t (probability of state transition)

The probabilities π are chosen in such a way that at equilibrium we will have the Boltzmann weight as the solution to the main equation.

$$P_a = \frac{e^{-\beta E a}}{Z} \qquad (47)$$

It is now a question of presenting the basic elements of the simulation by Monte Carlo, through the three main ideas: "the important sampling", "the detailed balance" and the "acceptance rate". Mastering the meaning of these terms will give us more information on the Monte Carlo simulation at thermal equilibrium.

3.1.1 Large sampling

The idea is not like what we saw previously to calculate the average of a quantity <A> by visiting all the possible states of the system because it can take a lot of time in order to make sure that we will travel at least one period, during the time of the experiment, hence the problem of the length of the chain. For example, a liter of gas, contains 10^{22}molecules, $(10^{27})^{10^{22}}$are possible states which is a spectacularly large number, hence the importance of taking a matrix of fairly large dimension, otherwise we risk not going through all the states. We speak in this case of important sampling, but to estimate a value A_M from a reduced number of states: the most important or relevant states represented by the subset: M, M = {a_1, a_2, a_3, …, a_i, …, a_M}, therefore

$$A_M = \frac{\sum_{a_i} \frac{A_{a_i} e^{-\beta E a_i}}{P_{a_i}}}{\sum_{a_i} \frac{e^{-\beta E a_i}}{P_{a_i}}} \qquad (48)$$

With: $P_{a_i} = \frac{e^{-\beta E a_i}}{Z}$: the probability of achieving state a_i

And from this probability, we deduce the value $\frac{A_{a_i} e^{-\beta E a_i}}{P_{a_i}} = Z$ of and replace it in the expression of A_M:

$$A_M = \frac{\sum_{a_i} A_{a_i} Z}{\sum_{a_i} Z} = \frac{\sum_{a_i} A_{a_i}}{\sum_{a_i} 1} = \frac{1}{M} \sum_{a_i} A_{a_i} \qquad (49)$$

Note: If all the states are equiprobable (that is to say $\forall i,j\ P_{a_i} = P_{a_i}$), then we will have a bad choice.

3.1.2 Markov chain

At the outset, we cannot simply randomly select certain states and accept or reject them by taking them equally likely to $e^{-\beta E_x}$. The result will not be better than that resulting from a random sampling or there is a risk of virtually repeating certain states as many times. The algorithms of the Monte Carlo methods use the Markov process to choose the states used (considered).

The Markov process is the mechanism that generates a state b of the system from another known. The generated state is not always the same, it scans the system in search of new states with a transition probability $\pi(b \to a)$ on which it imposes two conditions:

- they do not change over time.

- they only depend on the properties of the system on states a and b.

This translates the fact that the probability of transition from one state a to another b $\pi(b \to a)$ of the Markov process is always constant and will have to satisfy the closure relation:

$$\sum_b \pi(b \to a) = 1 \qquad (50)$$

And this while not forgetting that the transition from a state to itself $(a \to a)$ is not prohibited. In other words, $\pi(a \to a)$ it is not always zero.

In the Monte Carlo simulation, we will repeatedly use the Markov process to generate the Markov chain of new states. It is generally used especially when we want to start from any state of the system and generate a series of configurations of certain precise (final) states for example. And to complete the Markov process, we will need to impose two new conditions: ergodicity and detailed balance.

3.1.3 Ergodicity

The condition of Ergodicity is the fact that it will be possible by the Markov process to reach any state of the system from another if we evolve during a sufficiently large time. This is necessary to reach our initial, that of generalizing states from a correct probability called Boltzmann. Each state "a" appears with a certain non-zero probability P_a in the Boltzmann distribution.[138] And if this state cannot be accessible from another state "a" this will not be a

problem, we will continue our process and, in this case, we will resume the diagram from this new state. And it will be necessary in this case to not create an algorithm which violates the condition of Ergodicity.

3.1.4 Detailed balance

This other condition of the Markov process is one of those which ensures that the probability of Boltzmann distribution that we will generate after our system has reached equilibrium is the greatest of all the other distributions. The real meaning of "system in equilibrium": the number of transitions which leave a state are equal to those which enter this state. This can be expressed mathematically by the following equation:

$$\sum_b P_a \pi(a \to b) = \sum_b P_b \pi(b \to a) \quad (51)$$

And by introducing the closure equation, we will have:

$$P_a = \sum_a P_b \pi(b \to a) \qquad (52)$$

If this equation is satisfied, the probability P_a will be at equilibrium in the dynamic Markov process. But it may happen that the satisfaction of this equation is not totally efficient to guarantee that the probability of distribution can reach P_a any state of the system if we keep the system running for a long time.

Indeed, the probability of transition $\pi(a \to b)$ can be determined as an element of the Markov matrix. If we measure the time taken in each state during the Markov chain, then the probability at a time t+1 next (where the system will be in state "a") will be:

$$P_b(t+1) = \sum_a \pi(a \to b) P_a(t) \qquad (53)$$

In matric writing:

$$P(t+1) = \Pi\, P(t) \quad (54)$$

Where P(t) is the vector whose coordinates are the different statistical weights $P_a(t)$.

To keep the ergodicity of the system, we stretch time infinitely so that the Markov process reaches equilibrium, which is physically expressed by a fixed point, via the following equation:

$$P(\infty) = \Pi\, P(\infty) \qquad (55)$$

If the equilibrium is reached by the process is a limit cycle of size n, the equation becomes:

$$P(\infty) = \Pi^n\, P(\infty) \quad (56)$$

From the above we can say that we are informed that there is no guarantee that the state of equilibrium generated will have the expected probability of distribution.

To remedy this problem, we therefore apply another condition to our transition probability: the specific or detailed balance condition stated as follows:

$$P_a \pi(a \to b) = P_b \pi(b \to a) \qquad (57)$$

It is therefore clear that each state which satisfies this condition will absolutely satisfy equation (51) which is only a summation of on the different states concerned. By noting the equivalent bidirectional form of (57), we can see that the specific balance condition eliminates the notion of cycle which included the limit n. Indeed, the detailed balance informs us that on average, the system can leave from one state "a" to another "b" regardless of the path chosen and after an infinite time, we will have a probability of distribution P(t) tending exponentially like the eigenvectors corresponding to the strong eigenvalues of Π.

At equilibrium, we want the distribution to be that of Boltzmann, so the condition of the detailed balance allows us to write:

$$\frac{\pi(a \to b)}{\pi(b \to a)} = \frac{P_b}{P_a} = e^{-\beta(E_b - E_a)} \qquad (58)$$

In addition to this equation, if we add equation (53) we will obtain the constraints of the choice of the transition probability $\pi(a \to b)$.

If we choose as an example the probability of transition $\pi(a \to b)$ proportional to $e^{-\frac{\beta}{2}(E_b - E_a)}$, we will have a bad choice. The choice is to choose for example the Metropolis algorithm.

3.1.5 Acceptance rate:

From all that we have mentioned so far as an important element for the rapid and efficient obtaining of a steady state system, we have been able to generate a Markov process with which we have been able to find new states with a probability. However, it is difficult for us to predict the appropriate Markov process if we find ourselves in a given state, at its good probability, and seek the next state. Although it is still possible to use the conditions given, we could thus suggest several processes but until then without being able to have the right probability of triggering, that is to say that allowing us to transit to a next state while respecting the equations (52) and (58).

In reality, there are unintended consequences when we allow ourselves the choice of any algorithm to generate new states and therefore it is necessary to have a desired transition probability by introducing a condition d acceptance of the transition rate.

By posing a=b, $\pi(a \to b)$ is not zero. This would like to emphasize that the detailed balance condition is always verified for $\pi(a \to b)$ whatever the value of this probability. In other words, these conditions give us enough freedom on the possibilities of making transitions on each site with the probabilities that we wish. To see this, let's break the transition report down into two parts:

$$\pi(a \to b) = g(a \to b)\, A(a \to b) \quad (59)$$

g(a→b): Selective probability (choice of the target state "a" to generate the state "b")

A(a→b): Change acceptance report (if we accept state b generated from state a, we change the state of the system to b)

A(a→b) Є [0,1]. We are also free to choose its value. Choosing A(a→b) = 0 is equivalent to saying with certainty π(a→b) = 1 which is not, however, a case that we will look for. It is therefore to be avoided from the above, that we also have total freedom on the choice of g(a→b) from the constraint (58) which fixes the relationship:

$$\frac{\pi(a \to b)}{\pi(b \to a)} = \frac{g(a \to b)A(a \to b)}{g(b \to a)A(b \to a)} \quad (60)$$

Note that $0 < \frac{\pi(a \to b)}{\pi(b \to a)} < \infty$ therefore g(a→b) and g(b→a) can take any desired value.

Our additional constraint given by the closure relation (51) will also be satisfied since the sum will limit to the state of the Markov chain where we started the summation. Thus, in order to create our Monte Carlo algorithm, we will create an algorithm which will generate successive states simply with the data of g(a→b) and we will then select the states which are useful to us by the acceptance condition A(a→b) which we will choose as it will satisfy equation (60). This will have to satisfy all the queries of the transition probabilities such that when the algorithm reaches equilibrium, we will draw the true Boltzmann probability.

All this seems pleasant, but it will be necessary to take into account that if the acceptance rate is low, our algorithm will appear motionless, which will naturally block the evolution of the system. It is therefore necessary to find an algorithm which will evolve between the states for a large sampling. It is imperative to take care to shorten the processing time of our matrix. So,

we need to look for an algorithm that will respect a suitable time compared to the sampling available. It suffices to observe that equation (60) fixes only the acceptance rate $\frac{A(a\to b)}{A(b\to a)}$ between two distinct states in any direction with the constraint that this rate is between 0 and 1.

The correct algorithm is the one that keeps the acceptance ratio (i.e. choose A(a→b) close to 1 and adjust the value of g(a→b)).

3.2 Metropolis algorithm and Ising Model

The choice of the stationary Markovian process to satisfy the set of equations, (57) is one of the solutions. We will see later other methods. In order to obtain solutions of equations (57) or, in other words to obtain the transition matrix (π(a→b)), note that the elementary stochastic process in a Monte Carlo algorithm is the succession of two stages:

1. From a configuration a, we randomly draw a configuration b, with a probability g(a→b).

2. This new configuration is accepted with probability A(a→b). Thus, we got equation (59).

In the original Metropolis algorithm (and in most Monte Carlo algorithms),[139] we choose g(a→b) = g(b→a). In this case, equation (58) becomes:

$$\frac{\pi(a\to b)}{\pi(b\to a)} = \frac{A(a\to b)}{A(b\to a)} = e^{-\beta(E_b - E_a)} \qquad (61)$$

The solution chosen by Metropolis et al. is:

$$A(a \to b) = \begin{cases} e^{-\beta(E_b - E_a)} & si\ E_b > E_a \\ 1 & si\ E_b < E_a \end{cases} \qquad (62)$$

This amounts to saying that if $\Delta E = E_b\text{-}E_a$, the transition will be accepted, otherwise the transition is accepted with probability A(a→b), that is to say we generate a random number (random number) $\xi \in [0,1]$, and compare it to A(a→b): if $\xi < e^{-\beta(E_b - E_a)}$, the new configuration is accepted, otherwise it will be refused and we keep the old one. This procedure is shown in the following figure:

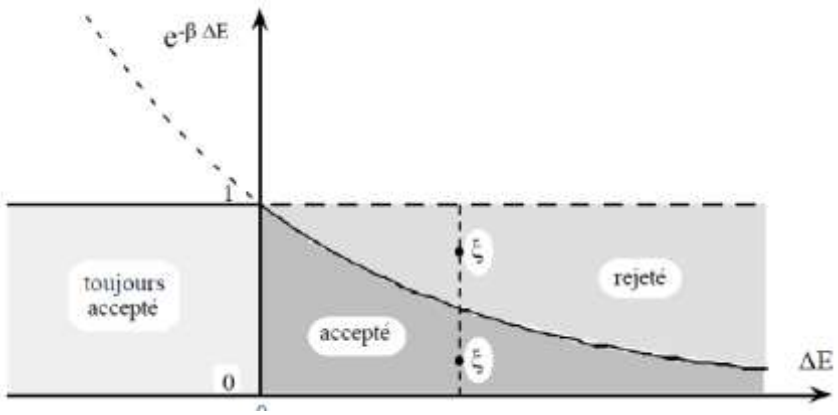

Figure 29. *Boltzmann weight as a function of the energy difference presenting the accepted and rejected states*

The Metropolis algorithm is very general, and it can be applied to any model where one can generate random numbers and associate variations of energies with them. Numerically, our approach consists in building a crystal structure on which we apply a spin model (Ising, Heisenberg, XY). Let's take the simplest of them, the Ising model.[140] It is a network model with two spin states S=±1/2 (or also S=±1) widely used in statistical physics to describe anisotropic systems where there is a strong crystal field which forces all the moments to take a direction called direction of easy magnetization.

With the Ising model, we assume that the crystal lattice sites are occupied by magnetic dipoles which can only take two values on the z axis (1/2 or -1/2). Each spin interacts with its neighbors through an exchange interaction or interaction coupling. Coupling J is a monotonic function, decreasing and dependent on the distance between neighboring spin. To simplify, the range of interactions is limited to the first neighbors. Finally, the sign determines the type of magnetism of the network. If J>0, the energy of the network is minimal in ferromagnetic configuration. Conversely, if J<0, the network will adopt an antiferromagnetic ground state.

The zero field Hamiltonian (B=0) is defined by:

$$H = J \sum_{<i,j>} S_i S_j - B \sum_i S_i \quad (63)$$

In one dimension, this model has an analytical solution and we show that the critical temperature is zero temperature.

In two dimensions, Onsager (1944) solved the model in zero external field H and showed that there is a phase transition at finite temperature. For the square network, this critical temperature is worth:

$$T_c = J\frac{2}{\ln(1+\sqrt{2})} \qquad (64)$$

which gives T_c=2.269J.

At three dimensions, the model was not solved analytically, but the numerical simulations on this model were numerous and the numerical estimates of the critical temperature are very precise.

The calculation of thermodynamic quantities (average energy, magnetization, specific heat, susceptibility, ...) can be done simply.

From the expression of the Hamiltonian, we calculate ΔE:

$$\Delta E = E_b - E_a = -J\sum_{<i,j>} S_i^b S_j^b + J\sum_{<i,j>} S_i^a S_j^a \quad (65)$$

E_a: Initial energy

E_b: energy of the new configuration (flip)

We arbitrarily choose the spin k modified on the network, so the expression (28) becomes:

$$\Delta E = -J\sum_{ivk} S_i^b S_k^b + J\sum_{ivk} S_i^a S_k^a \qquad (66)$$

$$\Delta E = -J\sum_{ivk} S_i^a (S_k^b - S_k^a) \qquad (67)$$

- If $S_k^a = +1$, then $S_k^b = -1$, therefore $S_k^b - S_k^a = -2$
- If $S_k^a = -1$, then $S_k^b = +1$, therefore $S_k^b - S_k^a = +2$

Hence,

$$\Delta E = 2J\sum_{ivk} S_i^a S_k^a \qquad (68)$$

- If $\Delta E \leq 0$, the flip is accepted ($S_k^a - S_k^b = -S_k^a$)
- If $\Delta E \geq 0$, the flip is accepted with a probability mentioned above, otherwise the initial configuration is kept.

Specific heat

Like what we saw in equations (41) to (45), we calculate the specific heat in the same way and we obtain the following equality:

$$Cv = \frac{\beta^2}{N}(< E^2 > - < E >^2) \qquad (69)$$

Magnetization

The total magnetization of the system for the initial configuration is the sum of the magnetizations of each spin:

$$M_a = \sum_i S_i^a \qquad (70)$$

Therefore,

$$\Delta M = M_b - M_a = \sum_i S_i^b - \sum_i S_i^a = S_b^b - S_i^a = 2S_i^b = -2S_i^b \quad (71)$$

Thus,

$$M_b = M_a + \Delta M = M_a + 2S_i^b = M_a - 2S_i^b \qquad (72)$$

Susceptibility

In the same way as the specific heat, we find that the susceptibility is equal to:

$\chi = \frac{\beta}{N} = (< M^2 > - < M >^2)$ (II.36) Where $\beta = \frac{1}{k_B T}$, and k_B is the Boltzmann constant which will be fixed at $k_B = 1$.

The magnetic entropy

$$\Delta S_m = \int_{h_i}^{h_f} \left(\frac{\partial M}{\partial T}\right) dh \qquad (73)$$

Where $\left(\frac{\partial M}{\partial T}\right)$ is the thermal magnetization for a fixed magnetic field H_i.

The adiabatic temperature change

$$\Delta T_{ad} = T \frac{\Delta S_m}{C_m} \qquad (II.38)$$

4. Synthesis methods of Magnetic Nanostructures

Nanomaterials are foundations of nanoscience and nanotechnology. The development of nanomaterial has been attracted great interest in the worldwide in the past few years.

Nanorods and nanoporous structures are considered as nanoparticles with diameter smaller than the length and ranges between 1-100 nm in diameter and 100 nm to tens of microns in its length. The fabrication of nanorods and nanoporous structures can be achieved from a wide range of materials which includes inorganic, electrical conductors, organic, insulators, and semiconductors[141,142]. Like other types of inorganic materials, magnetic nanorods and nanoporous structures should be produced with controlled properties based on manipulation of

processing parameters. Also, control of the processing conditions is needed to manipulate the structural characteristics of the particles allowing control of the intrinsic magnetic properties.
In this thesis, we aim at fabricating two types of $CoFe_2O_4$ nanostructures: The first one consists at synthesizing Co_2FeO_4 nanorods, grown by using electrochemical deposition inside the pores of anodic aluminum oxide (AAO). The second type of nanostructure is a new form of $CoFe_2O_4$ consisting of self-ordered $CoFe_2O_4$ nanoporous oxide layers via electrochemical anodization of FeCoV alloy metal sheet. Following that, we will discuss the synthesis methods which were used in this thesis, which are: electrochemical deposition and electrochemical anodization for synthesizing Co_2FeO_4 nanorods and $CoFe_2O_4$ nanoporous oxide layer respectively.

4.1. Electrochemical deposition method.

Electrodeposition is an electrochemical process applied for surface structure modification. The electrodeposition process is an old method in surface engineering processes which has a long history. The electrodeposition technique was firstly applied more than 2000 years ago in several hypothesizes [143,144]. The production of a galvanic cell with Volta in about 1800 and then progress in electrical motors from 1800 to 1900 led to use electrodeposition technique as a cost-effective process to produce a coating. In this process, a monolayer or multilayer coating is formed because of the electrochemical reactions occurred at the electrode/electrolyte interface and deposition of ions from the electroplating bath on the surface [145]. The coating may be deposited on the surface to enhance the solderability, lubricant properties, electrical conductance, corrosion resistance, and wear and thermal resistance of the substrate material. Electrodeposition process can be performed with both types of direct (DC) and pulse current (PC)[146]. In the DC method current is continuously applied to the system. However, in a PC electrodeposition process, the electrical current is alternated swiftly between two different values [147]. The properties of deposited coatings can vary because of pulsating parameters in PC electrodeposition process. The progress in electronics made it possible to control the properties of the coating by using the PC instead of DC method. More details will be discussed on the electrodeposition methods for fabricating CoFe2O4 nanorods in chapter 4.

4.2. Electrochemical anodization method.

Anodization is an electrochemical oxidation method to increase the thickness of metal (e.g. Al, Ti, Fe, W, Zr, Nb, etc) or semiconductor (e.g. Si, GaAs, etc) surface oxide layer[148]. As shown in figure 1, anodization technique was first presented in the preparation of alumina. In general, anodic oxidation of aluminum can produce two different types of oxide depending on the property of the electrolyte used. That is, normally, neutral electrolyte produces tight and non-

porous barrier oxides while porous oxides can be produced in an acidic electrolyte [149]. In the past decade, porous metal oxide layers made by anodization in an acidic electrolyte endows periodically ordered aligned 1D semiconductors with well-defined architecture, tunable thickness, and good corrosion resistance. Consequently, currently, preparation of porous materials via electrochemical anodization approach has still been attracting enormous attention, especially in fabricating highly ordered nanoporous materials. In 1991, Zwilling and co-workers[150] firstly reported the anodic oxidation of titanium (Ti) in fluorinated electrolyte under ambient conditions, by which spatially highly ordered titanium dioxide (TiO2) film with porous surface was fabricated. Since then, articles concerning 1D semiconductor materials are emerging in an endless stream.

Inspired by the fabrication of well-defined periodically ordered Al2O3 and TiO2 nanotube arrays, anodic oxidation techniques were further extended to prepare a large variety of other1D semiconductor arrays. For instance, transition metal foils including Fe [151], Ni [152], Cu[153], Zn[154], Zr[155], Nb [156], Hf [157], Ta [158], W[159], etc have been utilized as the metal precursors to prepare corresponding anodized metal oxides such as Fe2O3, NiO, Cu2O, and ZnO nanotube arrays. Moreover, some hybrid metal nanotube arrays can also be fabricated by using the metal alloy foils, e.g. TiAl[160], TiNb[161], or Ti6Al4V[162], most of which are featured by highly ordered nanostructures.

4.2.1. Anodization mechanism

Figure. 30 exhibits the typical anodization device for fabricating self-aligned highly ordered 1D semiconductor nanoporous oxide layer and nanotube arrays. Specifically, metal foil is directly connected to the positive electrode of DC power source as working electrode and conducting mediums such as platinum, graphite or metal is used as counter electrode. In this way, a thin metal oxides layer can be produced by a simple electrochemical oxidation of metal foil under ambient conditions. Generally, electrochemical anodization mechanism dictating the formation of self-aligned metal oxide arrays can be mainly divided into five stages including: (1) metal electropolishing, (2) formation of compact anodic metal oxides, (3) generation of self-ordered metal oxides (nanotubes or nanopores),(4) production of disordered oxide nanotubes, (5) organization of ordered nanoporous layers[163].

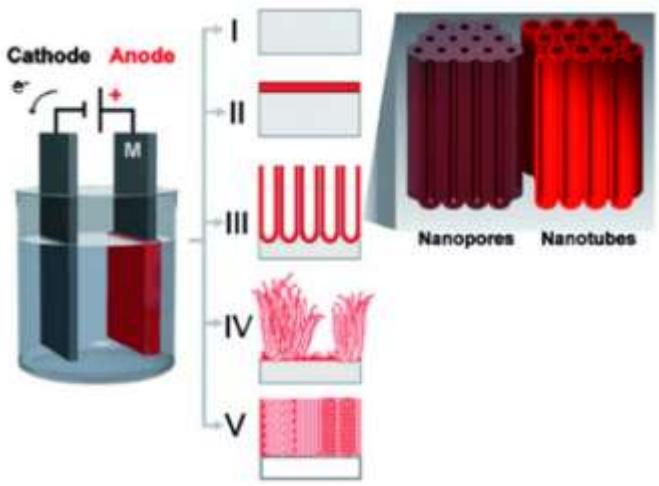

Figure 30. *Schematic illustration of electrochemical anodization process*

By taking TNTAs as a quintessential example, electrochemical anodization process can be generally divided into four steps: (1) At the beginning of anodization, metal Ti^{4+} interacts with O^{2-} or OH^- in the electrolyte to form an initial oxide layer on the surface under an electric field, during which these anions continuously migrate through the oxide layer to the metal/oxide interface and react with the metal at the interface[164]. (2) Subsequently, Ti^{4+} anions rapidly migrate from the metal/oxide interface to the oxide/electrolyte interface under an applied external electric field. (3) Afterwards, Ti–O bonds are weakened under the auxiliary electric field to promote the dissolution of the metal ions at the oxide/electrolyte interface, thereby causing dissolution of Ti^{4+} to the electrolyte solution and promoting reaction with the free O^{2-}.[165] (4) Finally, when chemical dissolution rate of metal oxide is in equilibrium with the anodization rate, thickness of the oxide film no longer increases. It should be emphasized that interaction between surface Ti^{4+} ions and O^{2-} in the electrolyte solution dictates the formation of initial oxide layer at the beginning of anodization[166], which can be expressed as follows:

$$2H_2O \rightarrow O_2 + 4e + 4H^+$$

$$Ti + O_2 \rightarrow TiO_2$$

Besides, noteworthy, field-assisted dissolution dominates the chemical dissolution in the initial stage of anodization due to relatively large electric field on the thin oxide layer[167]. Local dissolution of the oxide yields small dimples on the surface and they serve as the center of the hole, after which these pits become larger and are evenly distributed on the metal surface. The local chemical dissolution equation of the oxide can be expressed as follows:

$$TiO_2 + 6F^-{}_2 + 4H^+ \rightarrow TiF_6^{2-} + 2H_2O$$

On the other hand, it is worth mentioning that the presence of F^- ions in the chemical dissolution of metal oxides under acidic electrolytes plays a crucial role in forming nanotube rather than nanopores structures.[168]

5. Characterization methods used:

5.1. Measurement and Characterization Techniques

The cobalt ferrite $CoFe_2O_4$ nanorods and nanopores structures were characterized using various techniques for their structural and physical properties. Surface morphology was investigated using Scanning Electron Microscopy (SEM) equipped with an Energy Dispersive X-ray Spectrometer (EDX) to perform elemental analysis. Crystal structure was characterized using an X-ray diffraction in Grazing Incidence X-ray configuration (GI-XRD), an *in-situ* X-ray diffraction (*in situ* XRD). Room temperature magnetic properties were investigated using a Vibrating Sample Magnetometer (VSM).

5.1.1. Scanning Electron Microscopy Technique

The Scanning Electron Microscope (SEM) is a device for observation of specimen surfaces. Generally, when the specimen is irradiated with a fine electron beam, secondary electrons are emitted from the specimen surface. Topography of the surface can be observed by scanning of the electron beam over the surface and acquisition of the image detecting secondary electrons. The SEM requires an electron optical system to produce an electron probe, a specimen stage to place the specimen, a secondary-electron detector to collect secondary electrons, an image display unit, and an operation system. Figure 31.a shows a basic construction of the SEM, where the electron optical system consists of an electron gun, a condenser lens and an objective lens to produce an electron beam, a scanning coil to scan the electron probe, and other components. The electron optical system (inside the microscope column) and a space surrounding the specimen are kept at vacuum.

Three types of electron guns are generally used, the most common is a thermionic emission gun, and other electron guns are the field-emission electron and the Schottky-emission electron gun.

The secondary electron (SE) gun utilizes the Schottky-emission effect that takes place when a high electric field is applied to a heated metal surface. An advantage of the SE gun is that the electron-beam current is highly stable because the emitter, which is placed in an ultrahigh vacuum of about 10-7 Pa, is kept at a high temperature and no-gas absorption occurs.

The SEM generally uses a magnetic lens. When you pass a direct electron current through a coil-wound electric wire, a magnetic field is formed, and a lens action is produced on an electron

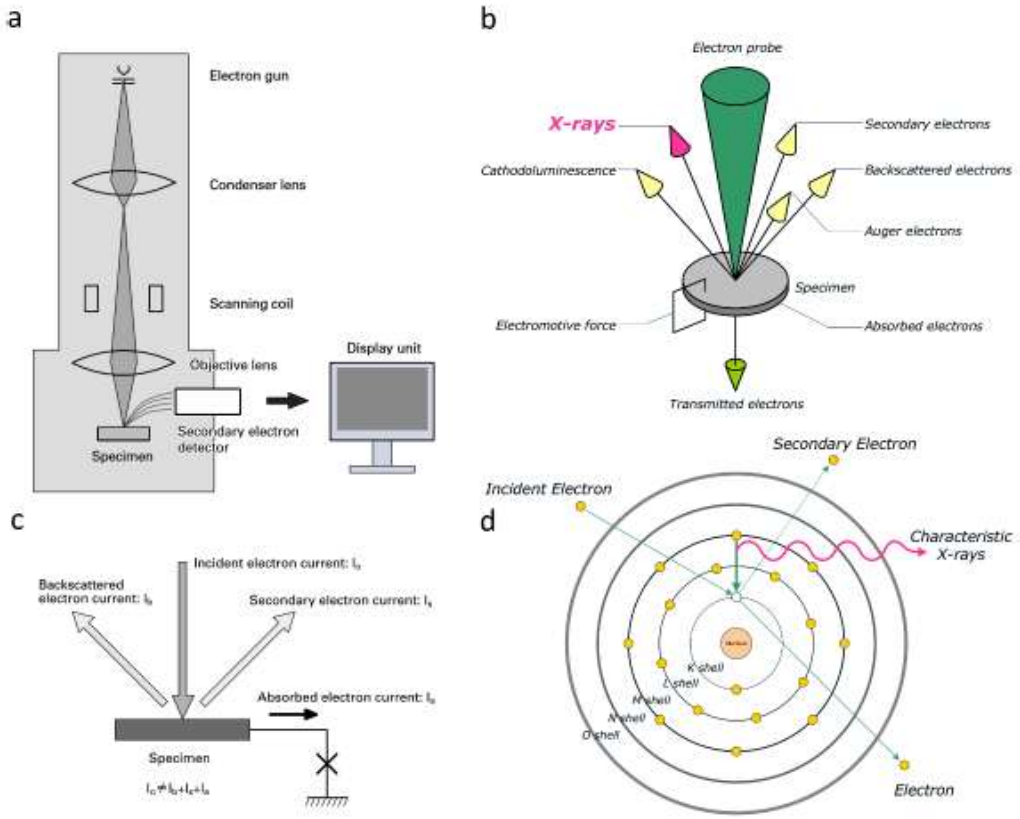

Figure 31. *(a)Basic construction of a SEM, (b)emission of various electron and electromagnetic waves from the specimen, (c)electric flow in a nonconductive specimen, (d)principle of the generation of characteristic X-rays.*

beam. The main feature of the magnetic lens is that when you change the current passing through the coil, the strength of the lens is also changed. Placing a lens below the electron gun allows you to adjust the diameter of the electron beam. The electron beam from the electron gun is focused by the two-stage lenses, which combines the condenser and objective lenses, and a small electron beam is produced.

The secondary electron detector is used for detecting the secondary electrons emitted from the specimen. The detector is incorporated either in the specimen chamber, or if the SEM is equipped with a strongly excited objective lens for higher resolution a secondary electron detector is placed above the objective lens and the secondary electrons are detected by utilizing the lens magnetic fields.

Figure 31b shows a schematic diagram illustrating various signals emitted from the specimen when the incident electron beam enters the specimen. The SEM uses these signals to observe the specimen surface (or just beneath the surface). When the incident electron beam enters the specimen, secondary electrons are produced from the emission of the valence electrons of the constituent atoms in the specimen. Since the energy of secondary electrons is very small, only those

generated at the top surface of the specimen are emitted outside of the specimen. Backscattering electrons are those scattered backwards and emitted out of the specimen, when the incident electrons are scattered in the specimen. Since backscattered electrons have higher energy than secondary electrons, a relatively deep region can be analyzed by the backscattering electrons.
The electrons that entered the specimen lose their energy and they are absorbed in the specimen. If a specimen is conductive, the electrons travels through the specimen stage, but if a specimen is insulating, the electrons stop in the specimen and the charging occurs. Figure 31c shows the schematic illustration of the charging. If some reason causes the number of the electrons exiting from the specimen to be larger than that flowing to the specimen, the specimen is positively charged. The most typical method to prevent the charging is conductive coating of an insulating specimen with a highly-conductive thin metal layers with a thickness ranging from a few to 10 nm (e.g., Au, Pt, Au-Pd, Pt-Pd).

5.1.2 Energy Dispersive X-ray Spectrometer Characterization

When the incident electrons enter a specimen, various electrons and electromagnetic waves are emitted from the specimen surface (Figure 31b). Figure 31d shows the schematic diagram of the generation of characteristic X-rays. When electrons in the inner shells are emitted from the constituent atoms in the specimen due to the irradiation of the incident electrons, the vacant orbits are filled with outer-shell electrons, and the substance emits X-rays whose energies correspond to the energy difference between the outer-shell electrons and the inner-shell electrons. These X-rays are used for elemental analysis. The X-rays that are emitted by the excitation of atoms and emission of the electrons in K shells are called “K lines”, whereas those emitted by the L and M shells are called “L lines” and “M lines”, respectively. As the constituent element is heavier, the X-rays energy is higher, therefore high-energy incident electrons are required to excite X-ray from heavy elements.
The EDX is used to analyse X-ray spectra by measuring the energies of the X-rays. The advantage of the EDX is that the X-rays from a wide range of elements are analyzed simultaneously. X-ray spectra enable us to perform quantitative analysis that identifies what elements are present in a specimen area irradiated by an electron beam. Three analysis modes are available: Point analysis to obtain a spectrum from a point irradiated with an electron beam, Line analysis to display one-dimensional distribution of elements on a specified line, and Mapping to display two-dimensional distributions of elements in a specified area. Since the intensity of X-rays is proportional to the concentration of the corresponding element,

quantitative analysis can be performed. If you try to analyse an insulating specimen without highly-conductive coating, this specimen is analyzed with a low accelerating voltage caused by the charging effect, thus, X-rays with high excitation energies cannot be detected, and the accuracy of quantitative analysis is degraded.

5.1.3 X-ray Diffractometer Crystal Structure Analysis

X-ray diffraction (XRD) is a technique used to measure the atomic arrangement of specimens. When a monochromatic X-ray beam hits a specimen, in addition to absorption and other phenomena, we observe X-ray scattering with the same wavelength as the incident beam, called coherent X-ray scattering. The coherent scattering of X-rays from a specimen is not evenly distributed in space but is a function of the electron distribution in the specimen. The atomic arrangement in specimens can be ordered like a single crystal or disordered like glass or liquid. As such, the intensity and spatial distributions of the scattered X-rays form a specific diffraction pattern which is the "fingerprint" of the specimen.

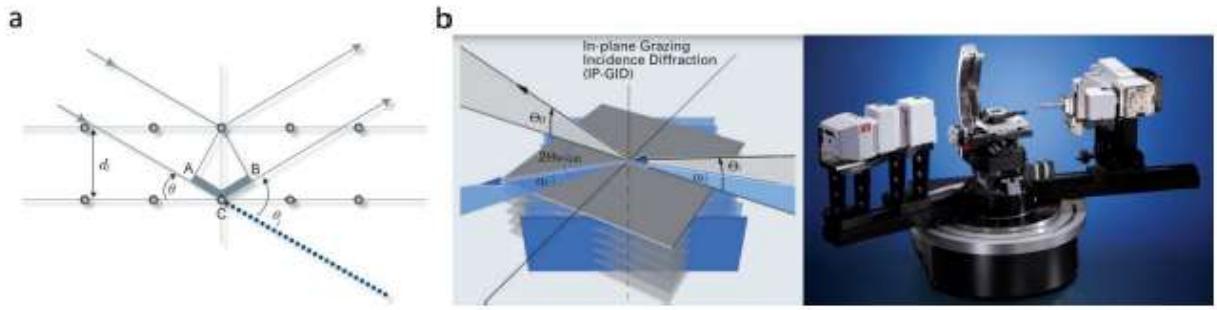

Figure 32. *(a) The incident X-Rays and reflected X-rays make an angle of ϑi symmetric to the normal of the crystal plane. (b) Principle of Grazing incidence X-Ray diffraction and its illustration*

There are many theories and equations about the relationship between the diffraction pattern and the material structure. Bragg's law is a simple way to describe the diffraction of X-rays by a crystal. In Figure 32a, the incident X-rays hit the crystal planes in an angle Θ, and the reflection angle is also Θ. The diffraction pattern is a delta function when the Bragg condition is satisfied:

$$n\lambda = 2d_i \times sin\theta_i$$

Where the wavelength λ is defined by the X-ray tube used, peak positions 2Θi are defined by the lattice spacing di, and peak intensities are defined by the geometrical and elemental structure of the lattice.

For real specimens, the diffraction patterns are different from the theoretical delta functions with discrete relationships between points to continuous distributions with spherical symmetry.

The diffraction beams from a single crystal point to discrete directions each corresponding to a family of diffraction planes. The diffraction pattern from a polycrystalline specimen forms a series of diffraction cones if a large number of crystals oriented randomly in the space are covered by the incident X-ray beam. Each diffraction cone corresponds to the diffraction from the same family of crystalline planes in all constituent grains. Polycrystalline materials consist of many crystalline domains, numbering from two to more than a million in the incident beam. In single-phase polycrystalline materials, all of these domains have the same crystal structure with multiple orientations. Polycrystalline materials could also be multiphase materials with more than one kind of crystal blended together. Polycrystalline materials can also be bonded to different materials such as thin films on single crystal substrates. The crystalline domains could be embedded in an amorphous matrix or stressed from a forming operation. Usually, the sample undergoing X-ray analysis has a combination of these effects. Polycrystalline diffraction deals with this range of scattering to determine the constituent phases in a material or the effect of processing conditions on the crystallite structure and distribution. In this work, a standard powder diffractometer PANalytical X'Pert Pro with Cu radiation was used.

Nonambient temperature measurements of the ME core-shell nanocables were conducted by the *in-situ* X-ray diffraction using a powder diffractometer PANalytical X'Pert Pro Anton Paar HTK1200 (1200 °C) with Co anticathode.

Grazing Incidence X-ray Diffraction Technique

Modern thin-film technology deals with increasingly thinner and more complex layered structures. The analysis of such challenging samples pushes classic diffraction methods to their limits. The Bruker D8 Discover has a winning combination of powerful X-ray sources, dedicated optics, the most sensitive 1- and 2-dimensional detectors, and a tilt stage to assure that no reflections are lost (Figure 32b). It directly evaluates the in-plane lattice parameters (perpendicular to the sample surface), determines the in-plane crystallite size and measures the in-plane texture and the domain structure. As an added feature, these parameters can be determined as a function of depth.

The crystal structure of the vertically aligned nanopillar arrays and (1-3) ME nanopillar based nanocomposites was characterized using the Bruker D8 Discover diffractometer in grazing incidence X-Ray diffraction configuration (GI-XRD), operating with CuKα radiation (CuKα1 = 1.5406 Å, CuKα2 = 1.5443 Å) and with an incident beam angle of 2°.

5.1.4. Vibrating Sample Magnetometer: for magnetic measurement.

The basic operating principle of vibrating sample magnetometer (VSM) is based on Faraday's Law of Induction (i.e. changing magnetic flux will produce an electric field). The generated electric field can be measured and can tell us information about the changing magnetic field. A VSM is employed to measure the magnetic behavior of magnetic materials. A VSM operates by first placing the sample to be studied in a constant magnetic field. If the sample is magnetic, the external magnetic field will magnetize the sample by aligning the individual magnetic spins or the magnetic domains, with the applied field. The stronger the external magnetic field, the larger the magnetization will be in the material. The magnetic field around the sample will generate due to magnetic dipole moment of the sample, sometimes called the magnetic stray field. As the sample is vibrated (i.e. moved up and down), the magnetic stray field will be changed as a function of time and a set of pick-up coils will sense the same. According to Faraday's Law of induction the alternating magnetic field will cause an electric field in the pick-up coils. This current is directly proportional to the magnetization of the sample. The induction current is amplified by a transimpedance amplifier and lock-in amplifier. The assorted components are connected to computer interface. By means of controlling and monitoring software, the system can show the data on how much the sample is magnetized and how its magnetization depends on the strength of the constant magnetic field.

Figure 33. *Schematic of VSM magnetometer*

Chapter III. Structural, electronic, magnetic, and Magnetocaloric Properties in antiperovskite materials of type Mn_3AC (A=Ga, Al)

1. Introduction

Recently, significant progress was made in pushing magnetic refrigeration towards commercialization as a potential alternative to other conventional vapor-cycle cooling due to its higher energy efficiency and the absence of harmful active materials, making it relatively more environmentally friendly. New magnetocaloric materials and devices have been developed and are becoming more powerful and efficient. [169,170,171,172] Although, several achievements were reached, the extensive study revealed a number of flaws and challenges in the deployment of magnetic refrigerants.[173] This new technology is based on the magnetocaloric effect (MCE) which is related to magnetic entropy change (ΔS_m) in a magnetic material under an applied magnetic field.[174] A good magnetic refrigerant should have a large MCE and also high relative cooling power (RCP), meaning a large magnetic entropy change (ΔS_m) and adiabatic temperature change (ΔT_{ad}), respectively.[175] Rare earth-based alloys (Gd in particular) were the first magnetic refrigerants to be used in the application of magnetic refrigeration at room temperature.[176,177] However, their poor resistance to oxidation and corrosion limited their use. There has been a lot of research focused on finding new materials with excellent magnetocaloric properties.[178,179] The first studies were focused on materials undergoing a first-order magnetic phase transition and demonstrate a substantial MCE, such as Gd based amorphous alloys, $Gd_5Si_2Ge_2$,[37,180,181,182] $La(Fe,Si)_{13}$,[42,183] $MnAs_{1-x}Sb_x$, $MnFeP_{1-x}As_x$, Ni-Mn-In. However, their phase transition is accompanied by a discontinuous volume deformation,[184] and some thermal hysteresis for some compounds; making magnetic refrigeration less efficient. Today, there is growing interest in investigating the MCE of materials which exhibit a second-order magnetic phase transition, such as Mn-based anti-perovskite compounds Mn_3AX (A=Ga, Al, Sn, In, Zn, etc.; X=C, N); mainly due to their large magnetoresistance (MR). The main drive behind this study is to calculate the structural, electronic, magnetic, and magnetocaloric properties of the second-order ferromagnetic to paramagnetic transition in the antiperovskite materials type Mn_3AC (A=Ga, Al.) i.e.; Mn_3GaC and Mn_3AlC compounds.

It is of interest to mention that the metallic antiperovskite Mn_3GaC compound is characterized by two magnetic transitions, namely: (i) a first-order transition from antiferromagnetic (AF) to

ferromagnetic (FM) state with the transition temperature about T_i ~ 160K,[185] however this transition is accompanied by a discontinuous expansion of the lattice parameter *a* with decreasing temperature, and (ii): a second-order transition from ferromagnetic (FM) to the paramagnetic (PM) state at Curie temperature T_C =249 K.[123] It was found that the Mn_3GaC compound have a giant magnetocaloric effect in the first-order transition under applying a magnetic field of 2.0T,[186] the maximum values of the magnetic entropy change (ΔS_m^{max}) and the adiabatic temperature change(ΔT_{ad}) are found to be 15 J/kg.K and 5.4 K, respectively.[124] On the other hand Mn_3AlC exhibits a ferromagnetic to paramagnetic phase transition around Curie temperature T_c=287K,[81] i.e. near room temperature. B.S Wang et Al.[81] conducted a study in which they resorted to magnetoelastic and magnetoelectronic couplings in Mn_3AlC. However, their theoretical results were too incompatible with experimental data, which is what motivated us to explore another approach. The present work focuses on the study of structural, electronic, magnetic, magnetocaloric and transport-related properties of the Mn_3GaC and Mn_3AlC compounds. To this end, several theoretical methods were used; namely first principle calculation and Monte Carlo Simulation (MCS).

2. Model and Methods of Calculations

2.1. First principle calculations

The primitive unit cell having cubic structure with *Pnma* symmetry was used for these calculations. All the calculations were performed using DFT under periodic boundary conditions, as implemented in WIEN2k code.[137] Linearized augmented plane wave method was employed that makes no shape approximations to the potential and density. Local orbitals were added for Mn, Ga, and Al and C semi core states for improved and flexible basis sets. The total energy was minimized using mesh of 10×10×10 k-grid points and 12×12×12 k-grid points in the integrated Brillouin zone for Mn_3GaC and Mn_3AlC respectively. Electronic wave functions are Fourier expanded inside non overlapping spheres of radius RMT. Plane wave expansion is used in the interstitial region. States lies below 7eV were treated as core states. The size of the basis set determined by $RMT \times K_{max}$ was set equal to 7. Scalar relativistic treatment was used for relativistic effects of valence states. On the other hand, core states were treated by a fully relativistic treatment. Self-consistent cycle converged until the total energy and charge of the system was equal to 1×10^{-4} mRy per unit cell and $1\times10^{-3}e$ respectively. Equilibrium volume was found by calculating total minimum energy as a function of seven different volumes at fixed *a, b and c*, where *a, b* and *c* are the lattice parameters in Å. Here *a, b* and *c* are the lattice

parameters in Å. The minimized "*a*" was used to obtained equilibrium volume and thus lattice constants. The optimized relaxed lattice structure was used for all subsequent calculations. Structural, magnetic and electronic properties for all samples were investigated by using spin polarized calculations with PBE-GGA xc-functional.[132]

2.2. Monte Carlo Simulation:

The magnetic and magnetocaloric properties of Mn_3GaC and Mn_3AlC, have been performed using Monte Carlo simulation and mean field theory. To simulate the two compounds, we used the following Hamiltonian:

$$H = -J_1 \sum_{<i,j>_1} S_i S_j - J_2 \sum_{<i,j>_2} S_i S_j - \Delta \sum_i^N S_i^2 - \mathrm{H} \sum_i^k S_i \qquad (1)$$

Where,

- J_1 and J_2 are the magnetic exchange couplings between the first and second nearest neighbors of the Mn atoms respectively.
- $< ij >$ Stands for the first nearest neighbors' sites i and j.
- $< i, j>_1$: represents the first nearest neighbor.
- $<i, j>_2$: represents the second nearest neighbor.
- S_i ; S_j are the spin random variable which takes the values ±1, 0.
- Δ and H are the crystal field and the external magnetic field applied on all system sites respectively

To perform the MCs, the Metropolis algorithm was used, boundary conditions on the lattice were imposed and configurations were generated by sequentially traversing the lattice and making single-spin flip attempts. Spin flip is chosen based on the energy difference between the considered spin and its neighbors. If the energy difference is negative, the spin will flip directly. If not, it will flip if the randomly chosen number is smaller than the Boltzmann factor $e^{-\beta H}$. Our data was generated at 10^5 Monte Carlo steps per spin, by discarding the first 10^4 Monte Carlo steps. First, multiple iterations were performed to achieve thermal equilibrium; they were followed by more iterations to calculate some physical quantities like energy per site, magnetization and magnetic susceptibility.

The total magnetization, specific heat and susceptibility are given respectively in Eqs. (2) to (4):

$$\mathrm{m} = \frac{1}{N} \sum_i S_i \qquad (2)$$

$$C_V = \frac{1}{k_B T^2} (< E^2 > - < E >^2) \qquad (3)$$

$$\chi_i = \frac{1}{k_B T} (< m^2 > - < m >^2) \qquad (4)$$

Where $\beta = \frac{1}{k_B T}$, and k_B is the Boltzmann constant which will be fixed at $k_B = 1$.

Using Monte Carlo simulations, the magnetocaloric properties were evaluated using Eqs. (5) to (7) below.

The magnetic entropy change is given by: $\Delta S_m = \int_{h_i}^{h_f} (\frac{\partial M}{\partial T})\, dh$ (5)

Where $\left(\frac{\partial M}{\partial T}\right)$ is the thermal magnetization for a fixed magnetic field H_i.

The adiabatic temperature change is given by: $\Delta T_{ad} = T \frac{\Delta S_m}{C_m}$ (6)

And the RCP (relative power cooling) is given by: RCP $= \delta_{FWHM}\, \Delta S_m^{Max}$ (7)

where δ_{FWHM} is the full width at half maximum in the ΔS_m(T) curve.

The exchange coupling parameters (J_1, J_2) and the crystal field (Δ) were investigated by using first principle calculations at T=0K by applying Eqs. (8) to (10) shown below.

$$J_1 = \frac{E_{ant1} - E_{fer}}{S_i S_j Z_1} \quad (8)$$

$$J_2 = \frac{E_{ant2} - E_{fer}}{S_i S_j Z_2} \quad (9)$$

$$\Delta = \frac{E_a}{\sum_i (S_i)^2} \quad (10)$$

Where, E_{fer}, E_{ant1}, and E_{ant2} are the energies of ferromagnetic, antiferromagnetic type 1 and antiferromagnetic type 2 configurations, respectively.

Z_1=8 and Z_2=6 are the number of first nearest and second nearest neighboring ions for each sub-lattice, respectively.

E_a is the magnetic anisotropic energy which is equal to the difference of the energy between the low and high energy positions.

3. Crystal structure of Mn_3AC (A=Ga, Al) compounds

3.1 crystalline structure of Mn_3AC (A=Ga, Al) compounds.

The alloy Mn_3AC (A=Ga, Al) has a metallic antiperovskite structure with *Pm*-3*m* symmetry. Fig. 34(a) shows the unit cell of Mn_3GaC and Mn_3AlC compounds respectively, which have plotted by using vesta software. The carbon atom is located at the (1/2, 1/2, 1/2) position in the center of an octahedron of Mn atoms, and the Ga/Al atoms are located at (0, 0,0). The cubic cell of Mn_3GaC has a lattice constant of 3.8942 nm,[75] and Mn_3AlC has a lattice constant of 3.873 nm.[81]

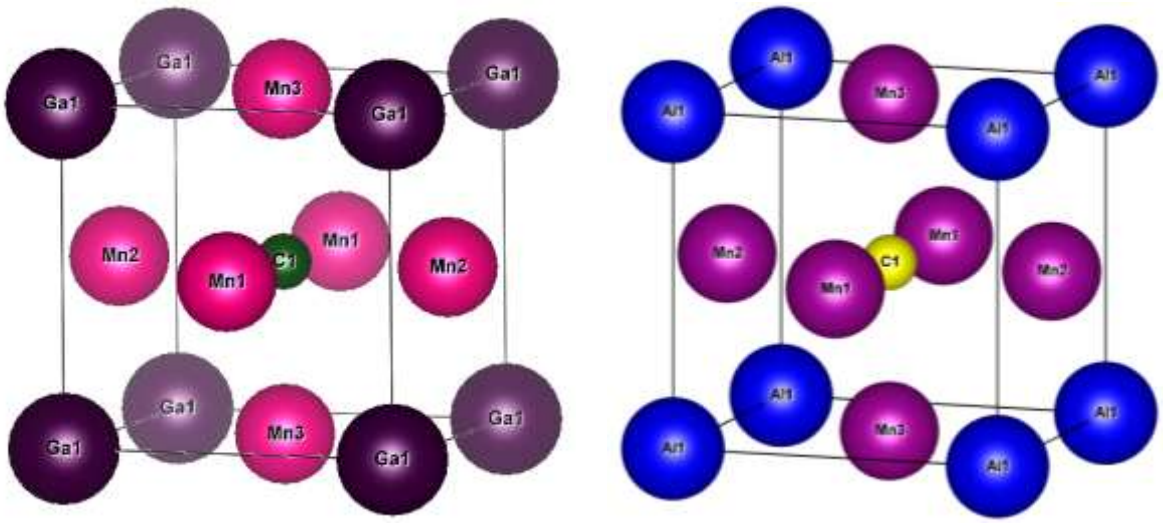

***Figure 334**. Unit cell structure of Mn_3AC (A=Ga, Al) crystallizes in the cubic anti-perovskite structure.*

3.2. Geometry Optimization

3.2.1. Convergence of K-points

To obtain the number of k-points, which minimize the total energy of the system. A convergence test of the number of special points used in the first Brillouin zone was calculated. To investigate the minimum number of k-points in the Brillouin zone from which a convergence in the total energy is ensured, we have calculated the total energy for different k-points values and plotted its variation. Figure 35 shows this variation for both compound Mn_3AC (A= Ga, Al). The optimal K-points minimizing the total energy of the system correspond to K-points =10x10x10 for Mn_3GaC and K-points =12x12x12 for Mn_3AlC. Before specifying the minimum number of K-points, we first determined the R_kmax which is given by: R_kmax = Product of the radius of the smallest sphere of radius muffin tin RMT by the cut-off energy of the plane wave base (Kmax). For a precise calculation, we have used an $R \times K_{max} = 7$ for both compounds.

(a)

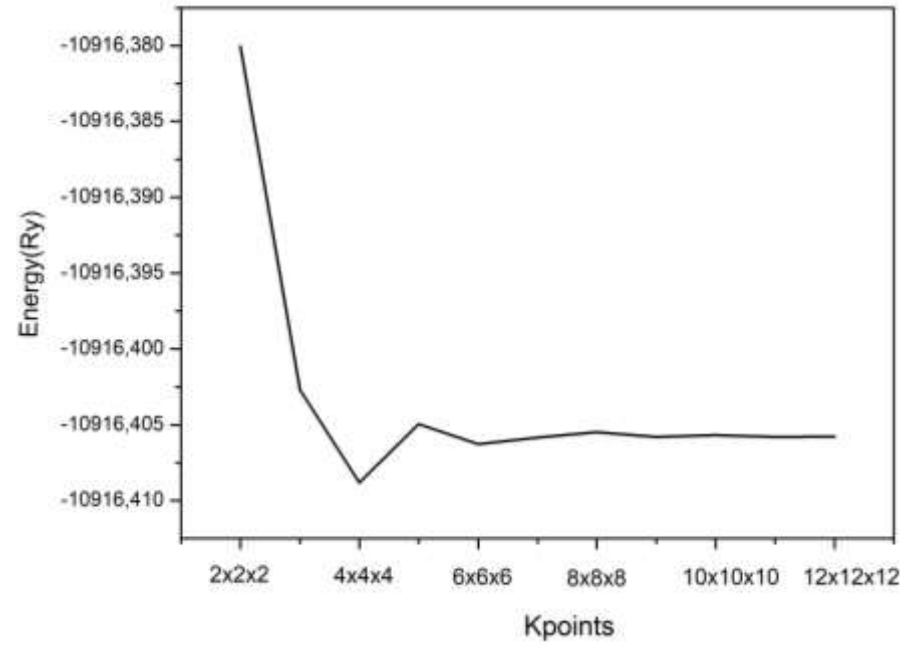

(b)

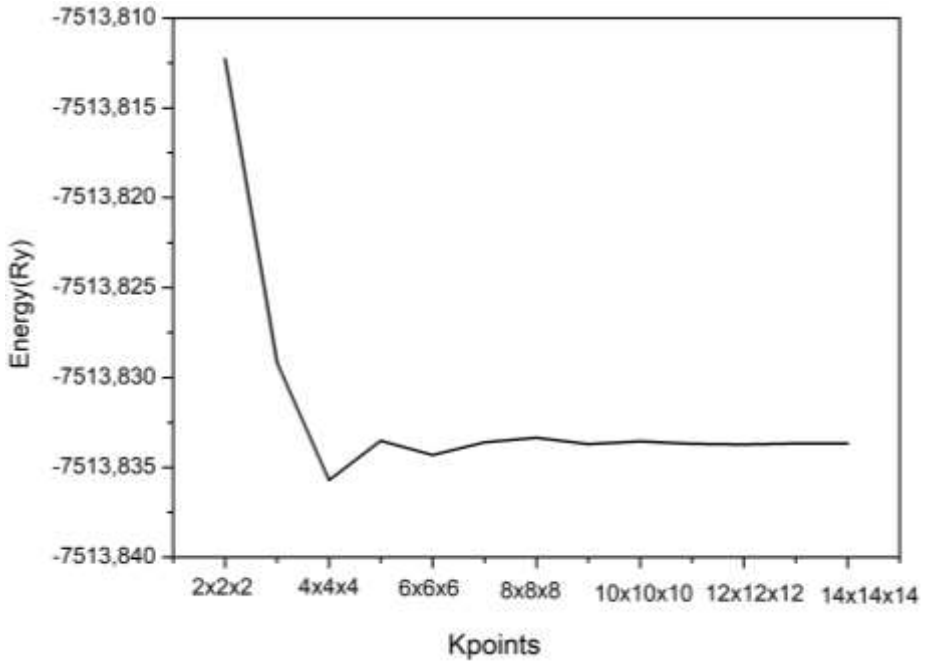

Figure 345. *Total energy variation as a function of K-points by GGA. (a)Mn_3GaC, (b) Mn_3AlC*

3.2.2 Total Energy as a function of volume

In order to determine the equilibrium structure of Mn_3AC (A= Ga, Al), geometry optimization of the experimental structure was performed. The optimization was investigated by using GGA approximation. Equilibrium volume was found by calculating total minimum energy as a function of seven different volumes at fixed *a, b and c*, where *a*, *b* and *c* are the

lattice parameters in Å. The structural optimization of Mn_3AC (A= Ga, Al) compounds were carried out by minimizing the total energy as a function of volume V. The optimization cycle is repeated until convergence is reached.

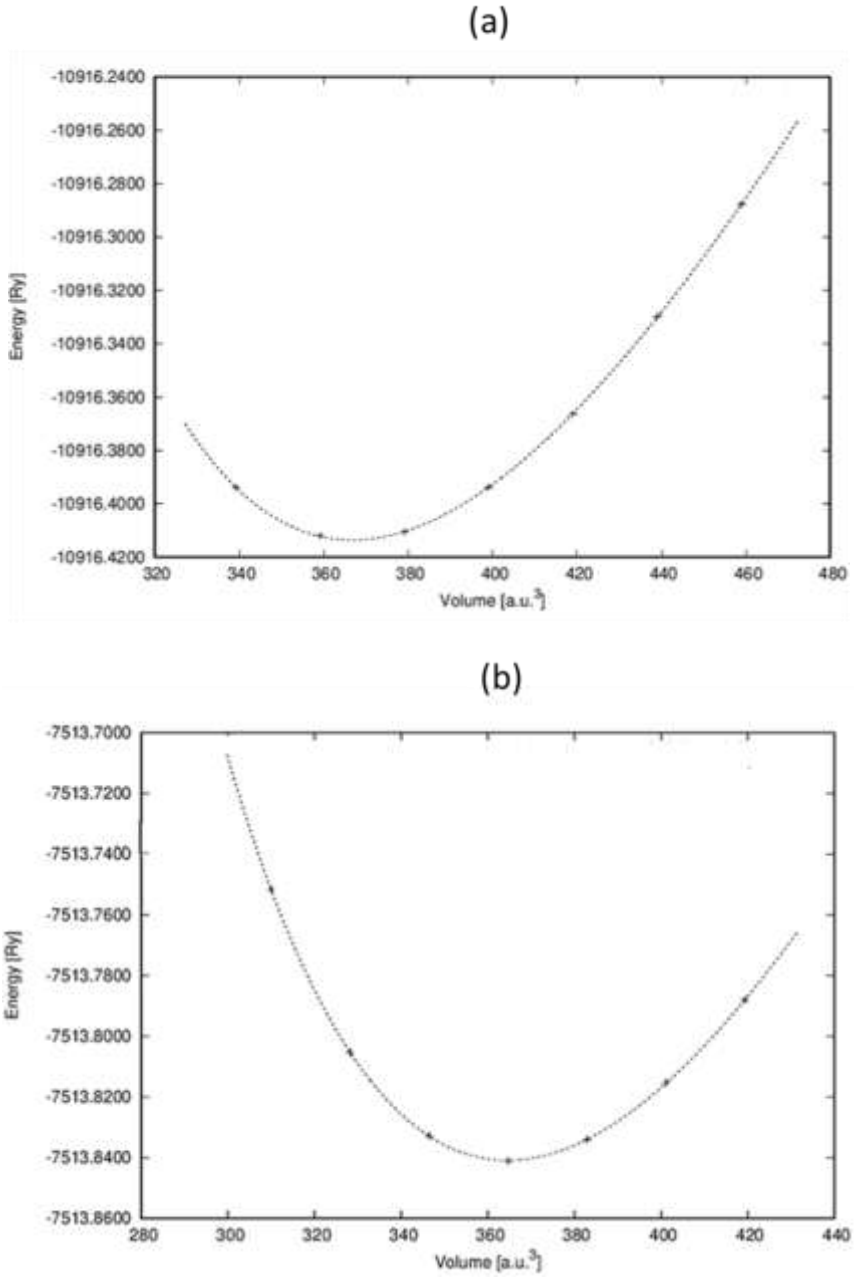

Figure 36. *Total energy variation as a function of volume of a) Mn_3GaC b) Mn_3AlC compounds with GGA approximation.*

The table below represents the experimental and the calculated parameters (the lattice constant and the volume of the system) of Mn_3GaC and Mn_3AlC respectively using GGA approximation. The optimized lattice parameters are in good agreement with experimental results.

		Volume V(Å)	Lattice parameter *a*(Å)
GGA calculations	Mn_3GaC	54.31	3.787
	Mn_3AlC	54.01	3.780
Experimental	Mn_3GaC[75]	59.04	3.894
	Mn_3AlC[81]	58.09	3.873

Table 2. *Experimental and optimized lattice parameters by GGA approximation*

4. Results and discussion

4.1. Mn_3GaC compound

4.1.2. Band structure of Mn_3GaC compound

The band structure calculation of the metallic antiperovskite Mn_3GaC compound for spin down, spin up channels, respectively, have been performed by using GGA along with high symmetry directions of Brillouin zone. The computed band structure of Mn_3GaC for spin down and spin up are given in Fig. 37(a), (b) in which it exhibits a metallic nature. Around Fermi level, there is a band crossing, which are originated from the valence electrons of Mn, also it can be seen that in the valence band, the energy region below -4 eV consists mainly of the *s* and *p* electrons of Ga and C atoms for both spins down and up respectively. However, in the energy region between –4 and 6 eV it consists mainly of the d electrons of Mn atom.

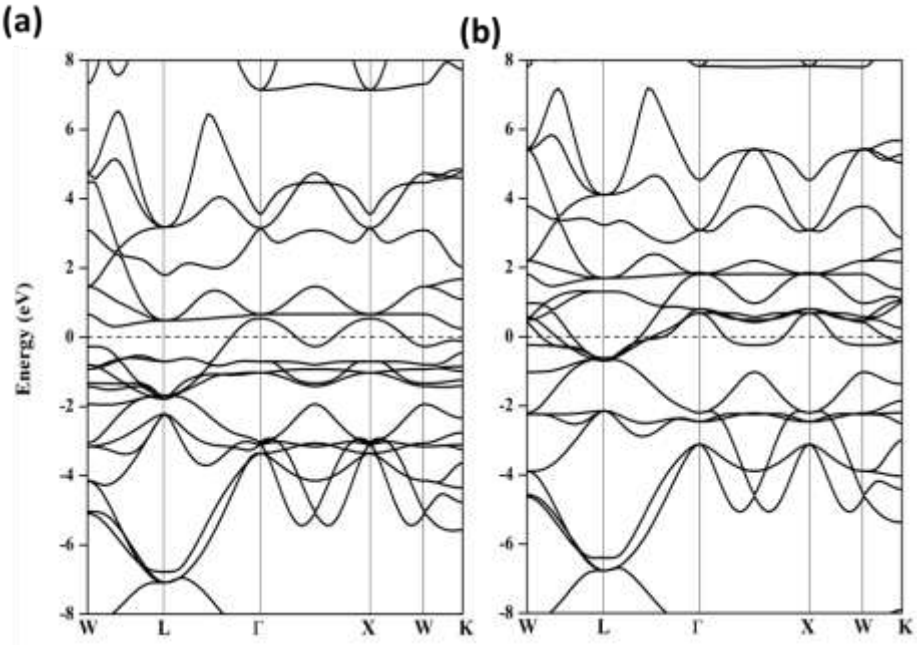

Figure 357. *Mn_3GaC band structure with GGA approximation (a) Spin up and (b) Spin down at T=0K.*

4.1.3. Density of States (DOS)

It is observed from Fig. 38 that the maximum contribution in total DOS is due to the Mn atom in both spin up and spin down, whereas the Ga and C atoms have a low contribution in total DOS for both spin up and down. The contribution in Mn DOS is mainly due to Mn-*d* electrons in the valence and conduction region, in the partial and total DOS, the electronic states at E_F (Fermi level) are completely due to the d state electrons of transition metal atom Mn. At the E_F level, there is an overlapping between the valence band and the conduction band, which confirms the metallic behavior of Mn_3GaC for both spin up and down. Furthermore, the asymmetrical shape between spin up and spin down proves that we have a magnetic compound, where the magnetism comes totally from the orbital *d* of Mn atom.

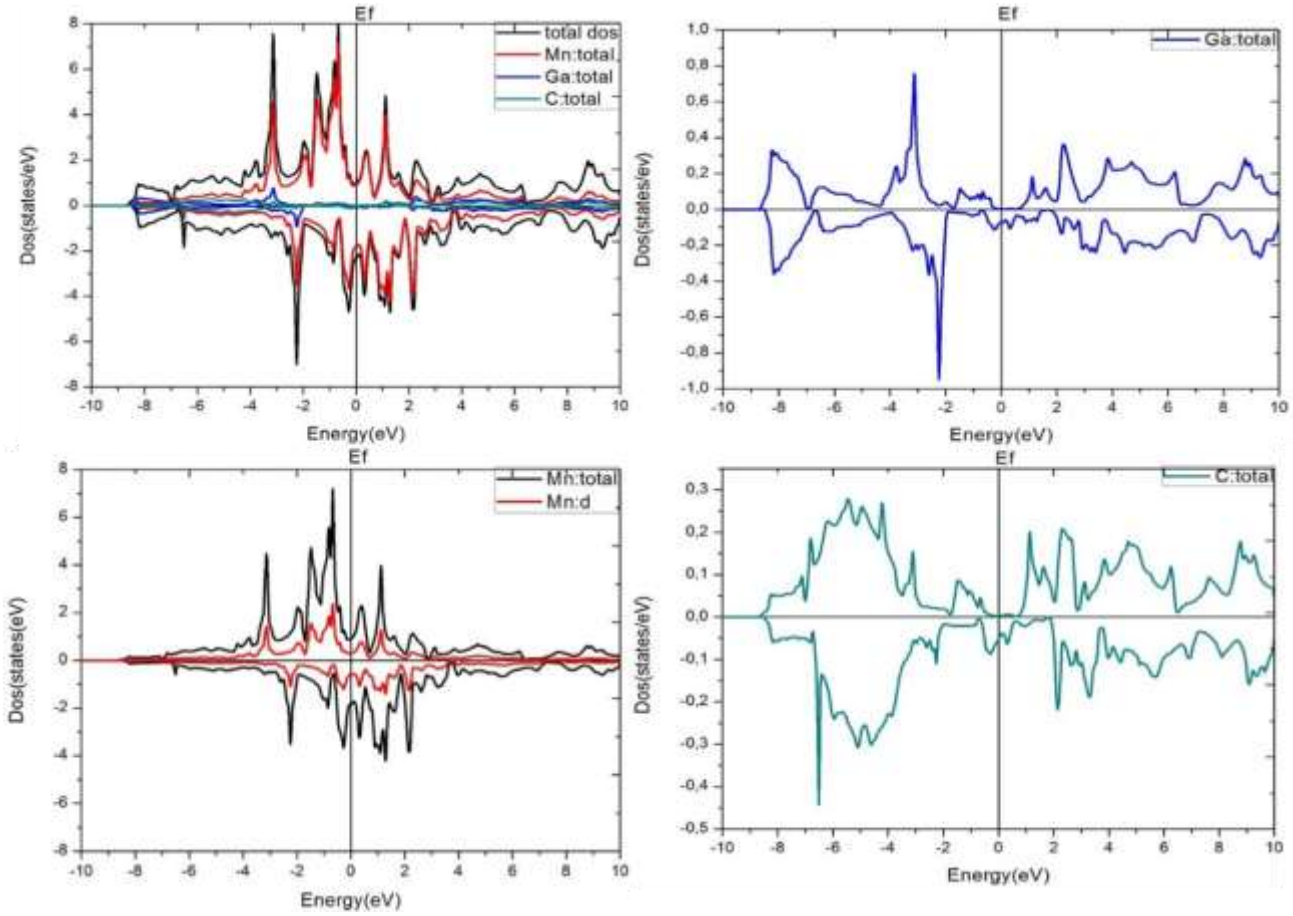

Figure 368. Total and partial electronic DOS of Mn_3GaC compound at T=0K.

4.1.4 Magnetic and magnetocaloric properties of Mn_3GaC

To calculate the magnetic and magnetocaloric properties of the metallic antiperovskite Mn_3GaC compound, we have used Monte Carlo simulation at non null temperatures. All these properties are plotted as a function of the temperature and the external magnetic field H. The input data

like the magnetic moment and the magnetic exchange coupling interactions have been investigated from the first principle calculations. We explore the Monte Carlo simulation to study the effect of the temperature on the magnetization, susceptibility and specific heat profiles. In Fig. 39, are represented the profiles of the magnetization, susceptibility and specific heat as a function of the temperature. However, this figure is made for fixed values of the magnetic exchange coupling interactions: J_1=35.78 meV, J_2=40.16 meV, and crystal field Δ=0.0053 meV with zero external magnetic field H=0 T. From Fig.39, it is very clear that for low values of the temperature T(K), the magnetization is in good agreement with the corresponding value of spin state in the case of T=0 K (S=1), also, the corresponding susceptibility and specific heat shows a notable peak around the curie temperature $T_C \approx 250K$, which corresponds to the peak of the susceptibility (see Figure 39). The curie temperatures of the antiperovskite Mn_3GaC compound obtained by Monte Carlo simulation and experimental study are listed in Table 3. It is very clear that, the Curie temperature calculated by Monte Carlo simulation is in good agreement with the experimental value.[66]

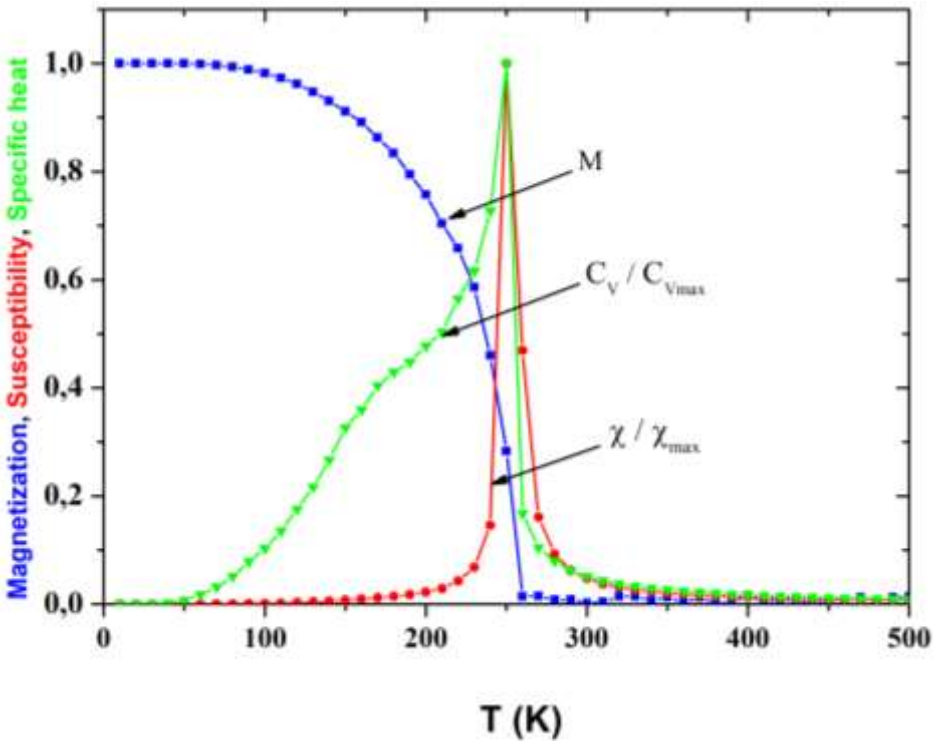

Figure 3937. *The behavior of the magnetization, the susceptibility and the specific heat as a function of the temperature of the Mn_3GaC compound, for H=0T*

	Experimental studies	MC simulations
Curie temperature Tc of Mn_3GaC compound	249K[75]	250 K

Table 3. *The comparison between the experimental critical temperature and that obtained*

Fig. 40 shows the temperature dependency of $-\Delta S_m$ under appliance of a magnetic fields of H=1T, 3T and 4.5T. The values of $-\Delta S_m$ are negative in the entire temperature range and is extended over a wide range of the temperature around T_C, which is useful for above room temperature magnetic refrigeration. Obviously, with increasing H, the value of $-\Delta S_m$ increases gradually and reaches the maximum value of about 5.65 J/kg·K at H=4.5T. The obtained value was close to the experimental one $-\Delta S_m$ =4.30 J/kg·K[73] at the same applied magnetic field H=4.5T.

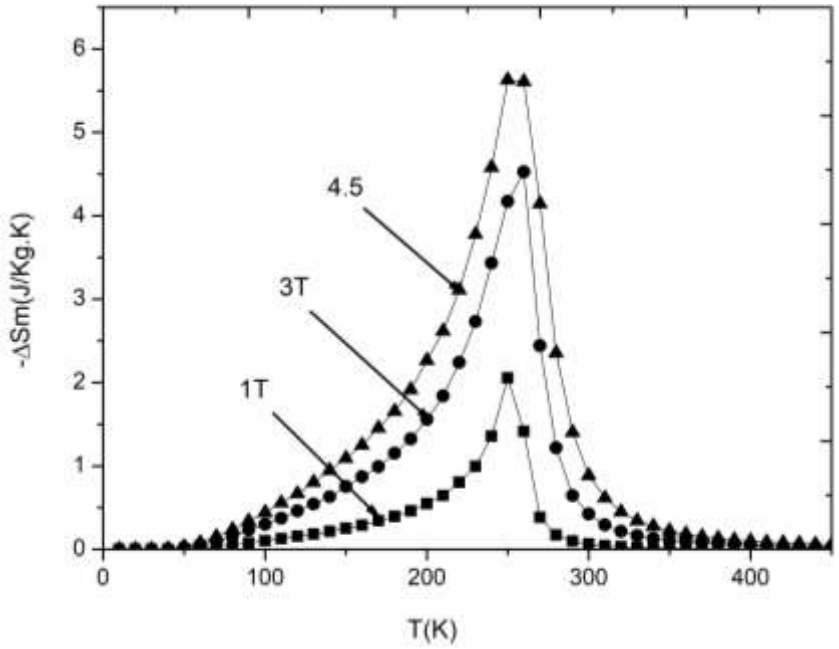

Figure 380. *Magnetic entropy change of Mn_3GaC compound as a function of temperature under different applied fields*

Another measured magnetocaloric property of metallic antiperovskite Mn_3GaC compound is illustrated in Fig.41, which is the adiabatic temperature change (ΔT_{ad}) as a function of the temperature for different values of the external magnetic field H = 1T, 3T and 4.5T. However, it can be seen that the maximum value of the adiabatic temperature change (ΔT_{ad}=13.81K) around 260 K is obtained to be close to the Curie temperature with an applied magnetic field of

H=4.5T. These results indicate that $MnGa_3C$ compound sample is a good substance for magnetic refrigeration applications.

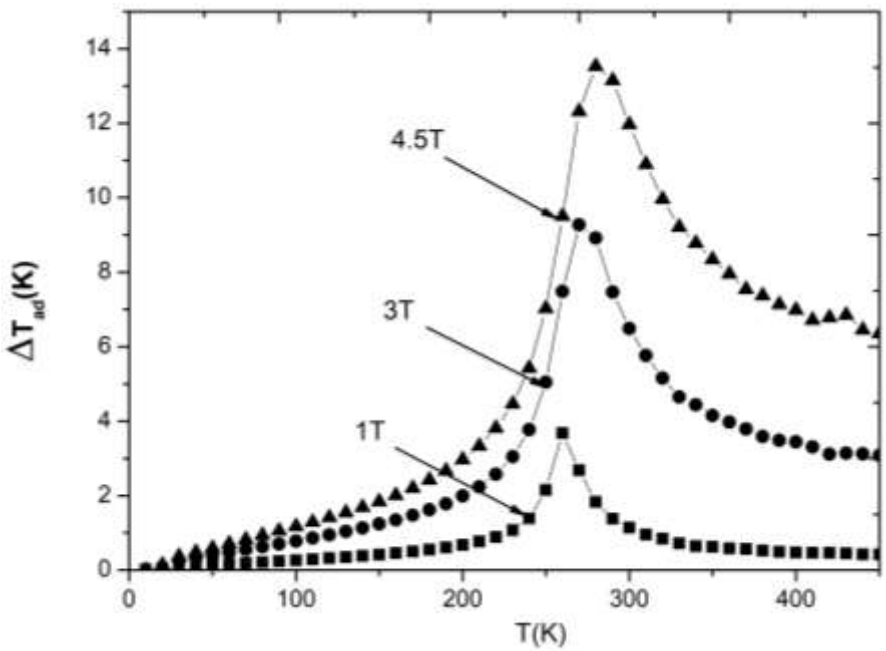

Figure 391. *Temperature dependence of the adiabatic temperature change ΔT_{ad} for Mn_3GaC compound*

The relative cooling power (RCP) is an important parameter for selecting potential substances for magnetic refrigerants, providing a measure of how much heat can be transferred between the cold and hot sinks in an ideal refrigerant cycle.[187,188] Fig. 42 shows the relative cooling power (RCP) versus the external magnetic field for Mn_3GaC compound at different magnetic fields of 1T, 3T and 4.5T. It is found that the RCP increases monotonically as the magnetic field increases, and reaches the value of 351.90 J/kg for H=4.5T. We note that all the parameters related to the magnetocaloric effect, such as the magnetic entropy change, adiabatic temperature change and relative cooling power depends strongly on the magnitude of the external magnetic field H and the exchange coupling interactions between Mn atoms.

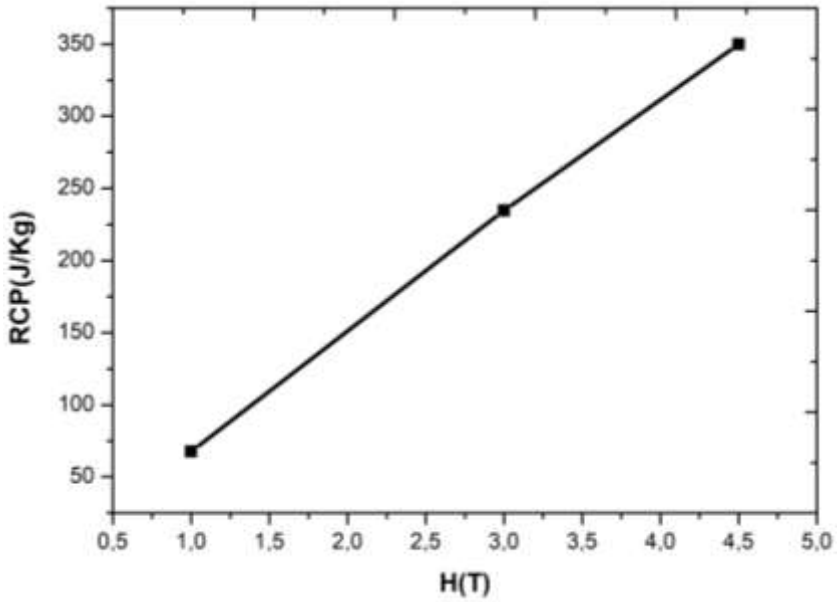

Figure 42. *Field dependence of the relative cooling power (RCP) of Mn_3GaC compound*

4.2. Mn_3AlC compound

4.2.1. Band structure of Mn_3AlC compound

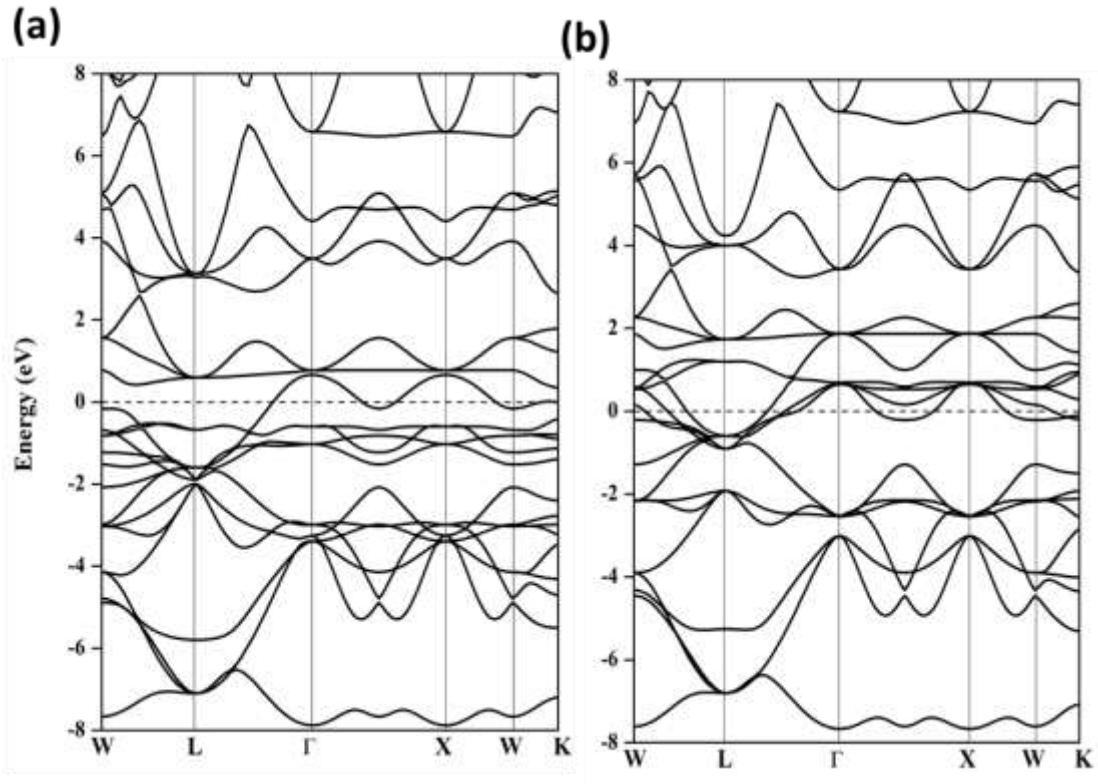

Figure 43. *Band structures of Mn_3AlC with GGA approximation for (a) Spin-up (b) Spin-down.*

For the electronic properties, all the calculations were performed by applying the GGA approximation along the higher symmetry directions of the Brillouin zone Fig. 43a and b show that the band structure obtained from both spin-up and spin-down electrons, is exhibiting a metallic behavior. However, around Fermi level, there are bands crossings originating from the valence electrons of Mn atoms, the same two graphs also show that in the valence band, the energy region below -5eV consists mainly of Al and C 's' and 'p' orbitals, for both spin-up and spin-down states respectively. However, the energy region between –5eV and 5eV consists mainly of ‘d’ orbitals of Mn.

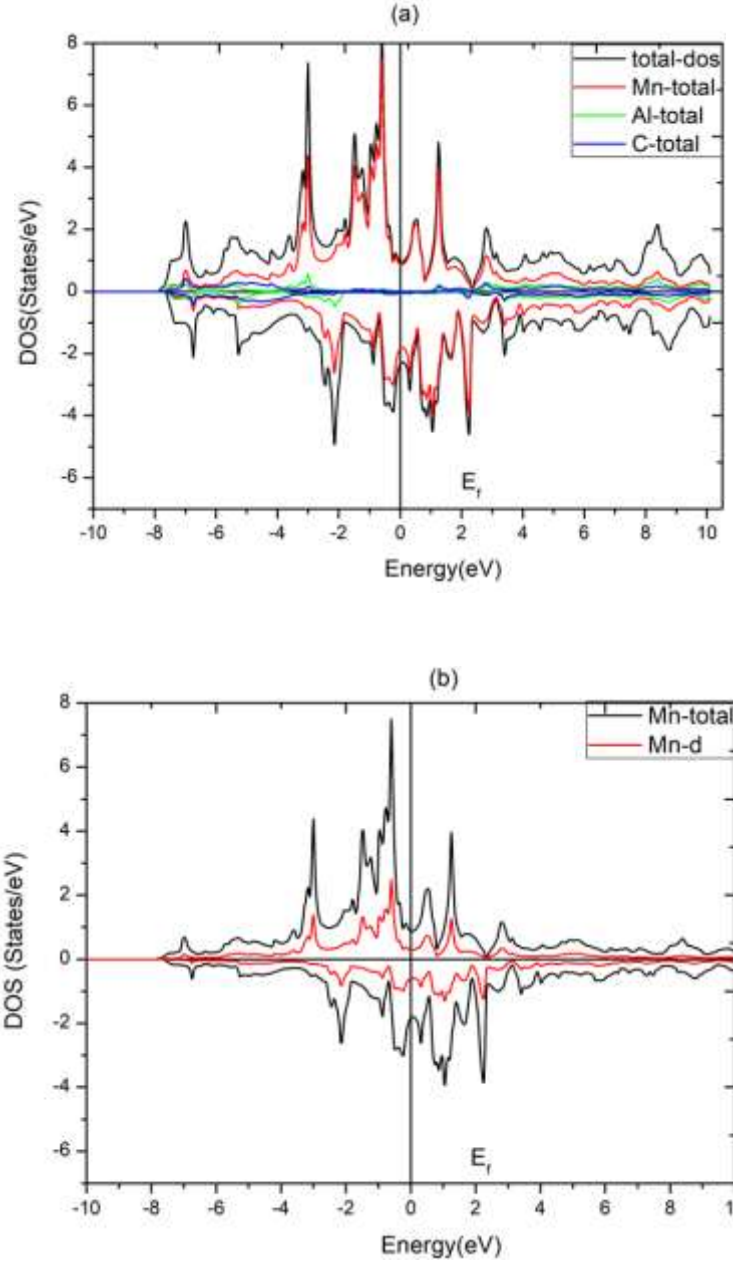

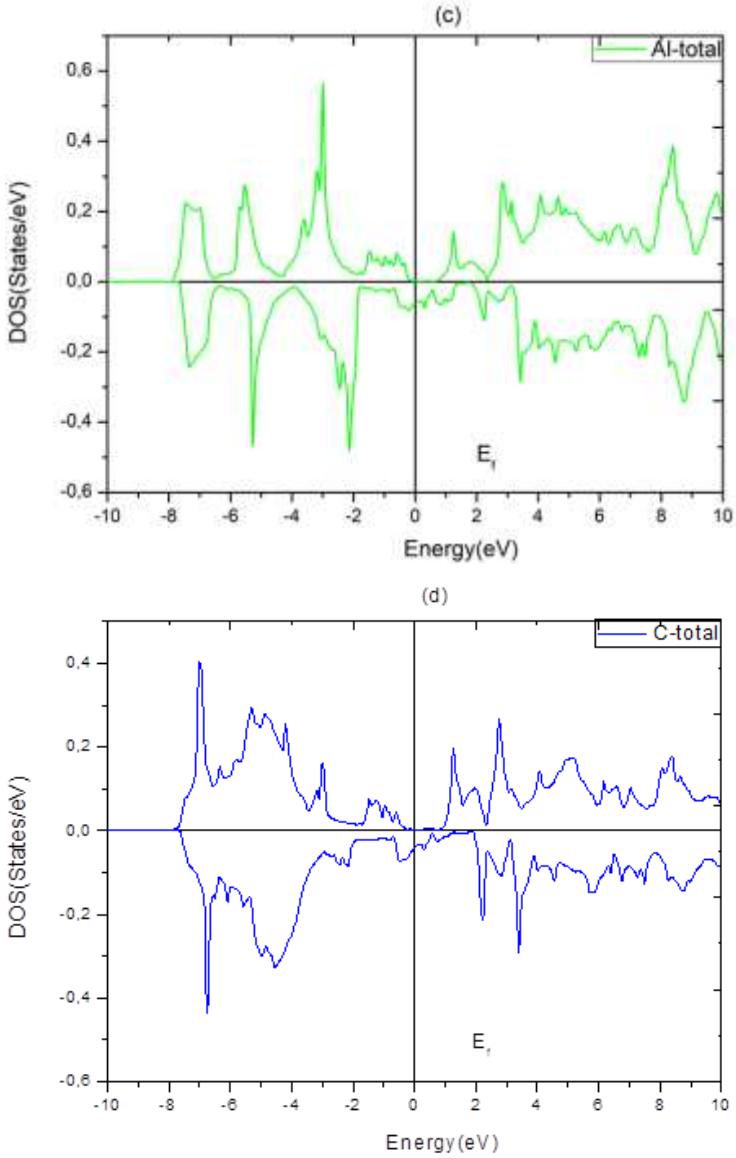

Figure 404. *(a) Total electronic DOS of Mn3AlC (b) Mn DOS (c) Al DOS (d) C DOS*

The total and partial density of states (DOS) plots of Mn_3AlC are shown in Fig. 44. From Fig. 44 a and b we can see that the maximum contribution in the total DOS is made by the Mn atom in both spin-up and spin-down states, whereas the Al and C atoms are lowly contributing to the DOS, also in both spin states, according to Figs. 44(c) and (d). The contribution to Mn in the DOS is mainly made by *s* orbitals in the valence and conduction region (cf. fig. 44(b)). At the partial and total DOS, the electronic states at E_f (Fermi level) are completely due to the fact that the electrons of transition metal Mn occupy the d-orbital. Moreover, DOS values at E_f in Figs. We can also conclude that the compound is metallic in nature. Additionally, the asymmetrical nature of spin-up and spin-down graphs from the density of states demonstrate the magnetic nature of Mn_3AlC.

4.2.2. Magnetic, magnetocaloric and transport properties of Mn_3AlC

The magnetic properties of Mn_3AlC have been determined using Monte Carlo simulations and at non-null temperatures. Fig. 45 displays the behavior of magnetization, susceptibility and magnetic-specific heat as a function of temperature, for fixed values of magnetic exchange couplings (J_1=44.38 meV and J_2=43.67 meV), and crystal field (Δ=0.0145 meV) under no external magnetic field. This figure shows that, for low values of T(K), the magnetization is in good agreement with the corresponding spin-state especially in the case of T=0K (S=1). The corresponding susceptibility and magnetic-specific heat peak can be seen at around T_C = 290K, this temperature corresponds to the peak value of susceptibility (see, Fig. 45). However, the Curie temperatures of the Mn_3AlC compound obtained using Monte Carlo simulations and experimental study are listed in Table 4. The Curie temperature obtained by Monte Carlo simulation T=290K is in good agreement with the experimental value Tc=287K.[81]

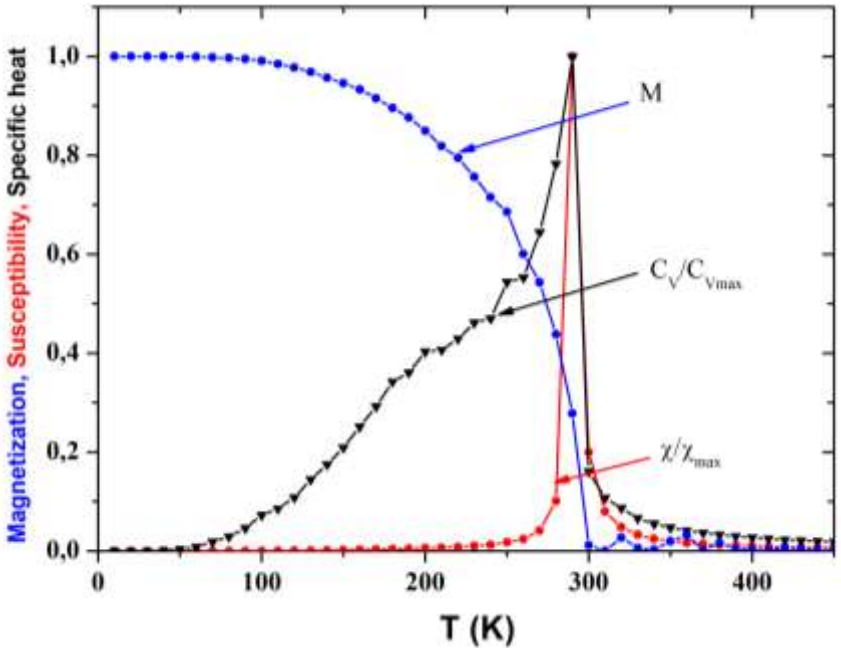

Figure 415. *The behavior of magnetization, susceptibility and specific heat as functions of the temperature of Mn3AlC, for H=0T*

	Experimental results	MC simulations
Curie temperature of the Mn_3AlC compound (T_C)	287 K[81]	290 K

Table 4. *Comparison between the experimental critical temperature and those obtained*

In a previous study, Wang et al.[81] discussed the magnetocaloric properties of the anti-perovskite compound according to the Landau theory of phase transition.[189] The anomalous results found were not in good agreement with experimental data, because of the additional contribution of magnetoelastic and magnetoelectronic couplings, which were used to investigate the ferromagnetic-paramagnetic transition of Mn_3AlC, and are based on free Gibbs energy G.[128] Based on what Wang et al. found during their study, and as was mentioned above, there is a clear difference between the experimental results and those found using the magnetoelastic couplings method. In fact, the value found for ΔS_m^{Max} in magnetoelastic couplings was 35 J/Kg·K under an applied magnetic field of 4.5T, while T_C was found to be 184K,[81] while the experimental results, under similar conditions, were 3.28 J/Kg·K and 287K respectively.[81]

The incompatibility between both results was the main reason behind our choice to use Monte Carlo simulation, in order to improve the results obtained by the magnetoelastic and magnetoelectronic couplings method. MC simulations results have matched experimental values much more closely. Fig. 46 represents our Monte Carlo simulation results, which determined that the maximum value of ΔS_m^{Max} is approximately 6.40 J/Kg. K under 4.5T, while T_C was found to be 290K.

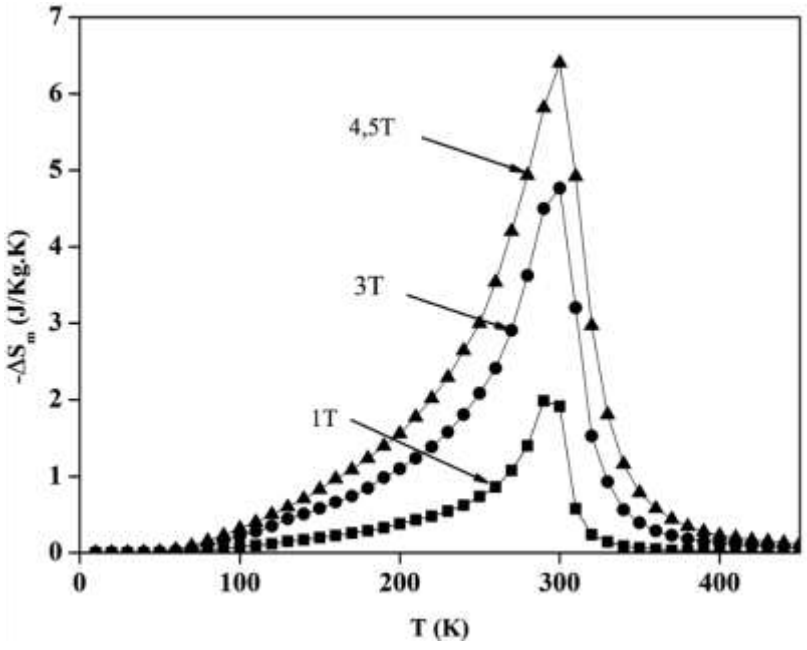

Figure 46. *Magnetic entropy change of Mn_3AlC as a function of temperature under different magnetic fields of 1T, 3T and 4.5T*

Other important factors for MCE materials are the adiabatic temperature change ΔT_{ad} and the relative cooling power RCP, the latter is an important parameter, defined as the amount of heat transfer between hot and cold reservoirs in an ideal refrigeration cycle. These two parameters were also calculated using Monte Carlo simulations. The maximum value of ΔT_{ad} was 13.60K and the RCP was found to be 416.96 J/Kg under an applied magnetic field of 4.5 T, (see Figs. 47 and 48). Table 5 below represents a comparison between our results by Monte Carlo simulation and those obtained by using the magnetoelastic couplings method in comparison with experimental data.

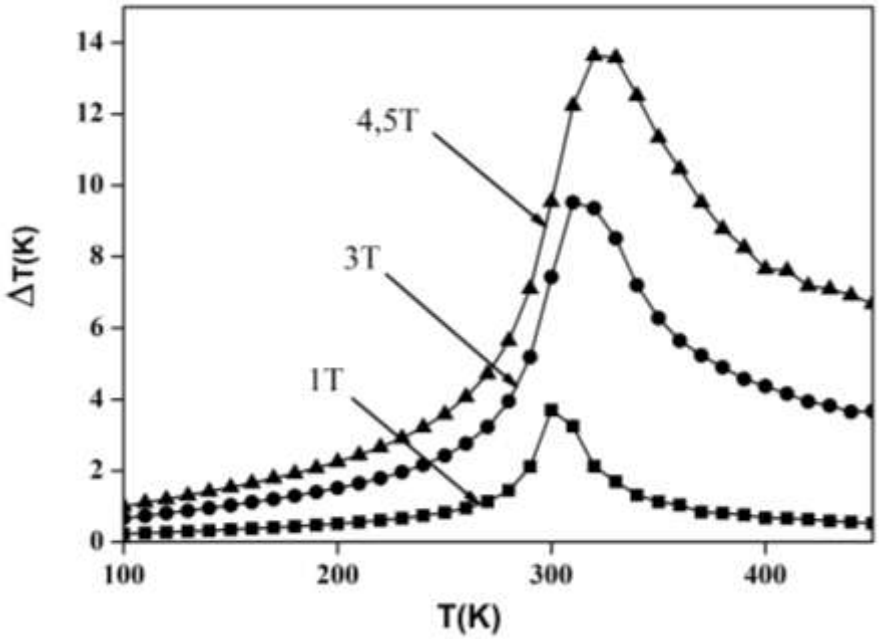

Figure 47. *Adiabatic temperature change of Mn_3AlC as a function of temperature under different magnetic fields of 1T, 3T and 4.5T*

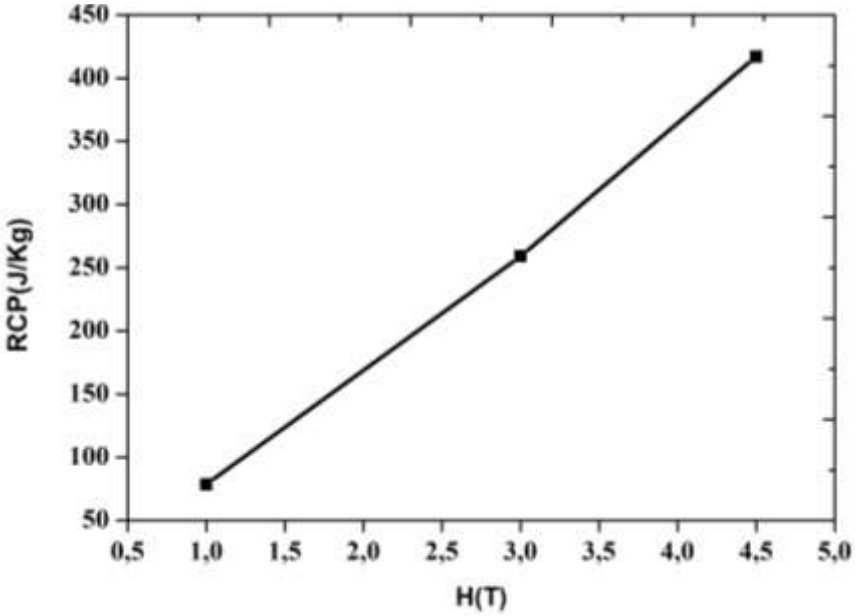

Figure 48. *Field dependence of relative cooling power (RCP) of $AlCMn_3$*

Magnetic field (Tesla)	Experimental[81]			Magneto-elastic couplings[81]			MCS (This work)		
H=4.5T	$\lvert\Delta S_m^{Max}\rvert$ (J/Kg.K)	ΔT_{ad} (K)	RCP (J/Kg)	$\lvert\Delta S_m^{Max}\rvert$ (J/Kg.K)	ΔT_{ad} (K)	RCP (J/Kg)	$\lvert\Delta S_m^{Max}\rvert$ (J/Kg.K)	ΔT_{ad} (K)	RCP (J/Kg)
	3.28	1.62	328	35	-	-	6.40	13.60	416.96

Table 5. *Comparison between the experimental magnetocaloric properties and those obtained by magneto-elastic couplings and Monte Carlo simulation for H=4.5T.*

The transport properties of Mn_3AlC including Seebeck coefficient and the electronic thermal conductivity were performed using BoltzTraP code interfaced with WIEN2K and based on the Boltzmann semi-classical transport equation. As shown in Fig. 49, Seebeck coefficient S (T) was measured at zero magnetic fields for temperatures ranging from 10 to 360K with GGA approximation. Below 110 K, the values of S(T) found to be negative, which means that the electrons are the dominant carrier in this area. The sign of the Seebeck coefficient changes from negative to positive at around 110K, when the temperature increases; it could be related to the enhancement of phonon scatterings. The result found of S(T) is qualitatively in good agreement with what Wang et al.[81] found However, by looking at the values it can be seen that quantitatively the results were further from experimental data; it was the reason why GGA+U (Hubbard correction) was looked upon, in order to improve the values, but the results found with this correction were still far from experiment. This large difference between the experimental and the calculated values may be due to BoltzTraP code which couldn't account well for the observed S(T) in Mn_3AlC. Besides, Fig. 50 represents the variation of temperature as a function of the electronic thermal conductivity (K), which is not treated experimentally, it can be seen that the thermal conductivity increases linearly with the rise of temperature.

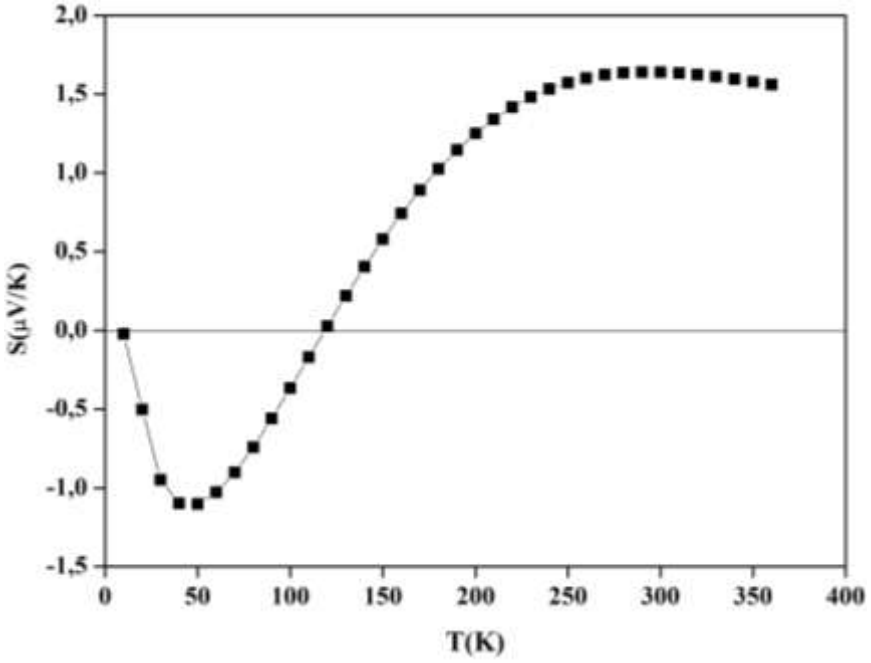

Figure 49. *Temperature dependence of SeebecK coefficient*

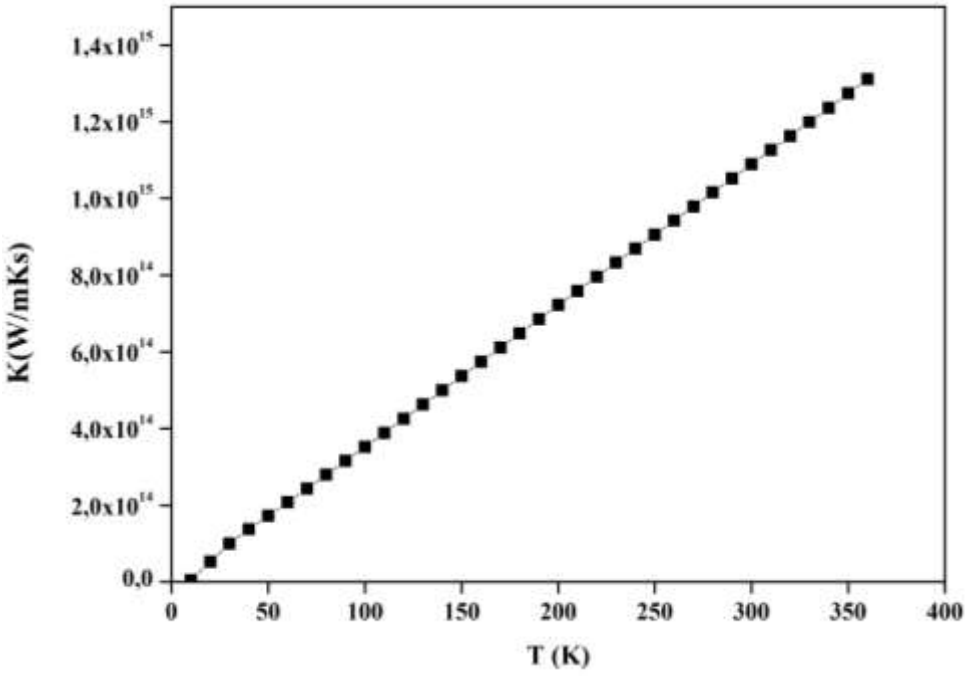

Figure 420. *Electronic thermal conductivity as a function of temperature*

Conclusion:

In conclusion, we carried out first principle calculations, and Monte Carlo simulations on the antiperovskite materials type Mn_3AC (A=Ga, Al) in order to study their structural, electronic, magnetic, magnetocaloric and transport properties. The obtained results include the magnetic entropy change $\Delta S_m^{Max} = 5.65\, J/Kg.k$, $\Delta S_m^{Max} = 6.4\, J/Kg.k$ and RCP=351J/Kg, RCP=416.96J/Kg at an applied magnetic field of H=4.5T for Mn_3GaC and Mn_3AlC

respectively. These results were found to be close to the experiment, as compared with those found by the magneto elastic coupling and the interaction between electrons. However, for the adiabatic temperature change the results were far from the experimental one. The present compounds Mn_3GaC and Mn_3AlC could be one of the promising candidates for magnetic refrigerants, working in a wide temperature range covering room temperature with absence of any hysteresis loss. For a better understanding and improvement of MCE and transport properties for this material, a further study is suggested by using other theoretical approaches.

Chapter IV. Fabrication of $CoFe_2O_4$ nanostructures

1. Formation $CoFe_2O_4$ nanorods by electrochemical deposition

$CoFe_2O_4$ vertically aligned cobalt ferrite nanorods were synthesized following 5 processes, as will be described: In the first step, commercial bulk Si wafers were used as substrates. While, a conductive gold layer was deposited on top of the silicon substrate to act as an electrode with high conductivity for the electrodeposition of $CoFe_2$ nanorods. In addition to that, a sputtering of a thick Al layer was performed on top of the gold electrode using an adhesive Ti inter-layer. For the 2nd step, an electrochemical anodization technique was used to oxidize the Al layer into the aluminum anodized oxide (AAO) template, this process led to the self-organization of the pores. In the 3rd step, a potentiostatic electrodeposition technique was used to fill the porous AAO template with the metal $CoFe_2$ nanorods. Following that, the 4th step consists in removing the hosting AAO template by using a chemical dissolution. The latter process led to the free-standing $CoFe_2$ nanorods array. Finally, the fifth step consists in transforming the $CoFe_2$ nanorods arrays into the insulating $CoFe_2O_4$ nanorods by using thermal annealing. More details in the synthesis steps will be shed light upon in the next section.

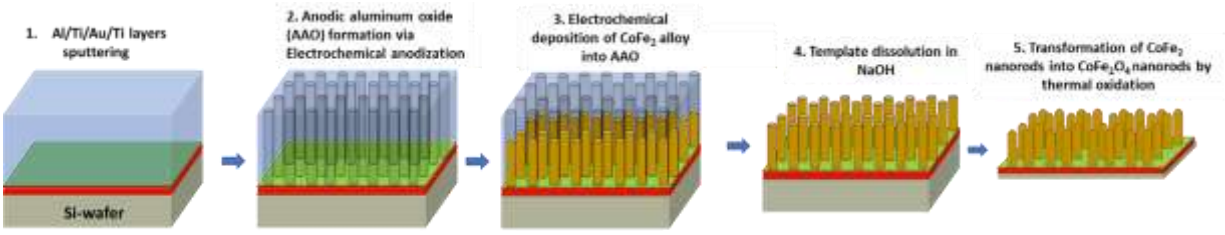

Figure 51. *Schematic summarizing the 5 needed steps required to fabricate a vertically aligned FM cobalt ferrite CoFe2O4 nanorods*

1.1. Experimental details:

For substrate preparation, aluminum film was deposited on silicon wafers that had been pre-coated with a thin titanium adhesion layer (a few nm) and gold (tens of nm) under-layer. The subsequent deposition of different layers was carried out by DC-magnetron sputtering (Plassys MP 500) equipment without breaking the vacuum. The anodization was conducted in oxalic acid solution (0.2 M) under constant cell potential and monitored with a self-written program in Igor Pro. Pore widening and barrier-layer etching were performed in phosphoric acid solution (0.5 M).[190] The process, described in the next sections, was tuned to obtain nanopores with average diameter of about 80 nm and spacing of 100 nm.

The electrodeposition of $CoFe_2$ nanorods was performed, by using an electrolyte composed of $CoSO_4.H_2O$ (0.05M), $FeSO_4.7H_2O$ (0.025M),boric acid (0.4M),and ascorbic acid (0.025M) $CoFe_2$ alloy was deposited into the AAO template with a potentiostatic voltage of 5V for approximatively 200s. For transforming the obtained $CoFe_2$ into $CoFe_2O_4$, the templates containing/and without $CoFe_2$ nanorods were subsequently heated in open air at different temperatures (T=100°C,200°C, 500°C,600°C) for different period of time respectively (1week, 2days, 24h and 12h) by using a thermal annealing furnace.

1.1.1. First Step: Substrate Preparation

As stated above, the first step consists at depositing a conductive Al/Ti/Au/Ti multilayer on top of Si wafers. The process of metallization responsible for smoothing and flattening the surfaces with thin metallic layers is usually conducted using a physical (PVD) or a chemical (CVD) vapor deposition technique. These advantage of these techniques, is that they allow to grow high quality films with good thickness control. Fig. 52 below, shows the deposition of a thin-film heterostructure on a Si substrate. The titanium layer serves as an adhesion layer to the gold electrode and the Al-film to be anodized. The Ti adhesion layer is usually an ultra-thin film of few nanometers (2–6nm) on top of which a Au-film of 5–20 nm is sputtered to serve as an electrode, followed by another thin layer of Ti (2-6nm) to serve once again as an adhesion between Au and a film of Al layer (500-600nm) to be deposited in the end. For a better improvement of the adhesion between Au and the subsequently deposited Al-film, it is suitable that the same Ti adhesion layer is used. The advantage of Ti manifests in its ability to form strong intermetallic bonds with both metals at the interface**.**

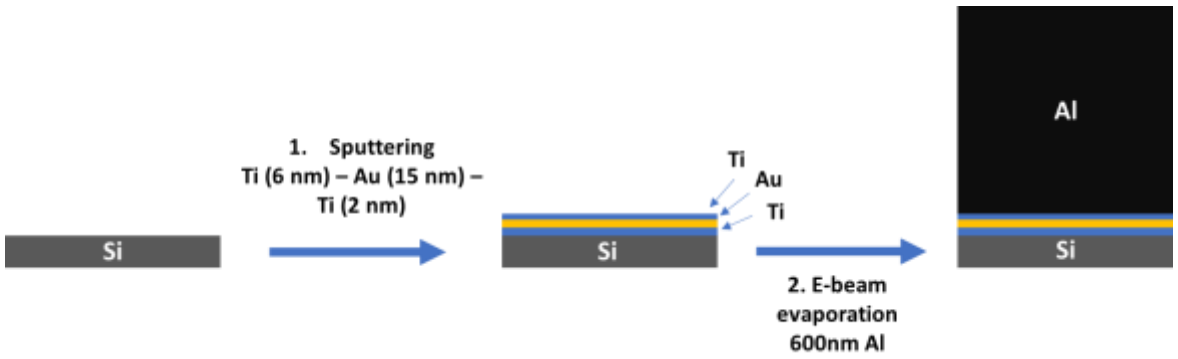

Figure 432. *Depiction of the silicon wafer coating with a metallic heterostructure of Ti (6 nm)/Au (15 nm)/Ti (2 nm) via sputtering followed by a layer of 600 nm of Al deposited via e-beam evaporation using high deposition rates to limit grain growth.*

1.1.2. Second step: Preparation of Porous Anodic Aluminum Oxide Templates (AAO)

The formation process of the nanoporous oxide layer is a complex process that produces a self-organized hexagonal pore array, these hexagonal honeycomb structures have been reported by several researchers.[191,192,193,194,195,196,197]

In general, the same process for anodization of Al foils in sulfuric, oxalic and phosphoric acids is used for the anodization of the supported Al layer. The anodization system is based on the electrochemical cell used for the potentiostatic electrodeposition of $CoFe_2$ nanorods arrays. While, the main role of the Au bar is to act as a cathode (counter electrode), and the supported Al layer act as an anode (working electrode) as shown in Fig.53. While, the electrolyte was a solution of oxalic acid.

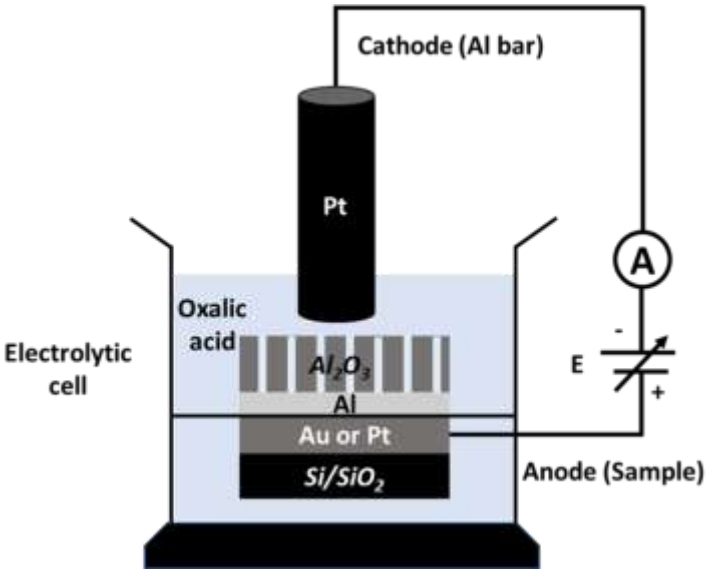

Fig 53. *Anodization setup for fabricating Porous Anodic Aluminum Oxide Templates (AAO)*

The main reactions followed for forming AAO are listed below:

Al anodization follows the sum reaction (1):

$$2Al + 3H_2O \rightarrow Al_2O_3 + 3H_2 \qquad (1)$$

Intermediate reaction (2) and (3) take place at the anode (oxidation of Al):

$$2Al \rightarrow 2Al^{3+} + 6e^- \qquad (2)$$

$$2Al^{3+} + 9H_2O \rightarrow Al_2O_3 + 6H_3O^- \qquad (3)$$

Hydrogen is released at the cathode (4):

$$6H_3O^+ + 6e^- \rightarrow 3H_2 + H_2O \qquad (4)$$

The time–current curve shown below (Fig.54), shows different segments followed for fabricating the AAO template that are well discussed in the literature.[198]

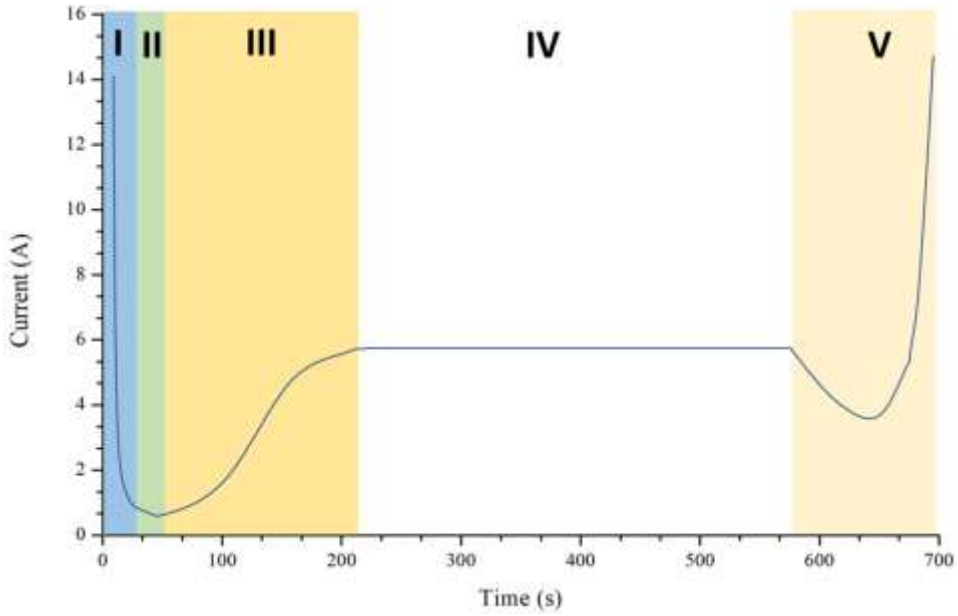

Figure 54. *Time–current curve*

These segments are linked to different reactions and equilibriums. First, we can state that there is a distinct decrease in the current density. During this phase (segment I), water and aluminum are split into ions:

$$H_2 \rightarrow 2H^+ + O^{2-} \quad (5)$$

$$H_2O \rightarrow H^+ + OH^- \quad (6)$$

$$Al \rightarrow Al^{3+} + 3e^- \quad (7)$$

The obtained O_2^- and OH^- anions react with aluminum at the metal/electrolyte interface and to form a layer of Al_2O_3. Thanks to the electric field, migration of the ions O_2^- and OH^- ions are enabled through the dielectric oxide layer allowing to oxidize the aluminum at the Al_2O_3/Al interface:

$$2Al^{3+} + 3O^{2-} \rightarrow 2Al_2O_3 \quad (8)$$

$$2Al^{3+} + 3OH^- \rightarrow Al_2O_3 + 3H^+ \quad (9)$$

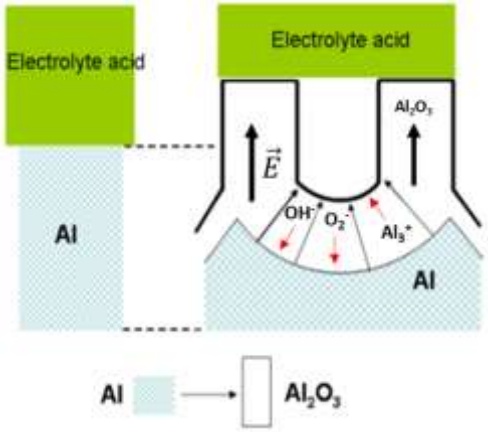

Figure 55. *Formation mechanism of AAO*

Simultaneously, Al cations migrate through the Al_2O_3 layer towards the Al_2O_3/electrolyte interface, in order to form the Al_2O_3. Both of the reactions reported are responsible in the growth of the dielectric Al_2O_3 layer that hinders for the ions to drift through it, causing by the occasion a decrease in the current density (segment II). Following this process, the current density starts to increase (segment III) as seen from Fig.54 due to the beginning of the dissolution of Al_2O_3:

$$Al_2O_3 + 6H^+ \rightarrow 2Al^{3+} + 3H_2O \qquad (10)$$

The increase in the current density cause a decrease in the oxide layer thickness. Because of fluctuations in the layer surface, the formation of pits is enhanced due to dissolution. Due to the presence of the oxide layer thickness at the bottom of each pit, the above-mentioned reactions happen faster at the pits, leading to pores formation. This increase is followed by a constant current density (segment IV), where the equilibrium is occurring between dissolution and formation of Al_2O_3 with pores growing vertically until they reach the underlayer. From there, the remaining aluminum between the pores is oxidized. Thus, forming a barrier layer of Al_2O_3 at the bottom of the pores that lead to a decrease in the current density. Still, after full oxidation of aluminum, the current density increases again, because at this point there is only dissolution of Al_2O_3, which leads to a decrease in the Al_2O_3 thickness. Finally, when the Ti inter-layer is reached, the same stage cited before are taking place but with a lower oxidation rate compared to the anodization of Al layer. This ensures a nice distribution of the AAO pores allowing them to reach the conductive Au layer, thus, the increase of the current (segment V).

After completion of the anodization process, a chemical widening process can be used on the pore's diameter labeled as D_{pore}, which would allow radius enlargement, smoothening of pore walls as well as barrier oxide layer dissolution (alumina layer between pore base and bottom electrode). Still the chemical widening method was found to linearly depend on time immersion time of the AAO membrane.[199,200] chemical etching process for pores widening process with controlled widening time has proven to be a very powerful technique that enables the simultaneous barrier layer dissolution, smoothing of pore walls and tuning of pore diameters.

1.1.2.1. Effect of Preparation Conditions on Anodic Aluminum Oxide (AAO) thickness's and pore size.

The particular electrolyte, its concentration, the anodic voltage and bath temperature are the main parameters in determining the pore size and the distance between pores.

Electrolyte

Typical electrolytes used to produce this type of oxide layer have a pH that is less than 5, and slowly dissolve the forming oxide layer. Examples of the acids used are sulfuric, phosphoric and oxalic. However; mixtures of organic and inorganic acids have also been used. The properties of the electrolyte are important in the formation of porosity and permeability. Electrolytes that are composed of less concentrated acids tend to produces oxide coatings that are harder, thicker, less porous and more wear resistant than those composed of higher concentrated acids. But the most important factor that must be considered when forming the porous oxide is the electrolyte ‘s ability to sustain a significant flow of Al^{3+} ions from the metal substrate into the electrolyte. There are two mechanisms that are responsible for the loss of Al^{3+} ions from the metal substrate. The first is by the direct expulsion of ions by the applied electrical field and the second is the dissolution of the forming oxide layer. In addition, if there are regions of high current flows when the electric field is applied, an increased dissolution rate can result (field assisted dissolution).[201]

Applied voltage

The applied potential V, is one of the most important factors to adjust self-assembly of porous alumina. The anodization voltage plays a crucial role influencing the pore diameter. In addition, the oxide layer at the bottom of pores could be controlled by changing the anodization voltages. During anodization at a constant DC voltage, the thickness of the barrier oxide layer remains constant, because the rate of alumina dissolution on the electrolyte side is equal to the rate of alumina production on the metal side. At lower voltage, the barrier oxide layer is quite thick; that led to small pore size and higher voltage led to large pore size because the barrier oxide layer is thin

Temperature effect

In order to know the effect of temperature on the pore size the temperature is kept constant during anodization of each AAO. It was noticed that the anodizing current increased with the temperature. During the anodization, temperature should be kept lower than room temperature to prevent the formed oxide structure from being dissolved in acidic electrolytes. A second reason to keep the temperature as low as possible is to avoid a local heating at the bottom of the pores during the course of anodization (specially, in the case of anodization at a high potential). The local heat causes an inhomogeneous electric field distribution at the bottom, leading to local electrical breakdown of the oxide. In fact, cracks and bursts of the oxide film are generated if porous alumina is formed without temperature controlling. If the temperature is too low (just

below zero degree) and diluted electrolytes are used, the electrolyte may freeze. In addition, the speed of the growth of porous alumina is affected by the temperature. The lower the temperature, the lower is the growth rate.

Experimental detailed of the preparation of AAO template.

The fabrication process of the supported AAO templates on a smooth conductive Ti/Au/Ti multilayer, deposited on top of a solid Si wafers is as follow: The aqueous solutions were prepared with deionized water. For the conditions used in the preparation, by applying an anodic potential of 56 V from a Keithley 2400 source meter during ~1000 sec, the as-prepared Al/Ti/Au/Ti/Si substrate was exposed to a single step anodization process in 0.2 M oxalic acid ($H_2C_2O_4$). The anodization process was stopped manually after the current gradually increased, identifying the end of the anodization process and indicating that the conductive gold layer has been reached by the template's pores (Fig. 56a). In order to improve the AAP template quality and to decrease the rate of oxidation process during anodization, the temperature was kept below <5°C. The anodization process was followed by a chemical widening of the nanopores and barrier layer dissolution in a 5 wt.% sulphuric acid (H_2SO_4) solution (Merch, Germany) at 30 °C for 45min (Fig. 56b). The SEM images of the AAO template after pore widening are shown in Fig.57a and Fig.57b respectively. The values for the inter-pore distance is D_{cell} ~100 nm, for the pore diameter is D_{pore} ~80 nm, and for the barrier layer thickness $t_{barrier}$ ~600nm.

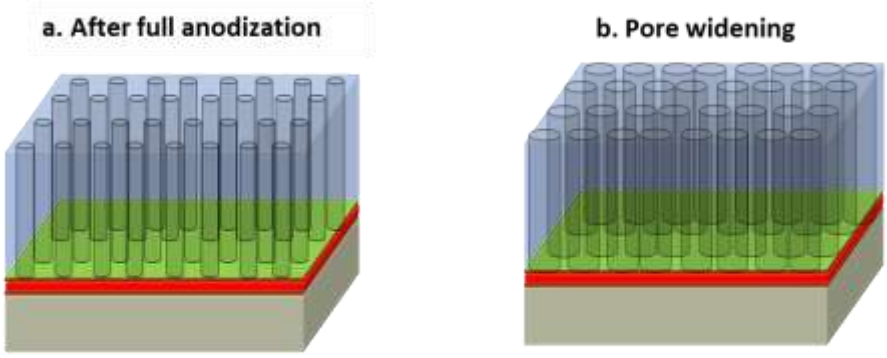

Figure 56. *Schematic illustration of the formation of porous alumina template. (a) Anodization of the Al/Ti bilayer, (b) Chemical dissolution of the barrier layer at the pore base and the pores chemical widening*

The Fig.57 shows the top and cross section view SEM images of the alumina templates after the anodization procedure and pores opening by means the preparation described in the section above.

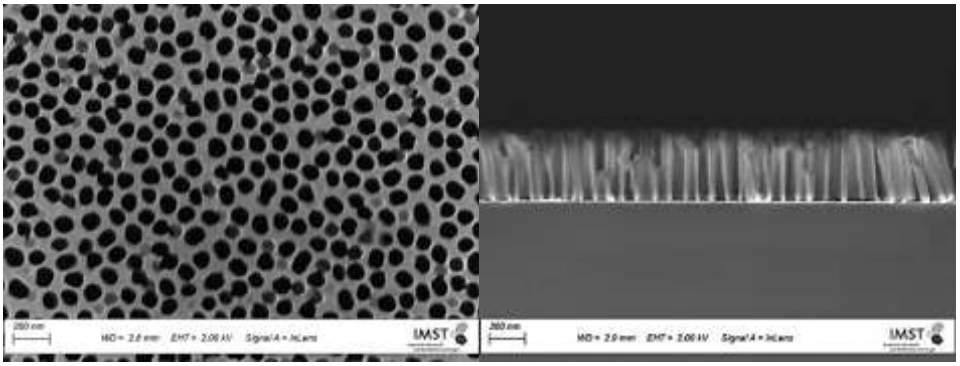

Figure 57. *Cross section view SEM images of the alumina templates after anodization*

1.1.3. Third Step: Electrochemical Deposition of Vertically Aligned $CoFe_2O_4$ nanorods Arrays into supported Anodic Alumina Templates:

A principle of magnetic nanorods electrodeposition is the confinement of metal ions inside the porous AAO membrane during their chemical reduction. The electrodeposition technique consists at applying a conductive path through the pores between the electrolyte contacting metal ions and the working electrode at the pore bottoms. A reduction of the metal ions diluted in the electrolyte are observed inside the nanopores through the conductive path by injection of an electrical current or a voltage. This low-cost technique was widely used for magnetic nanorods electrodeposition inside porous templates.[202] The fabrication technique used in the electrodeposition of nanorods allows to grow the high-density arrays (around 108-1011 NWs per cm^2). The geometric parameters of the grown nanorods (e.g. diameter, height and inter-spacing distance) are similar to the morphological features of the hosting AAO membrane. The templating method can be implemented using three main hosting materials, which are the block copolymer membrane, the polymer membrane, and the aluminum or silicon oxide membrane.

Iron deposition occurs simultaneously with hydrogen evolution; the occluded or absorbed hydrogen, leading to a rise in the embrittlement of the deposit, which can be partly removed by subsequent annealing processes. However, a small fraction of hydrogen tends to remain in the crystal lattice until nearly the melting point.[203]

The solutions used for the deposition of Fe-Co, Ni-Fe, and Fe-Co-Ni alloys are slightly acidic (pH ~2–3), and may contain either or both sulfates or chlorides of the various metals. Metal ion concentration is determined in part by the alloy composition sought for, and also by the fact that the Fe group metals exhibit the so-called anomalous co-deposition, i.e. the less noble metal in the alloy is deposited preferentially. In order to deposit Permalloy for example the concentration of Ni salt (0.5 M) is kept 50 times larger than the Fe ion concentration (0.01 M).

Buffering is needed in order to limit the pH increase at the interface resulting from the hydrogen evolution reaction; this is most often achieved by the use of boric acid (0.4 M).[142]

Experimental detailed of $CoFe_2$ nanorods fabrication.

In order to fabricate $CoFe_2$ nanorods, many electrolyte compositions were tested. It is worth mentioning that based on literature and electrolyte conditions, the results obtained were quite disappointing. However, by studying the stoichiometry of the cobalt ferrite $CoFe_2O_4$ compound it was clear that the amount of Fe is two times higher than Co. This information encouraged us to investigate the starting following conditions. For that matter, we used a standard three-electrode potentiostatic configuration by using a PAR263A Potentiostat/Galvanostat and a Pt foil as a counter electrode as depicted in Fig. 58. The three-electrode setup includes: (1) the Au-coated Si substrate at the bottom of the pores serving as a working electrode: (2) Pt foil as counter electrode. First electrolyte composition used was: $CoSO_4 \cdot H_2O$ (0.05M), $FeSO_4 \cdot 7H_2O$ (0.1M), by applying a potentiostatic voltage of 5V at room temperature with different electrodeposition durations: 30min, 10min, 4min, 2min respectively as shown in Fig. 59.

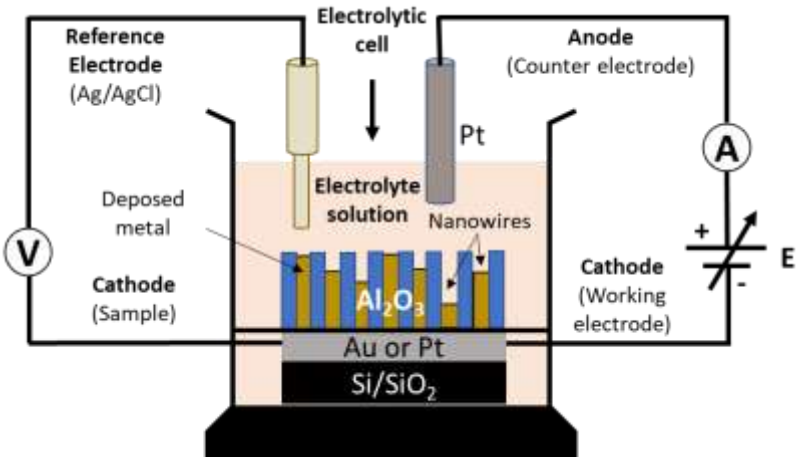

Figure 58. *Schematic of the "3-electrodes" potentiostatic electrochemical deposition setup*

According to the conditions above, as shown in Fig. 59a, Fig. 59b, for an electrodeposition duration of 30 min and 10 min, a very thick film deposited on top of the AAO with a non-homogenous deposition inside it. By decreasing the electrodeposition duration to 4min Fig. 59c, the deposition rate on the AAO surface decreases while a non-homogenous deposition was obtained. However, for the 2min Fig. 59d no deposition was observed on the surface of the AAO leading to almost empty pores. One of the main problems in Fe deposition, especially for magnetic device applications, is the possibility of oxidation of Fe^{2+} to Fe^{3+}, due to oxidation at the anode and/or to reaction with oxygen dissolved in the electrolyte. In combination with the

local increase in pH at the cathode due to hydrogen evolution, the presence of Fe^{3+} may lead to the precipitation of Fe(III) hydroxide, which is incorporated in the growing Fe films. The presence of Fe hydroxide results in embrittlement of the coating, which was the main problem in the first electrolyte composition.

(a)

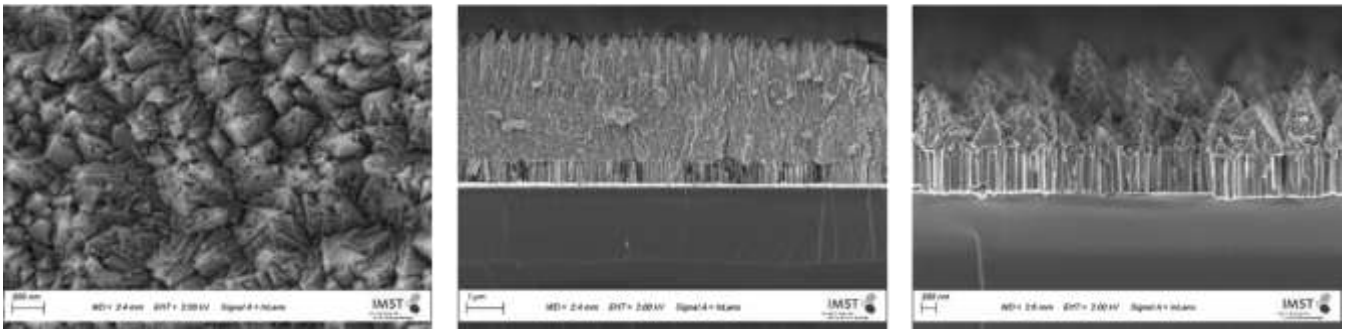

(b)

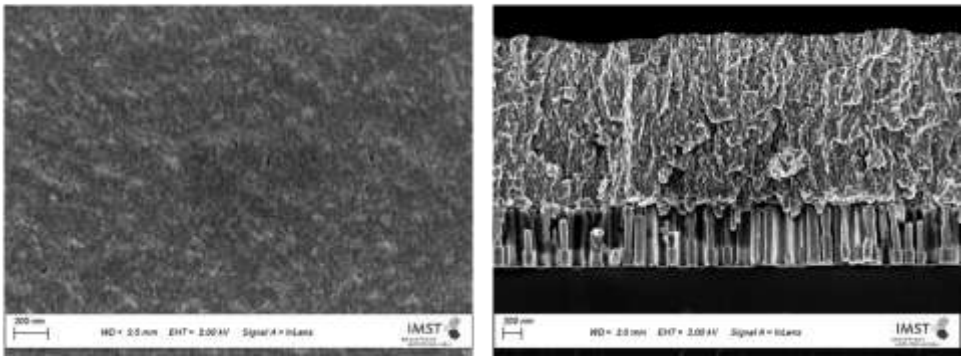

(c)

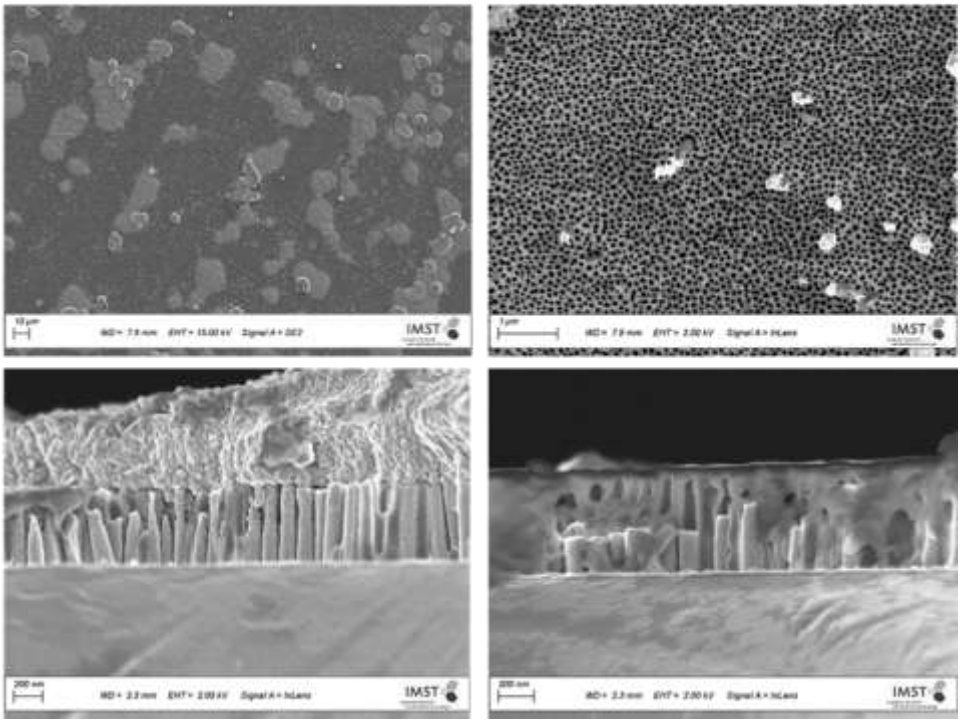

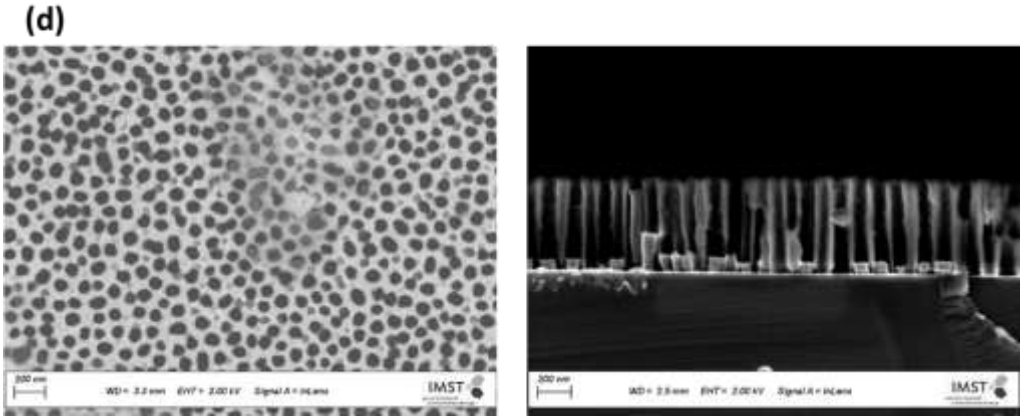

Figure 59. *SEM top view pictures as a function of electrodeposition time (a) 30min (b) 10min (c) 4 min (d) 2 min.*

To prevent the Fe(III) hydroxide formation and deposited on the top of the AAO. A decrease of the Fe ions concentration in the electrolyte was one of the proposed solutions. By trying a new electrolyte composition consisting $CoSO_4 \cdot H_2O$(0.05M), $FeSO_4 \cdot 7H_2O$ (0.025M), under applying the same potentiostatic voltage 5V at room temperature with different electrodeposition duration. As shown from the Fig. 60, it is very clear that in spite of decreasing the iron concentration the long electrodeposition duration to 10min and 5min respectively as shown in (Fig. 60a, 60b), lead to the precipitation of Fe(III) hydroxide. Hence, preventing the diffusion or the deposition of Co and Fe ions inside the pores. However, with decreasing the electrodeposition time to 180s and 160s we can see from Fig. 60c and Fig. 60d that the precipitation of Fe(III) hydroxide becomes low and the deposition looked homogeneous, but with short nanorods thickness of about 200nm.

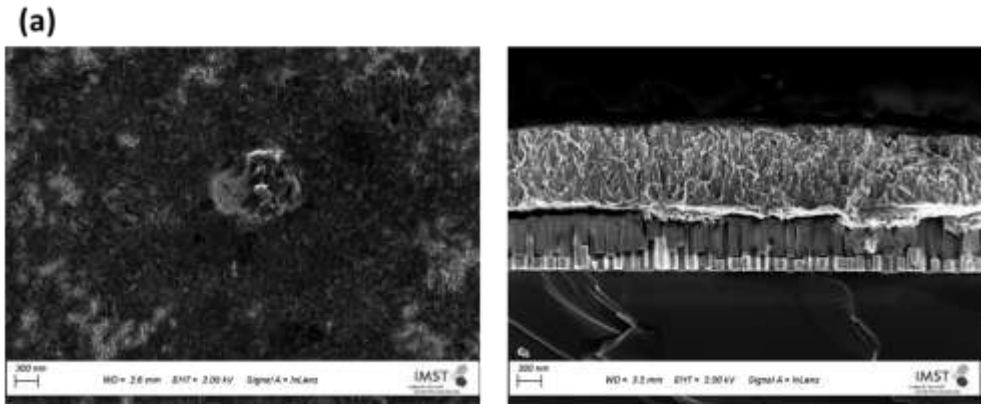

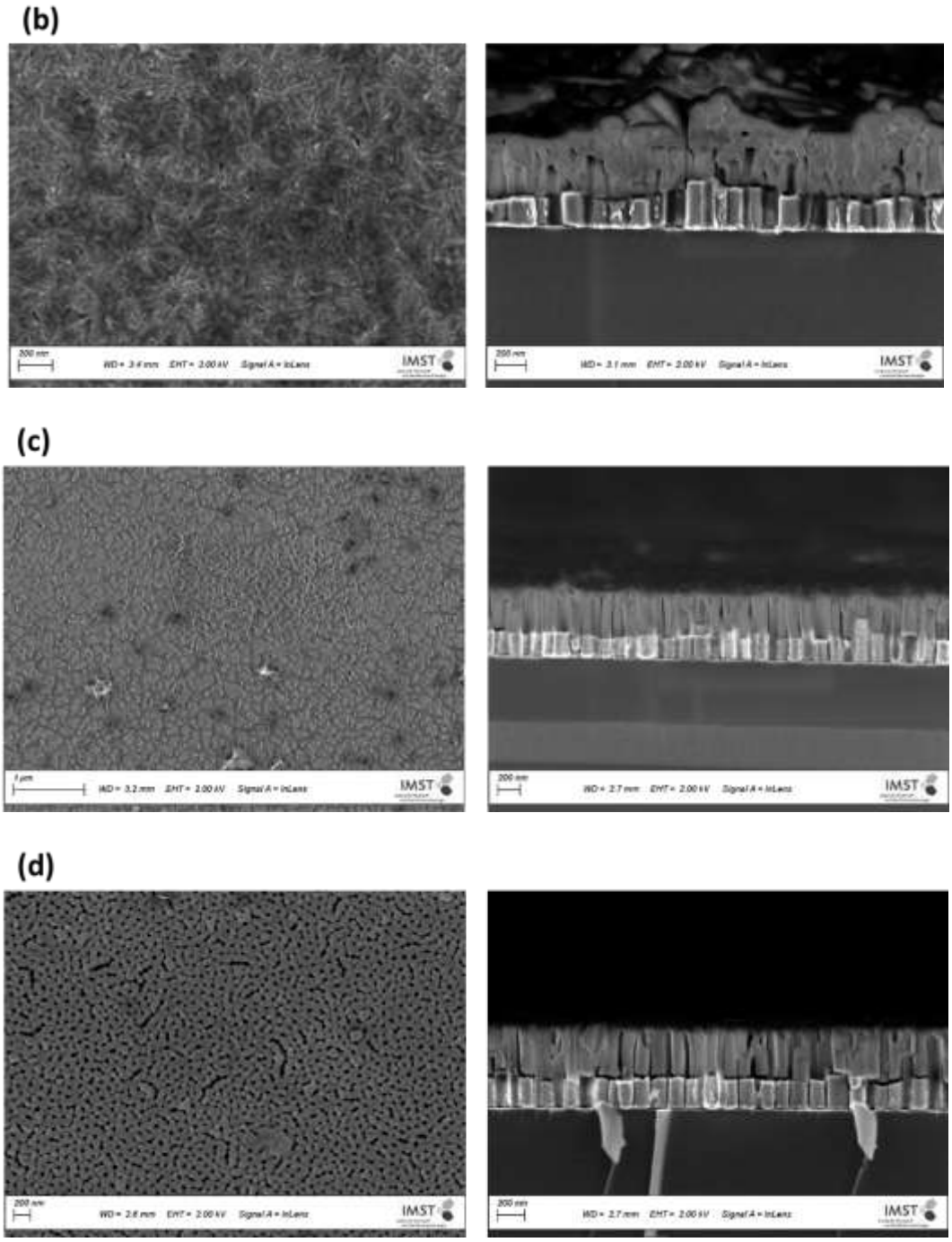

Figure 60. *SEM top view pictures as a function of electrodeposition time (a) 10(b) 5min (c) 180s (d)160s*

Optimal conditions:

In order to get a smooth deposition of $CoFe_2$ nanorods with longer thick

nesses and at short deposition time. Two main steps have to take them into account: by adding first the ascorbic acid. Thus, the presence of ascorbic acid served to minimize the air oxidation of iron (II) to iron (III) (prevent the Fe(III) hydroxide formation). The formation of iron (III) in the negative electrolyte must be avoided as it will reduce the Coulombic efficiency by electrochemical conversion to iron (II) and thus competing with the electrodeposition of iron.

second by buffering, which is needed in order to limit the pH increase at the interface resulting from the hydrogen evolution reaction; this is most often achieved by the use of boric acid .[142] Thus, the optimal electrolyte condition leading to smooth $CoFe_2$ nanorods are consisting $CoSO_4.H_2O$ (0.05M), $FeSO_4.7H_2O$ (0.025M),boric acid (0.4M),and ascorbic acid (0.025M),under applying a potentiostatic voltage of 5V at room temperature with short electrodeposition time of about 200s. as shown in the SEM images Fig.61, it is very clear that after employing the optimal condition cited above, we obtained a smooth surface without precipitation as shown in Fig. 61, the $CoFe_2$ nanorods have longer thicknesses in the order of the AAO thicknesses (approximatively 600nm) and diameter of about 80nm.

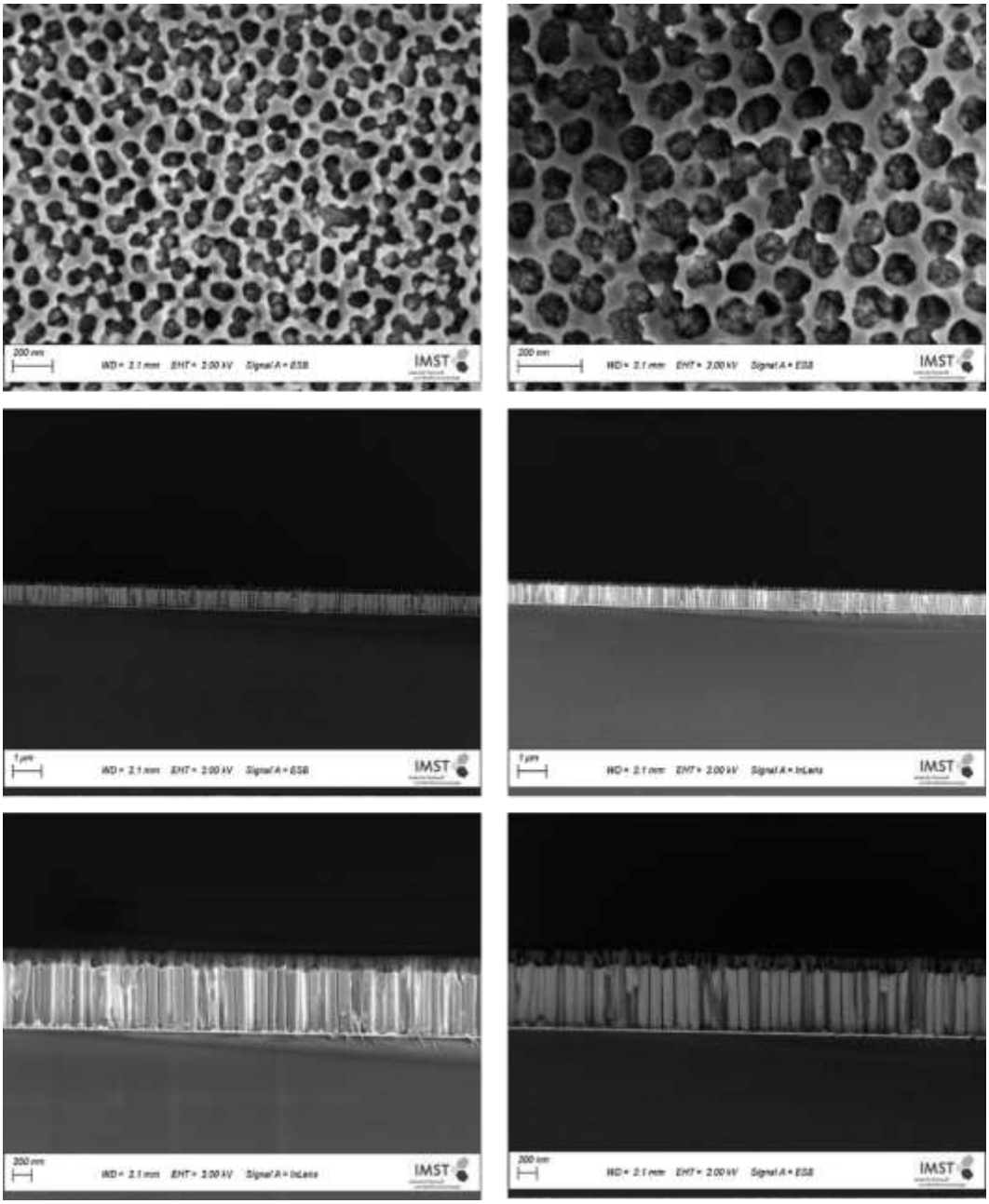

Figure 61. *Top and side view SEM images of fabricated $CoFe_2$ nanorods*

1.1.4. Fourth Step of Process: AAO Template Removal using Chemical Dissolution

The AAO template dissolution process is shown in Fig.62. Once the electrodeposition is completed, the alumina template was dissolved in a 3M of sodium hydroxide (NaOH) solution at room temperature during 1h as shown in Fig. 62.a and washed using distilled and (Fig. 62. b), thus leading to a free-standing and vertically aligned $CoFe_2$ nanopillar arrays Fig. 62.c.

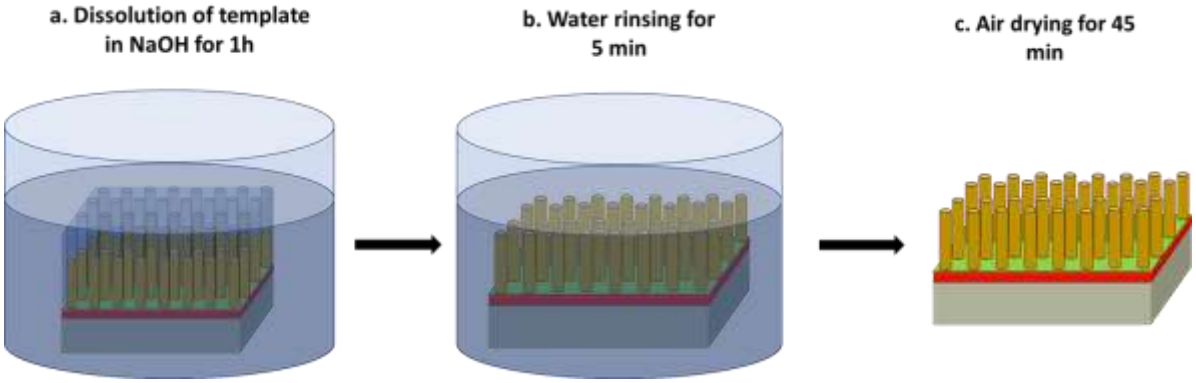

***Figure 62**. process of the chemical dissolution of the anodic alumina templates. a) Dissolution of the templates hosting CoFe2 nanorods arrays using 3M NaOH solutions for 1h. b) Washing of the free-standing CoFe2 nanorods arrays using the distilled water for 5 min. c) Drying of the $CoFe_2$* nanorods arrays in air for 45min

After totally removing the AAO template, a free standing and vertically aligned $CoFe_2$ nanorods are obtained as shown in Fig.63. the XRD measurement was investigated in order to confirm that the formed nanorods has a crystal phase correspond to $CoFe_2$, as can be seen in Fig.64, the patterns show that the main reflexes peaks correspond to $CoFe_2$ phase. However, a peak comes from the substrate (gold under-layer).

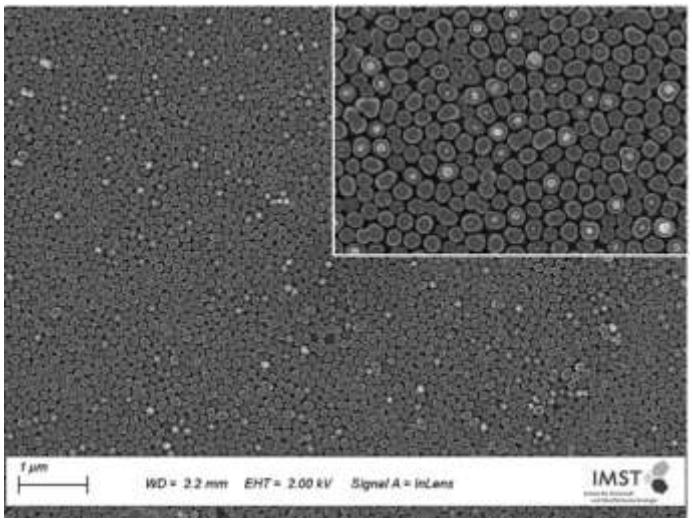

***Figure 63.** section view and top view SEM images of the $CoFe_2$ nanorods array after the template removal.*

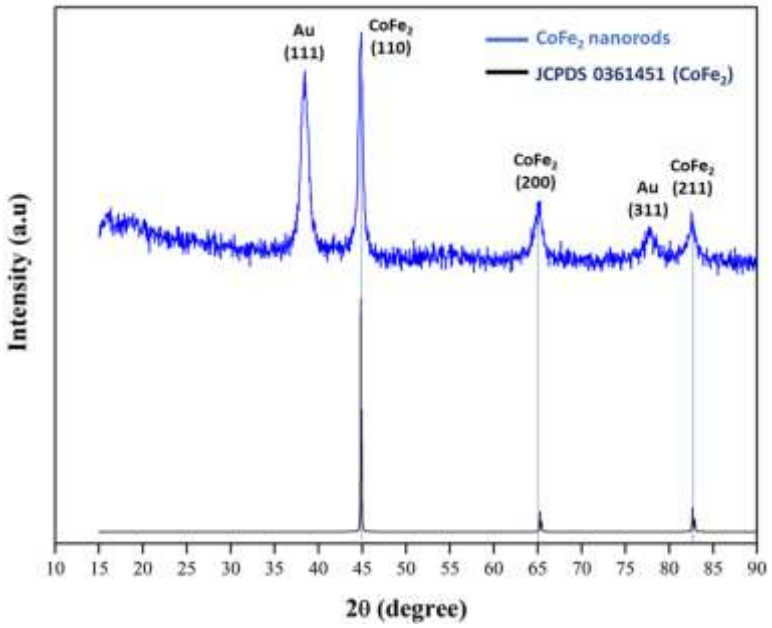

***Figure 64**. XRD pattern of $CoFe_2$ alloy*

1.1.5. Fifth Step of Process: Thermal Oxidation of $CoFe_2$ Nanorods Arrays

After the dissolution of AAO templates using the procedure shown in the previous part, the $CoFe_2$ nanorods arrays, free-standing on the Pt/Ti/Si substrate, were placed in a tubular furnace and heated in air at T_{anneal} = 500 °C for 24 hours in order to transform them into CoFe2O4 nanorods. Fig. 65 shows the top view SEM images of the $CoFe_2$ nanorods arrays after heat treatment, as seen in the Fig. 65, the nanorods shape distorted totally. However, the distorted $CoFe_2$ nanorods were transformed to a thick film with large grains of $CoFe_2O_4$ phase as shown in the XRD measurement Fig. 66. It is worth noting that, in order to solve the distorted problem, many heating treatments were investigated, we can cite: Heat treatment at T_{anneal}=600°C for 12 hours and 6 hours and heating at T_{anneal} = 400°C for the same period time. However, the $CoFe_2$ nanorods are distorted and transformed to $CoFe_2O_4$ phase. The second treatment consisted of annealing at T_{anneal} = 100°C and 200°C for 1 week and 2 days respectively. Nevertheless, the nanorods shape were preserved, without transforming to $CoFe_2O_4$ phase. The third treatment consists of annealing the $CoFe_2$ nanorods inside the alumina matrix (AAO), at $T_{anneal} \geq$ 500 °C resulted in some fading of the black color of alumina, and these changes intensified with further increase of *T*ann. A typical Mössbauer spectrum of the nanowires arrays with nanowires diameter of 30 nm after annealing at 600 °C revealed the complete transformation of the Fe into two components, i.e. $FeAl_2O_4$ and $(Fe_xAl_{1-x})_2O_3$.[204] Thermal oxidation of free-standing $CoFe_2$ nanorods arrays leading to the thermal expansion and corresponding variation of nanorods diameter, morphology, surface roughness, and deformation. On one hand ,nanorods

with large diameters (D = 90nm) enhancing the collapsing process of the $CoFe_2$ nanorods, and then leading to distorted phenomena, on the other hand the diffusion of Au underlayer on the nanorods could be the main problem of the nanorods distortion.

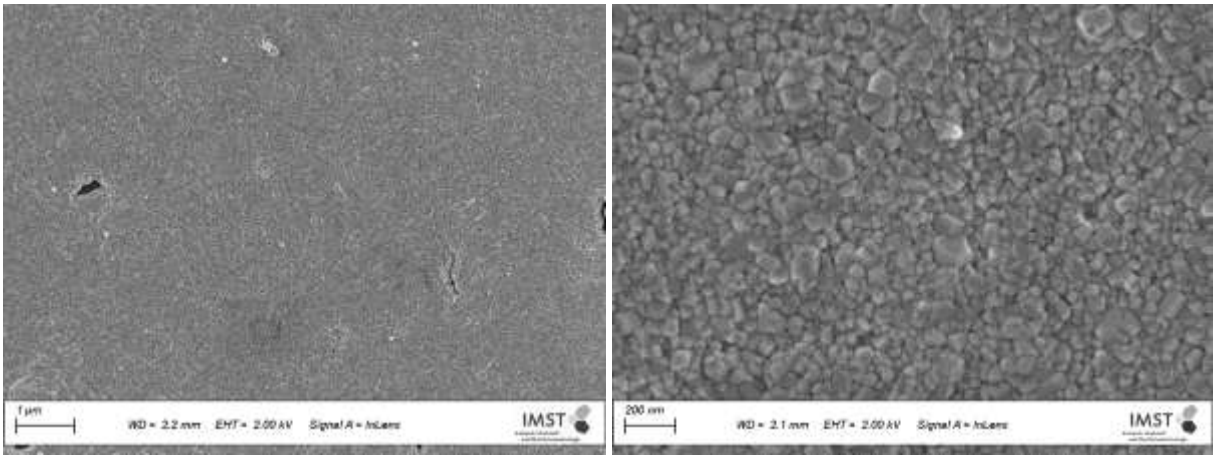

***Figure 65**. SEM of $CoFe_2O_4$ annealed at 600°C for 24h*

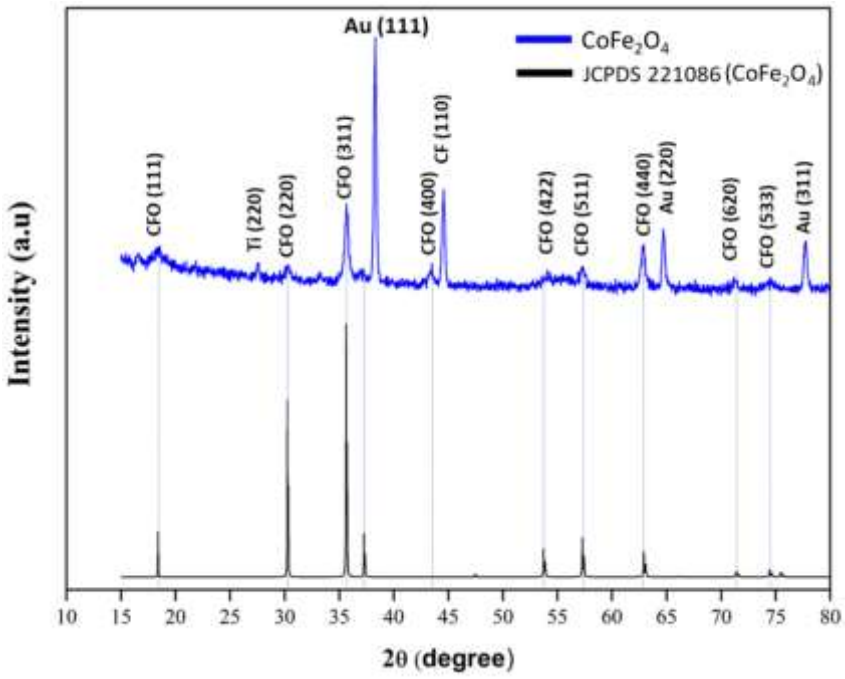

Figure 66. XRD of $CoFe_2O_4$ annealed at 600°C for 24h

Conclusion

In this part of the thesis, we focused on the process of fabricating vertically aligned $CoFe_2O_4$ nanorods arrays into supported anodic alumina templates by using electrochemical deposition method. After testing many electrolyte compositions, we succeeded in the fabrication of the $CoFe_2$ nanorods. The latter have longer thickness in the order of the AAO thicknesses (approximately 600nm) and diameter of about 80nm. However, based on literature and on our experimental conditions, the $CoFe_2$ nanorods seemed to become distorted and transformed into

a thick film layer of $CoFe_2O_4$. Unfortunately, we failed to preserve the ordered nanorods structure after thermal oxidation.

2. Simple synthesis of $CoFe_2O_4$ nanoporous oxide layer by electrochemical anodization

In the present work, we aim at fabricating a new form of $CoFe_2O_4$ nanostructures consisting on self-ordered $CoFe_2O_4$ nanoporous oxide layer via electrochemical anodization of FeCoV alloy metal sheet. The benefits of the electrochemical anodization method are the cheap and most straightforward approach to obtain ordered nanostructures under the right conditions. This method allowed us to get a new nano-structural form of $CoFe_2O_4$. The synthesized $CoFe_2O_4$ nanoporous oxide layer may be used for several magnetic applications. Self-ordering of anodized porous structures is known since the pioneering work of Masuda and Fukuda who were able to grow a highly ordered porous alumina structures, through establishing an equilibrium between the formation and dissolution of the oxide layer during the anodization of aluminum in acidic electrolyte.[205] Later, the process (with some necessary modifications) has been applied to numerous other metals, such as Ti, W, Zr, Nb and V, as well as many alloys.[206,207,208,209,210] Many studies were done in order to synthesize Fe nanopores and nanotubes, among them we can cite Albu et al. who reported on the processing of high aspect ratio, self-ordered iron oxide NTs by anodization of Fe in ethylene glycol/NH_4F electrolytes.[211] Furthermore, lee et Al. reported the formation of a highly ordered cobalt oxide nanoporous layer synthesized by mean of electrochemical anodization and they found that it has potential application as a catalyst-electrode.[212] However, until now, and to the best of our knowledge, no work has been published so far on the fabrication of self-ordered nanoporous $CoFe_2O_4$ via electrochemical anodization of the parent alloy. In this thesis, and for the first time we shed light on the process of fabricating $CoFe_2O_4$ nanoporous oxide layer by anodizing a commercial rolled sheet of a FeCoV alloy. We will show how the process parameters affect the porous structure, and the post processing treatment of the $CoFeO_4$ stoichiometry and properties. Finally, the magnetic properties of $CoFe_2O_4$ nanoporous oxide layer have been studied as a function of external applied magnetic field direction and thickness.

2.1. Experimental section:

2.1.1. Fabrication of $CoFe_2O_4$ nanoporous oxide layer

The rolled sheet of FeCoV alloy (sample 1) with specified composition in weight%: 49 % Fe, 49 % Co, 2% V, and 0.1 mm thickness) was obtained from VACOFLUX (Germany). FeCoV alloy sheets were cut into 2 × 1 cm pieces, which were ultrasonically cleaned in ethanol (99%) for 5 min and subsequently dried in a stream of dry air. The electrochemical anodization experiments were performed under potentiostatic conditions by using electrochemical workstation (Keithley 2400 SM, USA) in a two-electrode configuration with a counter electrode made of platinum sheet metal as shown in Fig. 67. During the anodization process, the temperature was kept below 10°C using an ice bath. Different electrolytes compositions were explored using ethylene glycol (EG) glycerol (Gly) and mixtures of EG-Gly solutions with varying concentrations of NH_4F and H_2O. Glycerin (99.5%) and ethylene glycol (99.5%) were purchased from Chemdiscount (Germany), while ammonium fluoride (>98%) from Carl ROTH (Germany).

The optimal anodization parameters and electrolyte composition have been used for growing nanoporous layer for different anodization time (90min, 3h, and 6h). The as-anodized samples were immediately rinsed with ethanol and dried in air. For transforming the as-anodized nanoporous oxide layer to a fully crystalline nanoporous oxide layer $CoFe_2O_4$, the samples were annealed at 450°C for 90 minutes in air.

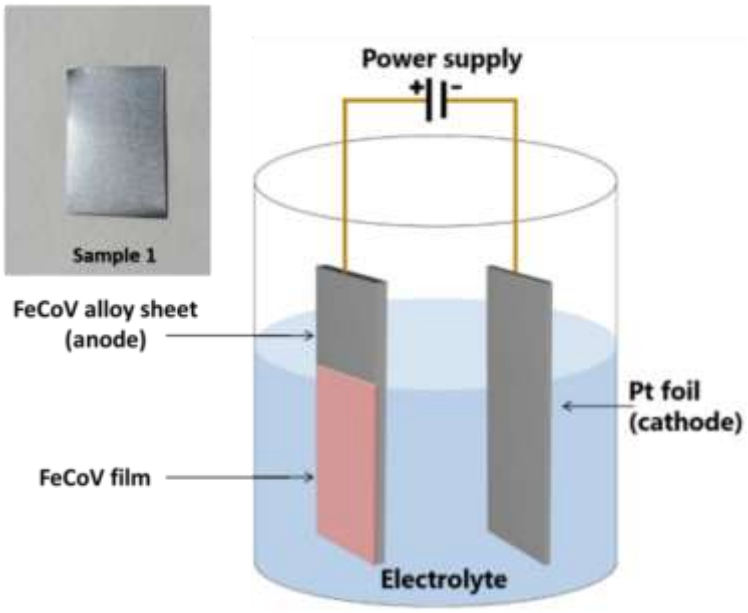

Figure 67. *Scheme representing an electrochemical cell used to produce FeCoV nanoporous layers by anodization of FeCoV alloy sheet.*

2.2. Results and discussion

2.2.1 Processing, morphology, mechanism and structure of anodic $CoFe_2O_4$ layers

In the following, we first give a succinct account of our endeavor to obtain a self-ordered porous structure on the FeCoV alloy sheet. We found that the formation of the nanoporous oxide layer was very sensitive to the anodization conditions and electrolyte compositions. We first started with the electrolyte compositions proposed by Albu et al. [22] and lee et al. [23] for anodizing Fe and Co respectively and applied them to our alloy. The results were, however, not satisfactory in terms of pore formation and ordering. A screening of the relevant parameters like electrolyte composition, anodization temperature, anodization voltage, and anodization time followed. Different electrolyte compositions were tested at constant voltage and temperature. Additionally, various fluoride and water concentrations were investigated in order to enable the equilibrium between the formation and the dissolution of the oxide layer, i.e. to obtain a self-ordered porous structure.

In the following sections, we will investigate the effect of electrolyte compositions and anodization conditions on the morphology, pore diameter, and oxide layers thickness such as the electrolyte solution, temperature, water and ammonium fluoride concentrations, anodization voltage, and anodization time.

2.2.1.1 Effect of electrolyte solution and temperature

By anodizing CoFeV alloy at room temperature, using ethylene glycol and the optimized amount of water and ammonium fluoride concentrations (0.15M H_2O and 0.15M NH_4F), under an applied voltage of 50V, we observed the formation of a very thick and compact layer, which is undesirable. The main cause of this thick formation is the anodization at room temperature which leads to a rapid evolution of oxygen which induces heat in the anodic layer.**Erreur ! Signet non défini.** To prevent this problem, all the following anodization experiments were performed at low temperature T<10°C. However, we still found that ethylene glycol as a solvent led to a compact layer with highly disordered pits with different pores diameter and a rough wall surface. This suggests that the low temperature is not the only parameter that needs optimization. To remediate to the disorder of the nanopores, we added Glycerin solvent, known to increase the viscosity and decrease the electrolyte conductivity, thus promoting the formation of ordered porous structures.[213] For further optimization, a mixture of ethylene glycol and Glycerin was used whereupon we observed that by increasing the ratio of Glycerin to 80%, the nanoporous layer becomes more ordered.

The optimum conditions thus found are an electrolyte composition of (in V %) 80% Glycerol, 20% EG, containing 0.15 M ammonium fluoride and 0.15M H_2O for a T<10°C, and a potentiostatic voltage of 50V and an anodization time of 90 minutes. Under this optimum condition, the nanoporous layer became more ordered and smoother. Fig. 68 is a top-view SEM micrograph depicting the morphology of the nanoporous anodized layer.

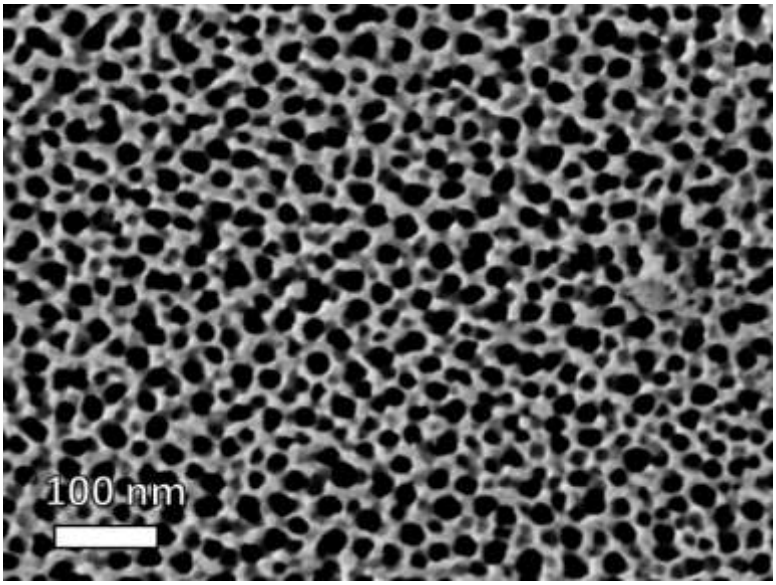

Figure 68. *Top view of SEM image of the synthesized nanoporous oxide layer formed under optimized electrolyte composition (80% in volume of glycerol and 20% in volume of ethylene glycol containing 0.15M ammonium fluoride and 0.15M of H_2O) and anodization condition at 50V, T<10°C for 90 min*

2.2.1.2 Effect of water concentrations

The water amount is essentially important in determining the rate of the growth of the layer, as the thicker porous layer can be grown. However, an excessive water content will lead to the appearance of rough and rippled walls.

By using the optimum conditions mentioned above with different water concentration consisting of 0.3M H_2O and 0.5M H_2OM respectively. Figure. 69 shows the effect of increasing water amount on the nanopores morphology and ordering. It is very clear that by increasing the water concentration to 0.3M H_2O and 0.5M H_2O respectively as shown in Fig.69a and Fig.69b respectively the oxygen evolution increase largely, and then increasing the oxidation rate with comparison to the dissolution rate , leading to the formation of a thick oxide layers with highly disordered pores .

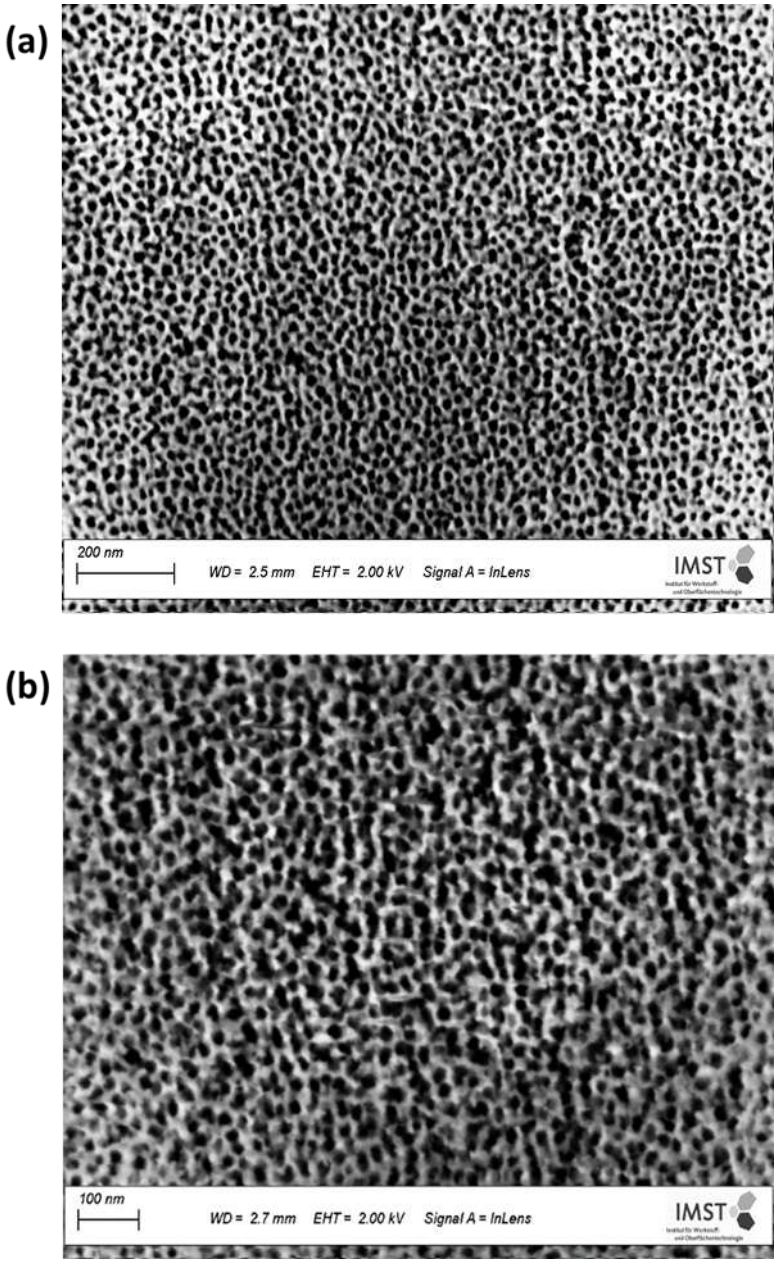

Figure 69. *Top view of SEM image of the synthesized nanoporous oxide layer formed under 80% in volume of glycerol and 20% in volume of ethylene glycol containing 0.15M ammonium fluoride, anodization condition at 50V, T<10°C for 90 min and water concentration of (a) 0.3M and (b) 0.5M*

2.2.1.3 Effect of ammonium fluoride (NH_4F) concentrations

Fluorides ions F^- participate in the chemical dissolution reaction with negligible amount of them being deposited on the surface of nanopores. However, most of them form complex species in electrolytes. The presence of fluoride ions is a key factor to activate the pore drilling, which give rise to the formation of highly ordered nanoporous structure.

At a NH_4F content of 0.15M an ordered porous FeCoV film is obtained. This result is attributed to the fact that chemical dissolution rate occurs uniformly to form nanopores under low F^-

content as shown in Fig.68. With increasing concentration of NH_4F to 0.3M and 0.4M respectively, the dissolution reaction increases, leading to the formation of highly disordered pits for the concentration of 0.3M NH_4F as seen in Fig. 70a Nevertheless, for the high concentration of 0.4M NH_4F, the complex species formed by F^- and the metals ions Co^{2+}, $Fe2^+/Fe^{3+}$ tend to precipitate on the surface of the FeCoV nanoporous layers (Fig.70b).

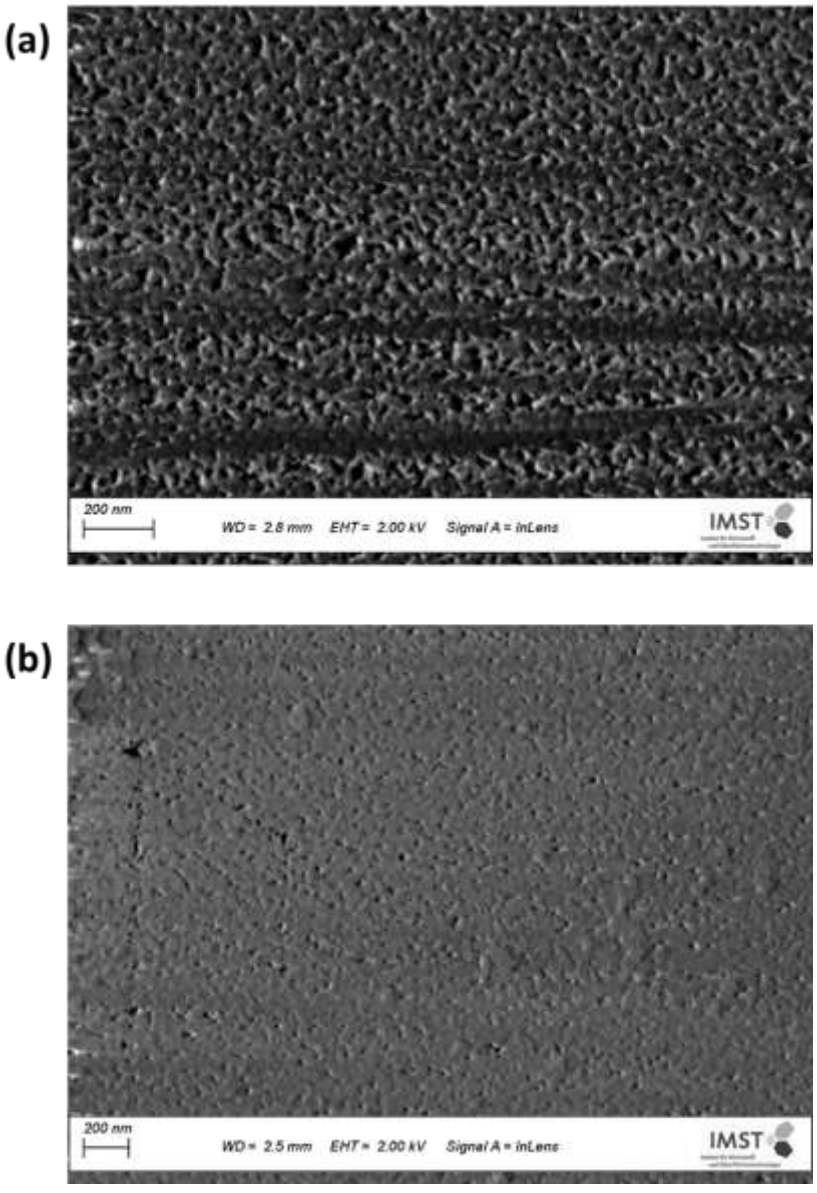

Figure 70. *Top view of SEM image of the synthesized nanoporous oxide layer formed under 80% in volume of glycerol and 20% in volume of ethylene glycol containing 0.15M of water, anodization condition at 50V, T<10°C for 90 min and ammonium fluoride concentration of (a) 0.3M and (b) 0.4M*

2.2.1.4 Effect of anodization voltage

The applied voltage is found to be an important factor that determines the pore diameter. To investigate the effect of applied voltages on pore morphology and its diameter, voltages of 50V, 70V, and 90V were applied respectively for anodizing FeCoV alloy sheet. As shown in Fig. 71

representing the current density-time curve. The typical behavior during anodization with an initial exponential current drop is due to the oxide formation and a subsequent steady-state regime through which the pores form correspond to the applied voltage of 50V as seen in Fig. 71.a. However, for the voltages of 70V and 90V as depicted in fig 71.b and c we observed another current drop instead of a steady-state regime, which could be explained by an increase in oxidation rate compared to the dissolution rate. The setback is that ordered structures can only be obtained over a special potential which is 50V. On the other hand, we found that the pore diameter did not change when the voltage increases, remaining roughly constant at d=15nm.

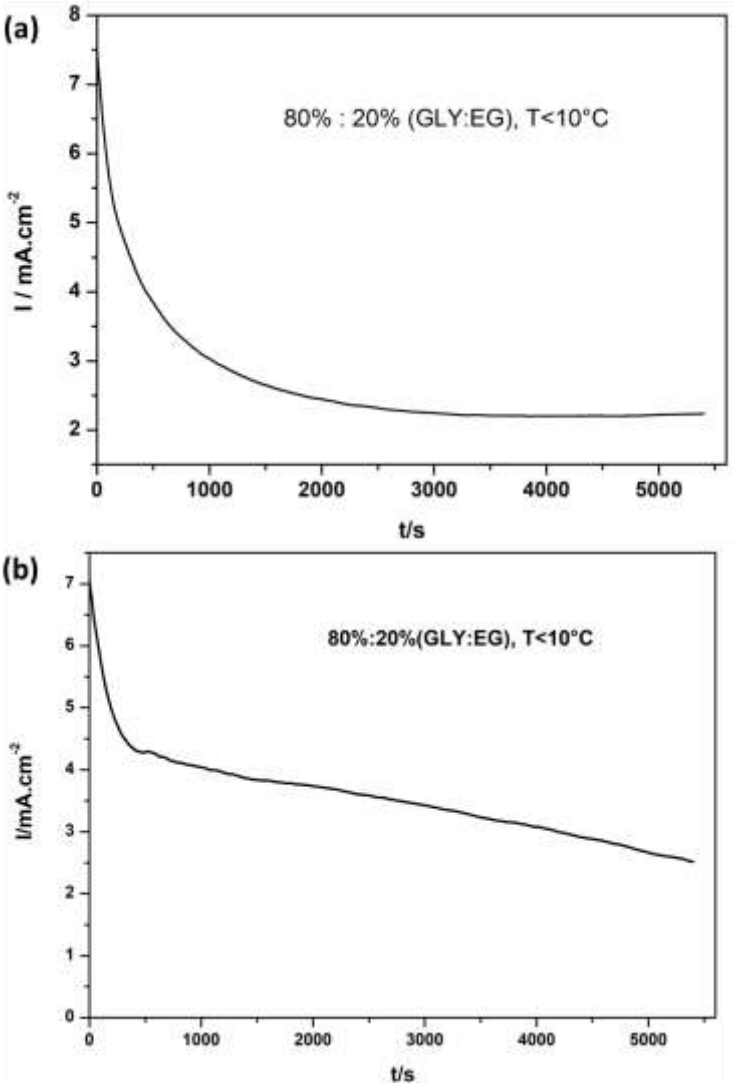

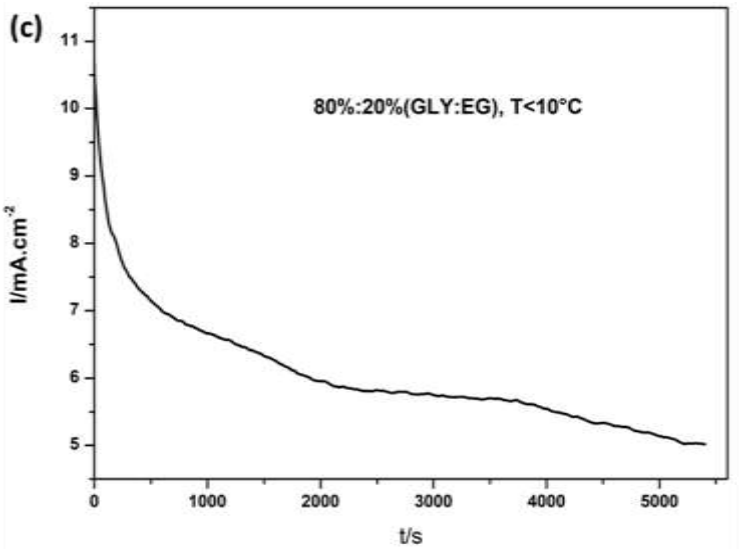

Figure 71. *Anodization current-time behavior of the formed nanoporous oxide layer under optimized electrolyte composition (80% in volume of glycerol and 20% in volume of ethylene glycol containing 0.15M ammonium fluoride and 0.15M of H2O) and anodization condition of T<10°C for 90 min and a voltage of (a) 50V, (b) 70V and 90V.*

2.2.1.5 Effect of anodization time

The thickness of the porous layer can be tuned by varying the anodization time from few hundreds of nanometers to several micrometers, as shown in Fig. 72. With increasing the anodization time to 90min, 3h, and 6h respectively, the thickness increases linearly to 990nm, 1500nm, and 3300nm respectively.

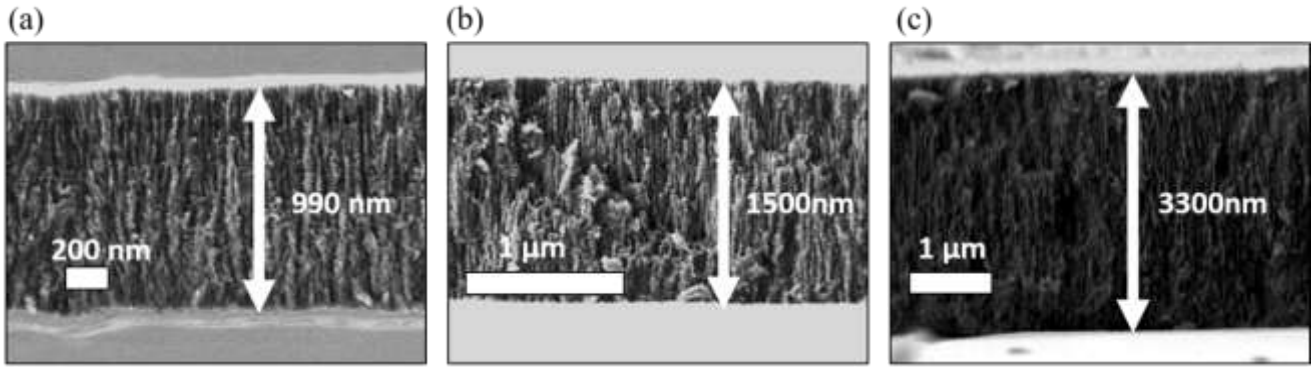

Figure 72. *Cross-section view of the SEM secondary electron (SE) images of the formed nanoporous oxide layer anodically fabricated in the same optimized conditions for different anodization time at (a) 90min (b) 3h (c) 6h.*

2.2.2 The mechanism of formation of $CoFe_2O_4$ nanoporous oxide layer

The mechanism of formation of $CoFe_2O_4$ nanoporous oxide layer on FeCoV alloy sheet is described by two main processes: growth of an anodic oxide layer and the chemical dissolution of the oxide layer by forming nanopores in a fluoride free electrolyte. An anodic oxide layer was produced on the anodized FeCoV alloy sheet surface in a fluoride free electrolyte, through the reaction between the oxidized metal species (Fe^{2+}/Fe^{3+}, Co^{2+}) and H_2O (O^{2-}). Under constant

applied voltage, a dielectric breakdown of the oxide layer is produced leading to a chemical etching of the oxide due to the presence of the fluoride ion F^-. During the chemical etching, the existence of water in the electrolyte helps the dissolution of the oxide layer by forming an aquo-complex. The latter process led to the formation of small pits. More migration of F^- ions into the surface sheet kept the charge neutrality with H^+ ions, this process assists the dissolution of the barrier layer. On the other hand, the FeCoV alloy sheet continues oxidizing because of the presence of O^{2-} and the applied anodic potential. Hence, the high concentration of F^- and H^+ within pits leads to rapid dissolution of the growing oxide, thus the formation and growth of pores.

2.2.3 Annealing treatment of the anodized FeCoV alloy sheet

After anodizing the FeCoV alloy sheet, an annealed treatment in air was performed, to transform the as-anodized nanoporous oxide layer into nanoporous cobalt ferrite $CoFe_2O_4$ spinel phase. Different annealing temperatures were tested 300°C, 350 °C, 400°C, 450°C, 500°C for 90min.

The nanopores morphology of the annealed samples at a temperature $\leq$ 450°C were not affected, as they yielded ordered and smoother nanopores. However, for samples annealed at 500°C, the nanopores were totally destroyed and transformed into a thick film composed of large grains. It is worth noting that at a high annealing temperature, the growth of large grains is unavoidable, which could be explained by the diffusion of cobalt and iron ions from the metal sheet alloy to the surface, leading to the growth of very big grains. To obtain an information about the formed structures, XRD measurements were performed on samples annealed at temperatures $\leq$ 450°C. The samples annealed at 300°C, 350°C and 400°C showed an amorphous phase. In addition, the main peaks are arising from the substrate $CoFe_2$ and Fe_3O_4, with weak peaks coming from the contribution of $CoFe_2O_4$. However, we found that the optimal annealing temperature leading to the formation of nanoporous oxide layer $CoFe_2O_4$ spinel phase was 450°C as shown in Fig. 73.

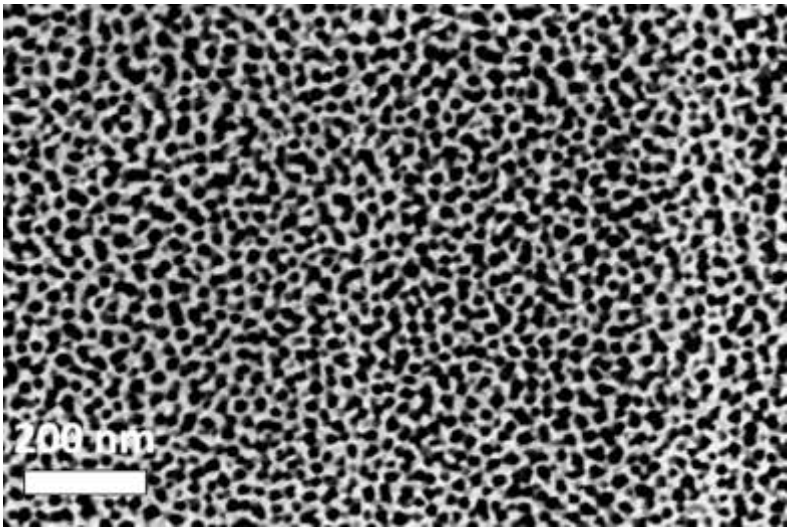

Figure 73. *SEM image of the annealed $CoFe_2O_4$ nanoporous oxide layers for 90min at T=450°*

2.2.4. EDS measurements

The EDS spectra of the as-anodized layer (sample 2) along with the anodized and heat-treated at 450°C (sample 3) are presented in Fig. 74. We found that the as-anodized layer contains fluorides, which are incorporated into the pore walls and the barrier layer during anodization as seen in Fig. 74a. While for the heat-treated sample shown in Fig. 74b, we found that it's devoid of fluoride, and contains instead a high concentration of oxygen. Because of the substrate contribution to the EDS signal, it is not possible to give semi-quantitative results

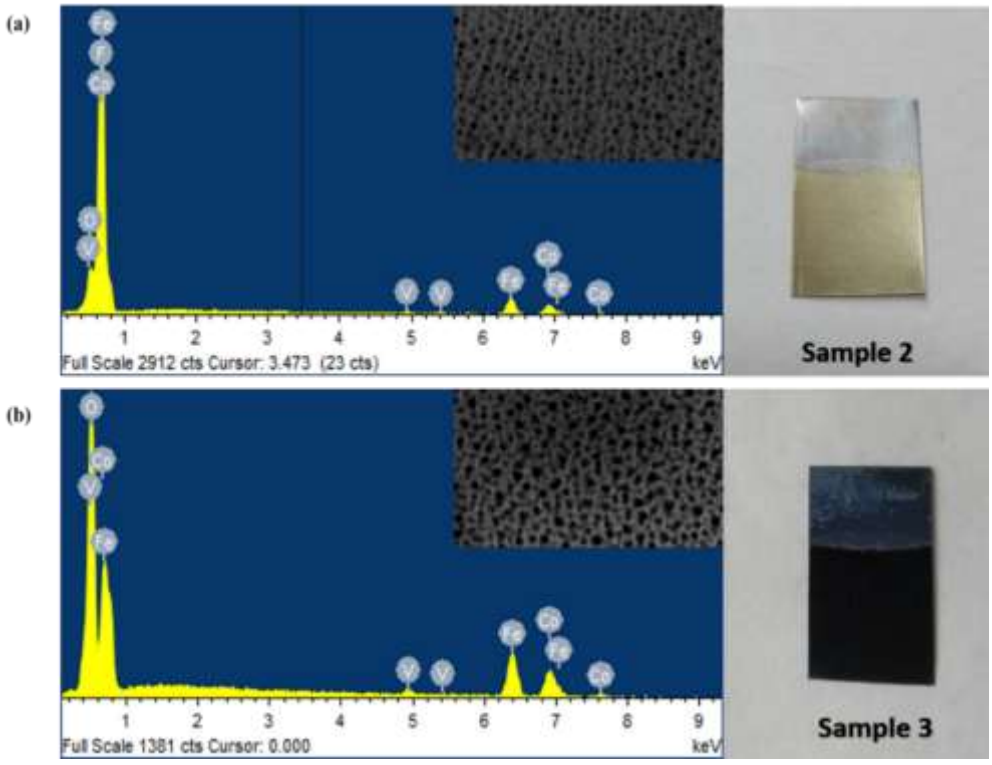

Figure 74. *EDS spectra of (a) the as-anodized nanoporous oxide layer (b) After heat-treatment for 90min at T =450°C*

2.2.5. XRD measurements

The XRD patterns of the anodized and heat-treated sample is represented by the red color as shown in Fig.75 in comparison to a control sample consisting solely of the FeCoV alloy sheet that was heat-treated under the same conditions at T=450°C for 90min (sample 4) represented by the black color. Both patterns show main reflexes of $CoFe_2O_4$ together with weak reflexes of the substrate as shown in Fig.75. One weak reflex is attributed to Fe_3O_4, although this assignment cannot be ascertained, because the main reflexes of Fe_3O_4 are absent. Thus, we could say that both the heat-treated FeCoV alloy sheet corresponds to $CoFe_2O_4$ sheet (black pattern), and the anodized and heat-treated sample corresponds to $CoFe_2O_4$ nanoporous oxide layer (red pattern). It can be seen that the latter exhibits broader and smaller peaks which points to the formation of nanocrystalline phase. The crystallite size calculated using Scherer's formula are equal to 12.4 nm for the plain film and 8.9 nm for the nanoporous oxide layer.

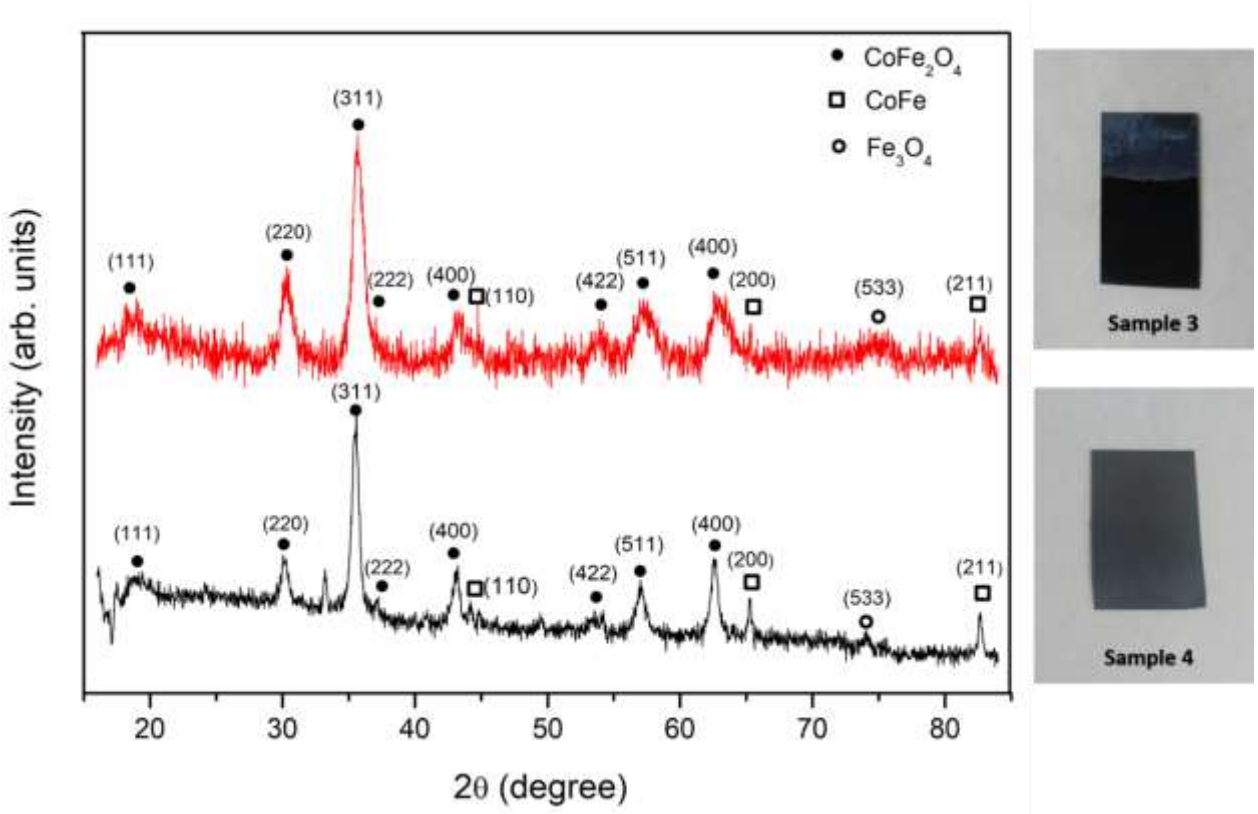

Figure 75. *XRD patterns of $CoFe_2O_4$ sheet (black) and $CoFe_2O_4$ nanoporous oxide layer (red)*

2.2. Magnetic properties of $CoFe_2O_4$ nanoporous oxide layer

Magnetic properties of FeCoV alloy sheet, $CoFe_2O_4$ sheet, and $CoFe_2O_4$ nanoporous oxide layer were measured at room temperature (T=300K). Cutting and placing the samples on the

holder were done manually. Fig. 76 shows the hysteresis loops of the three samples. FeCoV alloy sheet (sample 1) and $CoFe_2O_4$ sheet (sample 4) were used for the sake of comparison with the magnetic properties of $CoFe_2O_4$ nanoporous oxide layer (sample 3). The latter exhibit different thicknesses ranging from 990, 1500, and 3300 nm respectively. The hysteresis loops were measured along the in-plane (Fig.76a) and out-of-plane directions (Fig.76b) of the external magnetic field. The saturation magnetizations (M_s) and coercive fields (H_c) are summarized in Table 6.

It is of interest to mention that the FeCoV alloy sheet is available in the form of cold-rolled sheet, which is characterized by a rolling texture, known to cause a high magnetic anisotropy, which affect strongly the magnetic properties. As demonstrated by Chang He Shang et al., the rolling texture influence largely the magnetic and mechanical properties of FeCoV alloy sheet.[214] The rolled textured sheets are characterized by three directions: The Rolling Direction (RD), Transverse Direction (TD) and the Normal Direction (ND). The RD and TD directions are in the plane of the surface sheet. However, the ND is out of plane of the surface sheet. Based on Chang He Shang et al. studies, we investigated the magnetic properties of our samples by applying a magnetic field along in-plane direction at different angles with respect to the RD (θ=0°). A difference was noticed between the hysteresis loops measured along different directions of the sheet plane. Among all the measurements, the highest value of magnetization for different angles occurs at θ=90° as shown in Fig 76a, which means that the easy direction for the magnetic properties is perpendicular to the RD and hence along the TD. On the other hand, a magnetic field have been applied along the out of plane direction (along the ND) as shown in Fig 76b. It is clear that the shape of these loops differs significantly from the well-known shape of the hysteresis loops (Fig 76a) along the in-plane direction. The measured samples showed a high magnetic anisotropy affecting largely the magnetic properties with respect to the applied magnetic field direction as can be seen in table. 6. Indeed, the samples have a preferential magnetic orientation along the rolling texture. Therefore, the TD is the easy axis, and the ND is the hard axis.

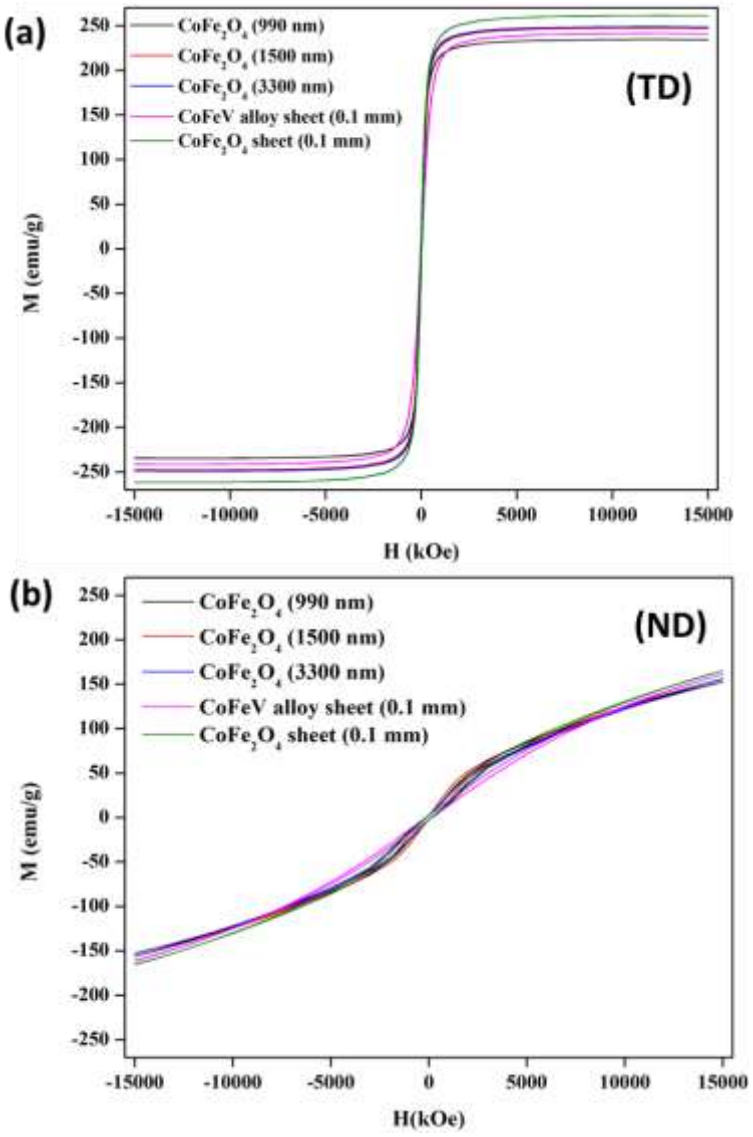

Figure 76. *Hysteresis loops of the samples along the (a) in plane and (b) out-of-plane direction*

For the magnetic properties of the samples as a function of thickness. FeCoV sheet, $CoFe_2O_4$ sheet and $CoFe_2O_4$ nanoporous oxide layer with thicknesses ranging from 990nm, and 3300nm respectively and a constant nanopores diameter of approximately 15 nm. From table 6, it is worth noting that the magnetic properties of FeCoV sheet along the in-plane direction (saturation magnetization 241.46 emu/g) are in agreement with those recently reported by Vadillo et al.[215] Still, the out-of-plane value do not agree well, for that matter we only considered comparing the in-plane direction for all the samples. Accordingly, the thickness does not strongly affect the coercive fields of the measured samples. However, the saturation magnetization values were different with respect to the thickness. The low value of saturation magnetizations at small thickness (990nm thick) compared to FeCoV alloy sheet and $CoFe_2O_4$ sheet (0.1mm thick) are related to the size reduction, leading to an enhancement of the surface effect. Indeed, an increase in the surface spin disorder lead to an increase in its anisotropy.

However, with increasing the $CoFe_2O_4$ nanoporous oxide layer thickness to 1500nm, and 3300nm respectively, their Ms values are not very far from those of $CoFe_2O_4$ sheet (0.1mm in thick). To summarize, by increasing the thickness of $CoFe_2O_4$ nanoporous oxide layer, the magnetic properties are increasing which means that they are mainly coming from the $CoFe_2O_4$ sheet.

Thickness	**M_s (emu/g) (in plane)**	**H_c (Oe) (in plane)**	**M_s (emu/g) (out of plane)**	**H_c (Oe) (out of plane)**
0.1mm (FeCoV alloy sheet)	241.46	37.50	162.06	160.30
0.1mm ($CoFe_2O_4$ sheet)	261.06	30.86	165.23	143.70
990 nm ($CoFe_2O_4$_nanoporous oxide layer)	234.66	32.42	153.86	153.71
1500 nm ($CoFe_2O_4$_nanoporous oxide layer)	247.66	30.90	155.93	124.60
3300 nm ($CoFe_2O_4$_nanoporous oxide layer)	248.96	31.75	155.56	122.14

Table 6. *The values of saturation magnetizations and coercive fields of FeCoV alloy sheet, $CoFe_2O_4$ sheet and the formed $CoFe_2O_4$ nanoporous oxide layer.*

Conclusion

Cobalt ferrite $CoFe_2O_4$ nanoporous oxide layer have been fabricated for the first time, using self-ordering electrochemical anodization. The best morphology of the nanoporous oxide layer was formed under optimized anodization conditions and electrolyte compositions. The EDS analysis and XRD experiments demonstrated that the fabricated nanoporous oxide layer transformed to $CoFe_2O_4$ phase. The hysteresis loops and the magnetic properties of FeCoV alloy sheet, $CoFe_2O_4$ sheet and $CoFe_2O_4$ nanoporous oxide layer showed a high magnetic anisotropy along the in plane and out of plane directions due to the texture characterized the FeCoV alloy sheet. Furthermore, we have investigated the magnetic properties of FeCoV alloy sheet, $CoFe_2O_4$ sheet (0.1mm in thick) and $CoFe_2O_4$ nanoporous oxide layer with different thicknesses going from 990nm, 1500nm, to 3300nm. The lower Ms for small thickness (990nm) may be due to the enhanced role of the surface and its anisotropy. By increasing the thicknesses to 1500nm, and 3300nm, the magnetic properties are highly affected by those of $CoFe_2O_4$ sheet.

Conclusion and Perspectives

The subject of this thesis is divided into two parts. The objective of the first part was focused on studying the structural, electronic, magnetic and magnetocaloric properties of Mn_3AC (A=Ga, Al) antiperovskite materials as candidates for magnetic refrigeration. As known in the literature, Rare earth-based alloys, especially Gadolinium *Gd* were amongst the used materials for magnetic refrigeration application. However, these materials exhibit a weak resistance to oxidation and corrosion as well as their rarity and harmful effect towards environment. Mn_3AC (A=Ga, Al) may be considered as a suitable material, because of their abundance and friendly to environment.

The antiperovskite Mn_3GaC is characterized by two magnetic transitions. The first one being a first-order transition from antiferromagnetic (AF) to (FM), this transition occurs at a temperature of about $T_i \sim 160K$, and is found to be accompanied by expansion of the lattice parameter, and it undergoes a second order transition from ferromagnetic (FM) to paramagnetic (PM) at a Curie temperature Tc = 249K. Many studies discussed and investigated the magnetocaloric effect of the first order transition, which concluded that this material exhibits a giant magnetocaloric effect at this transition. However, no work was performed on the study of Mn_3GaC second transition. For the first time, we shed light on the magnetocaloric properties at the second transition by means of theoretical methods including Density Functional Theory and Monte-Carlo simulation. After thorough investigation, we found that the maximum values of the magnetic entropy change (ΔS_m^{max}) , the adiabatic temperature change(ΔT_{ad}) , and the relative cooling power are found to be 5.65J/Kg.K, 13.81K, and 351.90J/kg respectively after applying a magnetic field of H=4.5T. For a deeper study, we chose another antiperovskite Mn_3AlC which belongs to the same family of materials of Mn_3GaC. Contrary to Mn_3GaC, the antiperovskite Mn_3AlC exhibits only a second order transition at a Curie temperature Tc=287K. Various theoretical studies treated its magnetocaloric properties. However, their theoretical results were too incompatible with experimental data, which is what motivated us to explore another approach using the same methods as for Mn_3GaC. We found that the maximum values of ΔS_{mag}, ΔT_{ad} and RCP for Mn_3AlC are 6.40J/Kg.K,13.60K, and 416.96J/Kg respectively.

The second part of our study is dedicated to inquiring the $CoFe_2O_4$ nanostructures: $CoFe_2O_4$ nanorods and $CoFe_2O_4$ nanoporous oxide layers. Both nanostructures were characterized by Scanning Electron Microscopy (SEM), X-ray spectroscopy (EDS) and X-ray Diffraction (XRD). For the synthesis of $CoFe_2O_4$ nanorods, four steps are required namely, the substrate

preparation, the preparation of porous anodic aluminum oxide (AAO) templates, the electrochemical deposition of vertically aligned $CoFe_2O_4$ nanorods arrays into supported anodic alumina templates and finally the thermal oxidation of $CoFe_2$ nanorods arrays. After testing many electrolyte compositions, we succeeded in the fabrication of the $CoFe_2$ nanorods. the later have longer thicknesses in the order of the AAO thicknesses (approximately 600nm) and diameter of about 80nm. However, based on literature and on our experimental conditions, the $CoFe_2$ nanorods seemed to become distorted and transformed into a thick film layer of $CoFe_2O_4$. Unfortunately, we failed to preserve the ordered nanorods structure after thermal oxidation.

For the second nanostructure type, the Cobalt ferrite $CoFe_2O_4$ nanoporous oxide layer have been fabricated for the first time, using self-ordering electrochemical anodization. The most suited morphology of FeCoV nanoporous layer was formed under optimized anodization conditions and electrolyte compositions. The EDS analysis and XRD experiments demonstrated that the FeCoV nanoporous layer transformed to $CoFe_2O_4$ nanoporous oxide layer. The hysteresis loops and the magnetic properties of $CoFe_2O_4$ nanoporous oxide layer were stable along the parallel direction. Meanwhile, they were not along the normal direction. Furthermore, magnetic properties investigation was performed on $CoFe_2O_4$ sheet (0.1mm in thick) and $CoFe_2O_4$ nanoporous oxide layer with different thicknesses going from 990nm, 1500nm, to 3300nm. The lower Ms obtained for small thickness (990nm) may be due to the enhanced role of the surface and its anisotropy. By increasing the thicknesses to 1500nm, and 3300nm, the magnetic properties are highly affected by those of $CoFe_2O_4$ sheet, hindering by the occasion magnetic properties of $CoFe_2O_4$ nanoporous layer. Still, the trial and error of magnetic properties gave different results at each magnetic measurement for the out-of-plane direction, the answer for this discrepancy is still not understood and requires a thorough experimental study as the obtained results are not coherent with experiment.

References

[1] J. D. Jackson, Classical electrodynamics: Wiley, 1999.

[2] R. Skomski, Simple models of magnetism: Oxford University Press on Demand, 2008.

[3] Dirac, Paul Adrien Maurice. "The quantum theory of the electron." Proceedings of the Royal Society of London. Series A, Containing Papers of a Mathematical and Physical Character 117.778 (1928): 610-624.

[4] Schiff, L. I. (1968). Quantum Mechanics (3rd ed.). McGraw-Hill. p. 440.

[5] Shankar, R. (1980). Principles of Quantum Mechanics. Plenum Press. pp. 398–400. ISBN 0306403978.

[6] C.A. Gonano; R.E. Zich; M. Mussetta (2015). "Definition for Polarization P and Magnetization M Fully Consistent with Maxwell's Equations" (PDF). Progress in Electromagnetics Research B. 64: 83–101. doi:10.2528/PIERB15100606

[7] Carlin, R. L. (1986). Magnetochemistry (Berlin, Springer-Verlag).

[8] "Evaluation of Eddy-Current Effects on Diamagnetic Bearings for Microsystems", Jie-Yu Chen, Jian-Bin Zhou, G. Meng, and Wen-Ming Zhang, IEEE Transaction on industrial electronics, Vol. 56, No. 4, (2009).

[9] "Diamagnetic bearings for MEMS: Performance and stability analysis", Jie-Yu Chen, Jian-Bin Zhou, Guang Meng, Mechanics Research Communications, Vol. 35, Iss. 8, pp. 546–552 (2008).

[10] "Efficient modeling approach for optimization of a system based on passive diamagnetic levitation as a platform for bio- medical applications", H. Chetouani, B. Delinchant, G. Reyne, COMPEL - The international journal for computation and mathematics in electrical and electronic engineering, Vol. 26 Iss. 2, pp.345 – 355 (2007).

[11] "Magnetic levitation of large water droplets and mice", L. Yuanming, Zh. Da-Ming, S. Donald M., I. Ulf, Advances in Space Research, No. 45 (1), pp. 208–213 (2010).

[12] "Magnetic gravity trick grows perfect crystals', K. Kurt, New Scientist (2011).

[13] K. H. J. Buschow et F. R. de Boer, Physics of Magnetism and Magnetic Materials, New York:Kluwer Academic/Plenum Publishers, 2003.

[14] K. E. Geckeler et H. Nishide, Advanced nanomaterials, John Wiley and Sons, 2009

[15] Néel, M. Louis. "Propriétés magnétiques des ferrites; ferrimagnétisme et antiferromagnétisme." Annales de physique. Vol. 12. No. 3. EDP Sciences, 1948.

[16] Goldman, Alex. Modern ferrite technology. Springer Science & Business Media, 2006.

[17] Sharifi, Ibrahim, Hooman Shokrollahi, and S. Amiri. "Ferrite-based magnetic nanofluids used in hyperthermia applications." Journal of magnetism and magnetic materials 324.6 (2012): 903-915.

[18] Weiss, Pierre. "L'hypothèse du champ moléculaire et la propriété ferromagnétique." (1907).

[19] "The Science and Engineering of Materials, Sixth Edition", D. R. Askeland, P. P. Fulay, W. J. Wright. Publisher, Global Engineering, pp. 777-784 (2010).

[20] Dirac, Paul Adrien Maurice. "The quantum theory of the electron." Proceedings of the Royal Society of London. Series A, Containing Papers of a Mathematical and Physical Character 117.778 (1928): 610-624.

[21] H. A. Kramers, Physica 1, 182 (1934).

[22] P. W. Anderson, Phys. Rev. 79, 350 (1950).

[23] Craik, D. J. (Ed.), Magnetic Oxides, John Willey and Sons, London, 1975.

[24] L. Néel, Adv. Phys. 4 (1955) 191.

[25] VARGAS, J. M., NUNES, W. C., SOCOLOVSKY, L. M., KNOBEL, M., ZANCHET, D., Effect of dipolar interaction observed in iron-based nanoparticles, Phys. Rev. B 72 (2005), 184428

[26] DORMANN, J. L., D'ORAZIO, F., LUCARI, F., TRONC, E., PRENE, P., JOLIVET, J. P., FIORANI, D., CHERKAOUI, R., NOGUES, M., Thermal variation of the relaxation time of the magnetic moment of □-Fe2O3 nanoparticles with interparticle interactions of various strengths, Phys. Rev. B 53 (1996), 14291.

[27] BEAN, C. P., LIVINGSTON, J. D., Superparamagnetism, J. Appl. Phys. 30 (1959), S120.

[28] D. Gubbins et E. H. Bervera, Encyclopedia of geomagnetism and paleomagnetism, Springer, 2007

[29] H. E. Landsberg Advances in geophysics, Academic Press, 1965.

[30] COEY, J. M. D., Noncollinear Spin Arrangement in Ultrafine Ferrimagnetic Crystallites, Phys. Rev. Lett. 27 (1971), 1140.

[31] COEY, J. M. D., KHALAFALLA, D., Superparamagnetic □-Fe2O3, Phys. Stat. Sol. (a) 11 (1972), 229.

[32] BERKOWITZ, A. E., SCHUELE, W. J., Influence of Crystallite Size on the Magnetic Properties of Acicular Fe2O3 Particles, J. Appl. Phys. 39 (1968), 1261.

[33] E. Warburg, Magnetische Untersuchungen, Annalen der Physik 249 (5) (1881) 141–164. doi:10.1002/andp.18812490510.

[34] P. Debye, Einige Bemerkungen zur Magnetisierung bei tiefer Temperatur, Annalen der Physik 386 (25) (1926) 1154–1160. doi:10.1002/andp.19263862517.

[35] W. F. Giauque, A Thermodynamic Treatment of certain magnetic effects. A proposed method of producing temperatures considerably below 1º absolute, Journal of the American Ceramic Society 49 (8) (1927) 1864–1870. doi:10.1021/ja01407a003.

[36] W. F. Giauque, D. P. MacDougall, Attainment of Temperatures Below 1° Absolute by Demagnetization of Gd2(SO4)3·8H2O, Physical Review 43 (9) (1933) 768–768. doi: 10.1103/PhysRev.43.768.

[37] A. M. Tishin and Yu. I. Spichkin, The Magnetocaloric Effect and Its Applications (IOP Publication, Bristol, UK, 2003).

[38] M. Balli, Ph.D. thesis, Joseph Fourier University, Grenoble, France, 2007.

[39] O. Tegus, Ph.D. thesis, University of Amsterdam, 2003.

[40] M. Phan and S. Yu. J. Magn. Magn. Mater., 308:325), 2007.

[41] E. Bruck. J.Phys. D: Appl.Phys., 38:R381, 2005

[42] V. Franco, J.S. Bl´azquez, B. Ingale, and A. Conde. Annu. Rev. Mater. Res., 42:305–42,2012.

[43] B. F. Yu, M. Liu, and P. W. Egolf. Int. J. Refrig., 33:10291060, 2010.

[44] K. G. Sandeman. Scripta Mater., 67:566–571, 2012.

[45] K. A. Gschneidner and V. K. Pecharsky. Annu. Rev. Mater. Sci., 30:387, 2000.

[46]V. K. Pecharsky and K. A. Gschneidner. Phys. Rev. Lett, 78:4494), 1997.

[47] B. G. Shen, J. R. Sun, F. X. Hu, H. W. Zhang, and Z. H. Cheng. Adv. Mater., 21:4545– 4564, 2009. 39

[48] O. Gutfleish, A. Yan, and K. Muller. J. Appl. Phys., 97:10M305, 2005. 39

[49] K. Mandal, O. Gutfleish, A. Yan, A. Handstein, and K. H. Muller. J. Magn. Mater., 673:290, 2005. 39

[50] M. D. Kuzmin and M. Richter. Phys. Rev. B., 76:092401–1, 2007. 39

[51] A. Fujita, S. Fujieda, K. Fukamichi, H. Mitamura, and T. Goto. Phys. Rev. B, 65:014410, 2001. 39

[52] L. Jia, G. J. Liu, J. R. Sun, H. W. Zhang, F. X. Hu, C. Dong, G. H. Rao, and B. G. Shen. J. App. Phys., 100:1239041, 2006. 39, 93, 98

[53] S. Gama, A. A. Coelho, A. de Campos, A. M. G. Carvalho, F. C. G. Gandra, P. J. von Ranke, and N. A. de Oliveira. Phys. Rev. Lett., 23:237202–1–237202–4, 2004. 39

[54] H. Wada and Y. Tanabe. Appl. Phys. Lett.), 79:3302), 2001. 39

[55] K. Taniguchi T. Shibata Y. Yamada H. Wada, T. Morikawa and Y. Akishige. Physica B, 328:114, 2003. 39

[56] M. Guillot R. Zach and R. Fruchart. J. Magn. Magn. Mater., 89:221, 1990. 39

[57] N. H. Dung, Z. Q. Ou, L. Caron, L. Zhang, D. T. C. Thanh, G. A. de Wijs, R. A. de Groot, K. H. J. Buschow, and E. Brck. Adv. Energy Mater., 1:1215, 2011. 40

[58] V. D. Buchelnikov. Int. J. Appl. Electromagn. Mech., 23:65, 2006. 40, 46

[59] Feng-xia Hu, Bao-gen Shen, Ji-rong Sun, and Guang-heng Wu. Phys. Rev. B, 64:132412, 2001. 40

[60] B. Ingale, R. Gopalan, M. M. Raja, V. Chandrasekaran, and S. Ram. J. Appl. Phys., 102:013906, 2007. 40

[61] J.-P. Bouchaud, R. Fruchart, R. Pauthenet, M. Cuillot, H. Bartholin, F. Chaissé, J. Appl. Phys. 1966, 37, 3.

[62] B. S. Wang, C. C. Li, J. C. Lin, L. J. Li, P. Tong, X. B. Zhu, Z. R. Yang, W. H. Song, J. M. Dai, Y. P. Sun, J. Magn. Magn. Mater. 2011, 323, 2017.

[63] D. Fruchart, E. F. Bertaut, F. Sayetat, M. Nasr Eddine, R. Fruchart, J. P. Sénateur. Structure Magnetique et Mn3GaC. Solid State Commun. Vol. 8:pp. 91 (1970)

[64] D. Fruchart, E. F. Bertaut, F. Sayetat, M. Nasr Eddine, R. Fruchart, J. P. Sénateur. Structure Magnetique et Mn3GaC. Solid State Commun. Vol. 8:pp. 91 (1970)

[65] T. Kaneko, T. Kanomata, K. Shirakawa. Pressure Effect on the Magnetic Transition Temperatures in the Intermetallic Compounds Mn3GaC (M=Ga, Zb and Sn). J. Phys. Soc. Jpn. Vol. 56, 11, (1987)

[66] T. Tohei, H. Wada, T. Kanomata. Negative magnetocaloric effect at the antiferromagnetic to ferromagnetic transition of Mn3GaC. J. Appl. Phys. Vol. 94, 3, (2003), DOI: 10.1063/1.1587265 21, 22, 47, 49, 51, 53, 59, 65, 70, 71, 78, 80, 101, 104

[67] Ö. Çakır, M. Acet, M. Farle, A. Senyshyn. Neutron diffraction study of the magnetic-field-induced transition in Mn3GaC. J. Appl. Phys. Vol. 115, 043913, (2014), DOI: 10.1063/1.4862903

[68] D. Fruchart, E. F. Bertaut. Magnetic Studies of the Metallic Perovskite Type Compounds of Manganese∗. J. Phys. Soc. Jpn. Vol. 44, 3, (1978) 21, 22, 24, 78

[69] J. García, J. Bartolomé, D. González. Thermophysical properties of intermetallic Mn3MC perovskites. J. Chem. Thermodyn. Vol. 15: pp. 1059 (1983) 21, 22

[70] F. Scheibel, T. Gottschall, K. Skokov, O. Gutfleisch, M. GhorbaniZavareh, Y. Skourski, J. Wosnitza, Ö. Çakır, M. Farle, M. Acet. Dependence of the inverse magnetocaloric effect on the field-change rate in Mn3GaC and its relationship to the kinetics of the phase transition. J. Appl.

Phys. Vol. 117, 233902, (2015), DOI: 10.1063/1.4922722 3, 13, 21, 22, 45, 47, 48, 49, 55, 57, 59, 62, 64, 70

[71] B. S. Wang, P. Tong, Y. P. Sun, W. Tang, L. J. Li, X. B. Zhu, Z. R. Yang, W. H. Song. Structural, magnetic properties and magnetocaloric effect in Ni-doped antiperovskite compounds GaCMn3-xNix (0≤x≤0.10). Physica B: Condensed Matter Vol. 405:pp. 2427 (2010), DOI: 10.1016/j.physb.2010.03.001 22

[72] T. Harada, K. Nishimura, T. Kanomata, T. Kaneko. Transport Properties of Ternary Magnetic Compounds Mn3-xMxGaC (M=Cr and Fe). Jpn. J. Appl. Phys. Vol. 32:pp. 280 (1993)

[73] T. Kaneko, T. Kanomata, K. Shirakawa. Pressure Effect on the Magnetic Transition Temperatures in the Intermetallic Compounds Mn3GaC (M=Ga, Zb and Sn). J. Phys. Soc. Jpn. Vol. 56, 11, (1987)

[74] T. Harada, K. Nishimura, T. Kanomata, T. Kaneko. Transport Properties of Ternary Magnetic Compounds Mn3-xMxGaC (M=Cr and Fe). Jpn. J. Appl. Phys. Vol. 32:pp. 280 (1993)

[75] Wang, B. S., et al. "Large magnetic entropy change near room temperature in antiperovskite $SnCMn_3$." EPL (Europhysics Letters) 85.4 (2009): 47004.

[76] P. l'Heritier, D. Boursier, R. Fruchart, D. Fruchart, Mater. Res. Bull. 1979, 14, 1203

[77] O Cakır, M. Acet, J. Magn. Magn. Mater. 2013, 344, 207

[78] Yu M H, Lewis L H and Moodenbaugh A R 2003 J. Appl. Phys. 93 10128

[79] Wang B S, Tong P, Sun Y P, Zhu X B, Luo X, Li G, Song W H, Yang Z R and Dai J M 2009 J. Appl. Phys. 105 083907

[80] Kenmotsu A, Shinohara T and Watanabe H 1972 J. Phys. Soc. Jpn. 32 377

[81] Wang B S, Lin J C, Tong P, Zhang L, Lu W J, Zhu X B, Yang Z R, Song W H, Dai J M and Sun Y P 2010 J. Appl. Phys. 108 093925

[82] Wrinkler, G. (1971) Magnetic Properties of Materials. McGraw-Hill: New York.

[83] Sickafus, K.E., Wills, J.M. (1999) Structure of spinel. J. Am. Ceram. Soc. 82, 3279-3292.

[84] Goldman, A. (2006) Modern ferrite technology. Springer: New York.

[85] E.J.W. Verwey and E.L. Hellmann, J. Chem. Phys. 15 (1947) 174.

[86] E.J.W. Verwey, F. De Boer and J.N. Van Santion, J. Chem. Phys. 76 (1948) 1091.

[87] T.F.W. Barth and E. Posnjac, Zs. Kristallographie 84 (1952) 325.

[88] A. Hagfeldth, M. Gratzel, Chem. Rev. 95 (1995) 49.

[89] S. Prasad, N. S. Gajbhiye, J. Alloys Compd. 265 (1998) 87.

[90] B. Viswanathan, V.R.K. Murthy: Ferrite Materials. Springer Verlag, Berlin (1990)

[91] Matsunaga, T., Kamiya, S. (1987) Use of magnetic particles isolated from magnetotactic bacteria for enzyme immobilization. Appl. Microbio. Biotechnol. 26, 328–332.

[92] Han, D.H., Luo, H.L., Yang, Z. (1996) Multifunctional nanoparticles possessing a magnetic motor effect for drug or gene delivery. J. Magn. Magn. Mater. 161, 376- 378.

[93] Pervaiz, E., Gul, I.H. (2014) High frequency ac response, dc resistivity and magnetic studies of holmium substituted Ni-ferrite: A novel electromagnetic material. J. Magn. Magn. Mater. 349, 27-34.

[94] Giri, A.K., Pellerin, K., Pongsaksawad, W., Sorescu, M., Majetich, S.A. (2000) Photomagnetism and structure in cobalt ferrite nanoparticles. IEEE Trans. Magn. 36, 3026-3029

[95] ˇSafaˇr´ık, I., ˇSafaˇr´ıkov´a, M. (2002) Magnetic nanoparticles and biosciences. Monatshefte fur Chemie, 133, 6, 737– 759.

[96] Yeh, T.C., Zhang, W., Ildstad, S.T., Ho, C. (1995) In vivo dynamic MRI tracking of rat T-cells labeled with super paramagnetic iron-oxide particles. Magn. Reson. Medic. 33, 200–208.

[97] Martin, C.R., Mitchell, D.T. (1998) Nanomaterials in analytical chemistry, Analyt. Chem., 70, 322A–327A.

[98] Jordan, A., Scholz, R., Maier-Hauff K., (2001) Presentation of a new magnetic field therapy system for the treatment of human solid tumors with magnetic fluid hyperthermia. J. Magn. Magn. Mater., 225, 118–126.

[99] Maaz, K., Mumtaz, A., Hasanain, S. K., & Ceylan, A. (2007). Synthesis and magnetic properties of cobalt ferrite ($CoFe_2O_4$) nanoparticles prepared by wet chemical route. Journal of magnetism and magnetic materials, 308(2), 289-295.

[100] Wang, Cheng-Chien, I-Han Chen, and Chun-Rong Lin. "Preparation and characterization of hollow magnetic silica ($CoFe_2O_4$–SiO_2) microspheres." Journal of Magnetism and Magnetic Materials 304.1 (2006): e451-e453.

[101] Lee, Sang Won, and Chul Sung Kim. "Mössbauer studies on the superparamagnetic behavior of $CoFe_2O_4$ with a few nanometers." Journal of Magnetism and Magnetic Materials 303.2 (2006): e315-e317.

[102] Xiangfeng, C., Dongli, J., Yu, G., & Chenmou, Z. (2006). Ethanol gas sensor based on $CoFe_2O_4$ nano-crystallines prepared by hydrothermal method. Sensors and Actuators B: Chemical, 120(1), 177-181.

[103] Thang, P. D., G. Rijnders, and David HA Blank. "Stress-induced magnetic anisotropy of $CoFe_2O_4$ thin films using pulsed laser deposition." Journal of Magnetism and Magnetic Materials 310.2 (2007): 2621-2623.

[104] Hua, Z. H., et al. "$CoFe_2O_4$ nanowire arrays prepared by template-electrodeposition method and further oxidization." Journal of alloys and compounds 427.1-2 (2007): 199-203.

[105] Losic, Dusan, et al. "Self-ordering electrochemistry: a simple approach for engineering nanopore and nanotube arrays for emerging applications." Australian Journal of Chemistry 64.3 (2011): 294-301.

[106] Ghicov, Andrei, and Patrik Schmuki. "Self-ordering electrochemistry: a review on growth and functionality of TiO_2 nanotubes and other self-aligned MO_x structures." Chemical Communications 20 (2009): 2791-2808.

[107] Hartree DR (1928) The Wave Mechanics of an Atom with a Non-Coulomb Central Field. PartI. Theory and Methods. Mathematical Proceedings of the Cambridge Philosophical Society, 24:89–110.

[108] Fock V (1930) N¨aherungsmethode zur L¨osung des quantenmechanischen Mehrk¨orperproblems. ZPhysik 61: 126–148.

[109] Slater JC (1930) Note on Hartree's Method. Phys Rev 35: 210–211.

[110] D.R. Hartree, Proceedings of the Cambridge Philosophical Society 24 (1928) 89.

[111] R. G. Parr, Ann. Rev. Phys. Chem. 34, 631 (1983). 22.

[112] T. Ziegler, Chem. Rev. 91, 651 (1991). 22.

[113] P. Geerlings, F. D. Proft, and W. Langenaeker, Chem. Rev. 103, 1793 (2003). 22

[114] R. O. Jones and O. Gunnarsson, Rev. Mod. Phys. 61, 689 (1989). 22

[115] R. G. Parr and W. Yang, Density-Functional Theory of Atoms and Molecules (Oxford University Press, New York, 1989). 22

[116] M. R. Dreizler and E. K. U. Gross, Density Functional Theory : An Approach to the Quantum Many-Body Problem (Springer, Berlin, 1990). 22

[117] L. H. Thomas, Proc. Camb. Phil. Soc. 23, 542 (1927). 22

[118] E. Fermi, Rend. Accad. Lincei. 6, 602 (1927). 22

[119] P. Hohenberg and W. Kohn, Phys. Rev. 136, B864 (1964). 23, 58

[120] W. Kohn and L. J. Sham, Phys. Rev. 140, A1133 (1965). 24, 58

[121] J. P. Perdew and K. Schmidt, in Density Functional Theory and Its Application to Materials, edited by V. Van Doren (AIP Press, Melville, New York, 2001). 2, 26

[122] M. Gell-Mann and K. A. Brueckner, Phys. Rev. 106, 364 (1957). 26

[123] D. M. Ceperley and B. J. Alder, Phys. Rev. Lett. 45, 566 (1980). 26

[124] J. P. Perdew and A. Zunger, Phys. Rev. B 23, 5048 (1981). 26, 34, 58, 60

[125] J. P. Perdew and Y. Wang, Phys. Rev. B 45, 13244 (1992). 26

[126] S. J. Vosko, L. Wilk, and M. Nusair, Can. J. Phys. 58, 1200 (1980). 26 Bibliography 103

[127] O. Gunnarsson and B. I. Lundqvist, Phys. Rev. B 13, 4274 (1976). 26

[128] O. Gunnarsson, M. Jonson, and B. I. Lundqvist, Sol. Stat. Comm. 24, 765 (1977). 26

[129] T. Ziegler, A. Rauk, and E. J. Baerends, Theor. Chim. Acta 43, 261 (1977).26

[130] K. Burke, J. P. Perdew, and M. Ernzerhof, J. Chem. Phys. 109, 3760 (1998).26

[131] J. P. Perdew, K. Burke, and Y. Wang, Phys. Rev. B 54, 16533 (1992). 27, 58

[132] J. P. Perdew, K. Burke and M. Ernzerhof, Phys. Rev. Lett. 77, 3865 (1996); 78, 1396 (1197). 27, 34, 58, 60

[133] Y. Zhang and W. Yang, Phys. Rev. Lett. 80, 890 (1998). 27, 34

[134] Z. Wu and R. E. Cohen, Phys. Rev. B 73, 235116 (2006). 27, 34, 35, 36

[135] J. P. Perdew, A. Ruzsinszky, G. I. Csonka, O. A. Vydrov, G. E. Scuseria,

[136] K. Schwarz and P. Blaha, "Solid state calculations using WIEN2k," Computational Materials Science, vol. 28, pp. 259-273, 2003.

[137] Blaha, Peter, et al. "wien2k." An augmented plane wave+ local orbitals program for calculating crystal properties (2001).

[138] L. Onsager, Phys. Rev., vol. **65**, p. 117, 1944.

[139] N. Metropolis, A. Rosenbluth, M. Rosenbluth, A. Teller, E. Teller, J. Chem. Phys. , vol. **21**, p. 1087, 1953.

[140] W. E. Pickett, Pseudopotential Methods in Condensed Matter Applications, **9** , 1989, 115-197.

[141] R. Krahne, G. Morello, A. Figuerola, C. George, S. Deka, L. Manna, Physics Reports, 501 (2011) 75 221.

[142] C.N.R. Rao, F.L. Deepak, G. Gundiah, A. Govindaraj, Progress in Solid State Chemistry, 31 (2003) 5-147.

[143] S.S. Djokic, Electrodeposition: Theory and Practice, Springer Science & Business Media, 2010.

[144] B. Hong, C.-h. Jiang, X.-j. Wang, Texture of electroplated copper film under biaxial stress, Mater. Trans. 47 (2006) 2299-2301

[145] K. Asa Deepthi, R. Balachandran, B.H. Ong, K.B. Tan, H.Y. Wong, H.K. Yow, S. Srimala, Physical and electrical characteristics of NiFe thin films using ultrasonic assisted pulse electrodeposition, Appl. Surf. Sci. 360 (2016) 519-524.

[146] M.S. Chandrasekar, M. Pushpavanam, Pulse and pulse reverse plating Conceptual, advantages and applications, Electrochim. Acta 53 (2008) 3313-3322

[147] M. Sajjadnejad, A. Mozafari, H. Omidvar, M. Javanbakht, Preparation and corrosion resistance of pulse electrodeposited Zn and ZneSiC nanocomposite coatings, Appl. Surf. Sci. 300 (2014) 1-7.

[148]Lohrengel M M 1993 Thin anodic oxide layers on aluminium and other valve metals: high field regime Mater. Sci. Eng. R 11 243–94.

[149] Diggle J W, Downie T C and Goulding CW 1969 Anodic oxide films on aluminum Chem. Rev. 69 365–405

[150] Zwilling V, Aucouturier M and Darque-Ceretti E 1999 Anodic oxidation of titanium and TA6V alloy in chromic media. An electrochemical approach Electrochim. Acta 45 921–9

[151] PrakasamHE, VargheseOK, Paulose M, MorGKand Grimes CA 2006 Synthesis and photoelectrochemical properties of nanoporous iron (III) oxide by potentiostatic anodization Nanotechnology 17 4285

[152] Chu S-Z, Wada K, Inoue S, Todoroki S-I, Takahashi YKand HonoK2002 Fabrication and characteristics of ordered Ni nanostructures on glass by anodization and direct current electrodeposition Chem. Mater. 14 4595–602.

[153] Wang Y, Jiang T, Meng D, JinHand YuM2015 Controllable fabrication of nanowire-like CuOfilm by anodization and its properties Appl. Surf. Sci. 349 636–43

[154] Chang S-S, Kurokawa S and Sakai A2003 Properties of annealed anodically etched porous Zn studied by scanning tunneling microscopy Appl. Surf. Sci. 217 50–5

[155] Tsuchiya H, Macak JM, Taveira L and Schmuki P 2005 Fabrication and characterization of smooth high aspect ratio zirconia nanotubes Chem. Phys. Lett. 410 188–91

[156] Sieber I, Hildebrand H, Friedrich A and Schmuki P 2005 Formation of self-organized niobium porous oxide on niobium Electrochem. Commun. 7 97–100

[157] TsuchiyaHand Schmuki P 2005 Self-organized high aspect ratio porous hafnium oxide prepared by electrochemical anodization Electrochem. Commun. 7 49–52

[158] Sieber I, Hildebrand H, Friedrich A and Schmuki P 2006 Initiation of tantalum oxide pores grown on tantalum by potentiodynamic anodic oxidation J. Electroceram. 16 35–9

[159] Tsuchiya H, Macak JM, Sieber I, Taveira L, Ghicov A, SirotnaKand Schmuki P 2005 Self-organized porousWO3 formed in NaF electrolytes Electrochem. Commun. 7 295–8

[160] Berger S, TsuchiyaHand Schmuki P 2008 Transition from nanopores to nanotubes: self-ordered anodic oxide structures on titanium-aluminides Chem. Mater. 20 3245–7

[161] Ghicov A, Aldabergenova S, TsuchyiaHand Schmuki P 2006 TiO2–Nb2O5 nanotubes with electrochemically tunable morphologies Angew. Chem., Int. Ed. 45 6993–6

[162] Macak JM, Tsuchiya H, Taveira L, Ghicov A and Schmuki P 2005 Self-organized nanotubular oxide layers on Ti-6Al-7Nb and Ti-6Al-
4V formed by anodization inNH4F solutions J. Biomed. Mater. Res. A 75 928–33

[163] Roy P, Berger S and Schmuki P 2011 TiO2 nanotubes: synthesis and applications Angew. Chem., Int. Ed. 50 2904–39

[164] ParkhutikVand ShershulskyV1992 Theoretical modelling of porous oxide growth on aluminium J. Phys. D: Appl. Phys. 25 1258

[165] MacdonaldDD1993 On the formation of voids in anodic oxide films on aluminum J. Electrochem. Soc. 140 L27–30

[166] Pakes A, Thompson G, Skeldon P and Morgan P 2003 Development of porous anodic films on 2014-T4 aluminium alloy intetraborate electrolyte Corros. Sci. 45 1275–87

[167] Siejka J and Ortega C1977 AnO18 study of field-assisted pore formation in compact anodic oxide films on aluminum J. Electrochem. Soc. 124 883–91

[168] MorGK, VargheseOK, Paulose M, ShankarKand GrimesCA 2006 A review on highly ordered, vertically oriented TiO2 nanotube arrays: fabrication, material properties, and solar energy applications Sol. Energy Mater. Sol. Cells 90 2011–75

[169] V.K. Pecharsky, K.A. Gschneidner, Magnetocaloric effect and magnetic refrigeration, J. Magn. Magn Mater. 200 (1999) 44.

[170] C.R.H. Bahl, K. Navickaite, H.N. Bez, T. Lei, K. Engelbrecht, R. Bjørk, K. Li, Z. Li, _ J. Shen, W. Dai, Operational test of bonded magnetocaloric plates, Int. J. Refrig. 76 (2017) 245

[171] O. Tegus, X.W. Li, F.R. de Boer, K.H.J. Buschow, Magnetic refrigeration-towards room-temperature applications, Phys. B 327 (2003) 431.

[172] Z.G. Zheng, H.Y. Yu, X.C. Zhong, D.C. Zeng, Z.W. Liu, Design and performance study of the active magnetic refrigerator for room temperature, Int. J. Refrig. 32 (2009) 78.

[173] Lyubina Julia, Magnetocaloric materials for energy efficient cooling, J. Phys. D Appl. Phys. 50 (2017), 053002

[174] Dang Thanh, Tran, et al. "Magnetic properties and magnetocaloric effect in Fe90− x Ni x Zr10 alloy ribbons." Journal of Applied Physics 113.21 (2013): 213908.

[175] M. Balli, D. Fruchart, D. Gignoux, E.K. Hlil, S. Miraglia, P. Wolfers, Gd1-xTbx alloys for Ericsson-like magnetic refrigeration cycles, J. Alloy. Comp. 442 (2007) 129

[176] O. Sari, M. Balli, From conventional to magnetic refrigerator technology, Int. J. Refrig. 37 (2014) 8.

[177] Dexin Li, Yoshiya Homma, Fuminori Honda, Tomoo Yamamura, Dai Aoki, Large magnetocaloric effect and magnetic properties in ErCoAl, Phys. Proced. 75 (2015) 1300.

[178] Murtaza Bohra, S.C. Sahoo, Large magnetocaloric effect at Verwey point in nanocrystalline Fe3O4 thin films, J. Alloy. Comp. 699 (2017) 1118.

[179] K.A. Gschneidner Jr., V.K. Pecharsky, A.O. Tsokol, Recent developments in magnetocaloric materials, Rep. Prog. Phys. 68 (2005) 1479.

[180] Z.G. Zheng, X.C. Zhong, K.P. Su, H.Y. Yu, Z.W. Liu, D.C. Zeng, Magnetic properties and large magnetocaloric effects in amorphous GdeAleFe alloys for magnetic refrigeration, Sci. China Phys. Mech. Astron. 54 (2011) 1

[181] Lingwei Li, Zan Ding, Dexuan Huo, Yaping Guo, Yang Qi, Rainer Pottgen, Magnetic properties and magnetocaloric effect in Tm-based magnesium compounds Tm4PdMg and Tm4PtMg, J. Alloy. Comp. 680 (2016) 415.

[182] Z.G. Zheng, X.C. Zhong, H.Y. Yu, V. Franco, Z.W. Liu, D.C. Zeng, The magnetocaloric effect and critical behavior in amorphous Gd60Co40-xMnx alloys, J. Appl. Phys. 111 (2012), 07A922.

[183] R. Caballero-Flores, V. Franco, A. Conde, K.E. Knipling, M.A. Willard, Influence of Co and Ni addition on the magnetocaloric effect in Fe88-2xCoxNixZr7B4Cu1 soft magnetic amorphous alloys, Appl. Phys. Lett. 96 (2010), 182506.

[184] K.S. Zhang, J.N. Xue, Y.X. Wang, H. Sun, Y. Long, Magnetocaloric effect and corrosion resistance of La(Fe, Si)13 composite plates bonded by different fraction of phenolic resin, AIP Adv. 8 (2018), 048104.

[185] N. Ennassiri, N. Tahiri, O. El Bounagui, H. Ez-Zahraouy, A. Benyoussef, Structural, electronic, magnetic, and magnetocaloric properties in metallic antiperovskite compound Mn3GaC, Mater. Res. Bull. 98 (2018) 335.

[186] O. Çakır, F. Cugini, M. Solzi, K. Priolkar, M. Acet, M. Farle, Dynamics of nonergodic ferromagnetic/antiferromagnetic ordering and magnetocalorics in antiperovskite Mn3SnC, Phys. Rev. B 96 (2017), 014436.

[187] T.Tang, K. M. Gu, Q. Q. Cao, D. H. Wang, S. Y. Zangand Y. W. Du, J. Magn.Magn. Mater. 222, 110 (2000).

[188] A. Kitanovski and P. W. Egolf, Int.J. Refrig.29, 3 (2006).

[189] V.D. Buchelnikov, V.V. Sokolovskiy, H.C. Herper, H. Ebert, M.E. Gruner, S.V. Taskaev, V.V. Khovaylo, A. Hucht, A. Dannenberg, M. Ogura, First-principles and Monte Carlo study of magnetostructural transition and magnetocaloric properties of Ni2þxMn1xGa, Phys. Rev. B 81 (2010), 094411.

[190] J. Mallet, K. Yu-Zhang, S. Matefi-Tempfli, M. Matefi-Tempfli and L. Piraux, J. Phys. D: Appl. Phys., 2005, 38, 909–914

[191] Masuda, H.; Yada, K.; Osaka, A. Self-ordering of cell configuration of anodic porous alumina with large-size pores in phosphoric acid solution. Jpn. J. Appl. Phys. 1998, 37, L1340-L1342.

[192] Jessensky, O.; Muller, F.; Gosele, U. Self-organized formation of hexagonal pore arrays in anodic alumina. Appl. Phys. Lett. 1998, 72, 1173-1175.

[193] Jessensky, O.; Muller, F.; Gosele, U. Self-organised formation of hexagonal pore structures in anodic alumina. J. Electrochem. Soc. 1998, 145, 3735-3740.

[194] Li, F.; Zhang, L.; Metzger, R.M. On the growth of highly ordered pores in anodized aluminium oxide. Chem. Mater. 1998, 10, 2470-2480.

[195] Li, A.P.; Muller, F.; Birner, A.; Nielsch, K.; Gosele, U. Polycrytalline nanopore arrays with hexagonal ordering on aluminium. J. Vac. Sci. Technol. A 1999, 17, 1428-1431

[196] Li, A.P.; Muller, F.; Birner, A.; Nielsch, K.; Gosele, U. Hexagonal pore arrays with a 50–420 interpore distance formed by self-organisation in anodic alumina. J. Appl. Phys. 1998, 84, 6023-6026.

[197] Zhang, L.; Cho, H.S.; Li, F.; Metzger, R.M.; Doyle, W.D. Cellular growth of highly ordered porous anodic films on aluminium. J. Mater. Sci. Lett. 1998, 17, 291-294.

[198] Parkhutik, V. P. & Shershulsky, V. I. J. Phys. D: Appl. Phys. 25, 1258-1263 (1992).

[199] AlMawlawi, D., Coombs, N. & Moskovits, M. J. Appl. Phys. 70, 4421-4425 (1991).

[200] Takahashi, H. & Nagayama, M. Corrosion Science 18, 911-925 (1978).

[201] O'Sullivan J.P., Wood G.C. Nucleation and growth of porous anodic films on aluminium. P Roy. Lond. A Mat. 1970; A317:511–543. doi: 10.1098/rspa.1970.0129.

[202] Kawai, Satoshi, and Ryuzo Ueda. "Magnetic properties of anodic oxide coatings on aluminum containing electrodeposited Co and Co- Ni." Journal of the Electrochemical Society 122.1 (1975): 32.

[203] Gamburg, Yuliy D., and Giovanni Zangari. Theory and practice of metal electrodeposition. Springer Science & Business Media, 2011.

[204] Jagminas, Arūnas, et al. "Annealing effects on the transformations of Fe nanowires encapsulated in the alumina template pores." Materials Chemistry and Physics 115.1 (2009): 217-222.

[205] Masuda, Hideki, and Kenji Fukuda. "Ordered metal nanohole arrays made by a two-step replication of honeycomb structures of anodic alumina." science 268.5216 (1995): 1466-1468.

[206] Tsuchiya, Hiroaki, et al. "Self- organized high- aspect- ratio nanoporous zirconium oxides prepared by electrochemical anodization." Small 1.7 (2005): 722-725.

[207] Guo, Yafeng, et al. "High photocatalytic capability of self-assembled nanoporous WO3 with preferential orientation of (002) planes." Environmental science & technology 41.12 (2007): 4422-4427.

[208] Gong, Dawei, et al. "Titanium oxide nanotube arrays prepared by anodic oxidation." Journal of Materials Research 16.12 (2001): 3331-3334.

[209] Liu, Jun, Dongfeng Xue, and Keyan Li. "Single-crystalline nanoporous Nb_2O_5 nanotubes." Nanoscale research letters 6.1 (2011): 138.

[210] Yang, Yang, et al. "Enabling the anodic growth of highly ordered V_2O_5 nanoporous/nanotubular structures." Angewandte Chemie International Edition 50.39 (2011): 9071-9075.

[211] Albu, Sergiu P., Andrei Ghicov, and Patrik Schmuki. "High aspect ratio, self- ordered iron oxide nanopores formed by anodization of Fe in ethylene glycol/NH_4F electrolytes." physica status solidi (RRL)–Rapid Research Letters 3.2- 3 (2009): 64-66.

[212] Lee, Chong- Yong, Kiyoung Lee, and Patrik Schmuki. "Anodic Formation of Self- Organized Cobalt Oxide Nanoporous Layers." Angewandte Chemie International Edition 52.7 (2013): 2077-2081.

[213] Bervian, A., Ludwig, G. A., Raquel Kunst, S., Rossa Beltrami, L. V., Dewes Moura, A. B., Malfatti, C. D. F., & Trindade Oliveira, C. (2015). The influence of the glycerin concentration on the porous structure of ferritic stainless steel obtained by anodization. Dyna, 82(190), 46-52.

[214] Shang, C. H., Weihs, T. P., Cammarata, R. C., Ji, Y., & Chien, C. L. (2000). Anisotropy in magnetic and mechanical properties in textured Hiperco® FeCoV alloys. Journal of Applied Physics, 87(9), 6508-6510.

[215] Vadillo, Virginia, et al. "Synthesis and Characterization of Fe–Co–V High-Magnetization Nanoparticles Obtained by Physical Routes." IEEE Magnetics Letters 10 (2019) : 1-5.

Résumé

Cette thèse porte sur l'étude des propriétés structurales, électroniques, magnétiques et magnétocaloriques des matériaux antiperovskite de type Mn_3AC (A = Al, Ga) en utilisant des méthodes théoriques.

Pour Mn_3GaC, nous avons étudié la transition du second ordre. Un MCE significatif sans perte d'hystérésis est observé. D'autre part, l'antiperovskite Mn_3AlC subit également une transition de second ordre avec l'absence de perte d'hystérésis et des matières premières à faible coût et respectueuses de l'environnement. Pour cette raison, ces critères suggèrent que ces matériaux peuvent être de bons candidats pour des applications de réfrigération magnétique.

La seconde partie de cette thèse sera consacrée à la synthèse de nanostructures $CoFe_2O_4$ comprenant des nanorods et des couches d'oxide nanoporeux. Les deux nanostructures ont été caractérisées par microscopie électronique à balayage (SEM), spectroscopie rayons X (EDS) et diffraction des rayons X (XRD). Les cinq étapes de la synthèse de nanorods $CoFe_2O_4$ ont été reportées en fonction des nombreuses compositions d'électrolytes testées. La couche d'oxyde nanoporeux $CoFe_2O_4$ a été fabriquée par anodisation électrochimique de la feuille d'alliage parent FeCoV. Nos méthodes de caractérisation ont confirmé la transformation de la couche d'oxyde anodisé en couches d'oxyde nanoporeux $CoFe_2O_4$. Les propriétés magnétiques de la couche d'oxyde nanoporeux $CoFe_2O_4$ obtenue ont été étudiées en fonction des directions et de l'épaisseur du champ magnétique appliqué.

Mots-clés : DFT, Simulation Monte Carlo, Anti-pérovskites, $CoFe_2O_4$ nanorods, Couche d'oxide $CoFe_2O_4$ nanoporeux.

Abstract

This thesis focuses on the study of structural, electronic, magnetic and magnetocaloric properties of antiperovskite materials type Mn_3AC (A=Al, Ga) by using theoretical methods (DFT and Monte Carlo simulation).

For Mn_3GaC we investigate the second order transition. A significant MCE with no hysteresis loss is observed. On the other hand, Mn_3AlC antiperovskite also undergoes a second order transition with absence of hysteresis loss and low cost and environment friendly raw materials. For that reason, these criterions suggest that Mn_3GaC and Mn_3AlC may be a good candidate for magnetic refrigeration applications.

The second part of this thesis will be devoted to the synthesis of $CoFe_2O_4$ nanostructures including nanorods and nanoporous oxide layers. Both nanostructures were characterized by Scanning Electron Microscopy (SEM), X-ray spectroscopy (EDS) and X-ray Diffraction (XRD). The five steps of the synthesis of $CoFe_2O_4$ nanorods were reported as a function of the electrolyte's compositions. The $CoFe_2O_4$ nanoporous oxide layer was fabricated by electrochemical anodization from the parent alloy FeCoV sheet, leading to an ordered nanoporous structure of $CoFe_2O_4$. Our characterization methods confirmed the transformation of the as-anodized oxide layer into nanoporous oxide layers $CoFe_2O_4$. The magnetic properties of the obtained $CoFe_2O_4$ nanoporous oxide layer have been investigated as a function of the applied magnetic field directions and thickness.

Keywords: DFT, Monte Carlo simulation, Antiperovskites, $CoFe_2O_4$ nanorods, $CoFe_2O_4$ nanoporous oxide layers.